TURBULENCE IN THE DEEP OCEAN: A STUDY OF LEE WAVE PROPAGATION THROUGH DEPTH-VARYING CURRENTS AND THE IMPLICATIONS FOR ENERGY DISSIPATION

by

Marie Babineau

Submitted in partial fulfillment of the requirements
for the degree of Master of Science

at

Dalhousie University
Halifax, Nova Scotia
November 2023

Table of Contents

List of Tables

List of Figures

Abstract

Lee wave dissipation rates estimated from observations are two to three times lower than those predicted by models. However, such models have assumed a constant background current into which the waves propagate. To explore the impact of depth-varying currents on lee waves, I have run idealized 2D numerical simulations with sinusoidal bathymetry and linearly varying currents. For both bottom- and surface-intensified currents, waves propagate to the surface when their frequency (Ω) remains within the radiating range, $f < \Omega < N$. In contrast, waves reach an evanescent layer when their frequency is Doppler-shifted to the limits of the radiating range, namely a dissipative layer when $\Omega = f$ or an internal reflective layer when $\Omega = N$. All simulations are time-dependent, with the generation of inertial oscillations and interference patterns when reflection occurs. Furthermore, depth-varying currents allow for energy exchanges, a dominant feature of wave energetics.

List of Abbreviations and Symbols Used

Roman Symbols	Description	Units
$\mathcal{A}$	Wave action	J/s^1
b	Buoyancy	m/s^2
C_p	Phase speed	m/s
C_{gL}	Lagrangian group velocity	m/s
C_{gL-h}	Horizontal lagrangian group velocity	m/s
C_{gL-v}	Vertical lagrangian group velocity	m/s
C_{gE}	Eulerian group velocity	m/s
E	Lagrangian wave energy	J
E_0	Energy flux above bathymetry	W
E_f	Energy where $\Omega = f$	W
f	Coriolis parameter	s^{-1}
$f(k)$	Function of the wave number k	
Fr_{lee}	Lee wave Froude number	
F_e	Energy exchange fraction from *Kunze and Lien* (2019)	
F_d	Dissipative fraction from *Kunze and Lien* (2019)	
F_{em}	Modified energy exchange fraction	
g	Gravitational acceleration	m/s^2
h_0	Bathymetric height	m
h	Bathymetric function	m
h_c	Critical bathymetric height	m
h_p	Propagation depth	m
(k, l, m)	x, y, z-direction wave number	m^{-1}
K	Kinetic energy density	J/m^3
L	Bathymetric lengthscale	m
N	Buoyancy frequency	s^{-1}

Roman Symbols	Description	Units
n_x	Number of grid points in the x-direction	
p	Total pressure	Pa
p'	Pressure anomalies	Pa
$S[h](k)$	Topographic height spectrum	m
t_p	Propagation time	h, min
t_a	Analysis time	h, min
t	Time variable	h, min
t_f	Inertial period	h
$T_{L(z=h)}$	Lagrangian wave generation period	h
$U(z)$	Background current	m/s
$\mathbf{u}_t = (u, v, w)$	Total velocity field	m/s
$\overline{\mathbf{u}} = (\overline{u}, \overline{v}, \overline{w})$	Residual horizontally-averaged current	m/s
$\mathbf{u}' = (u', v', w')$	Wave velocity field	m/s
$\mathbf{u}_b = (u_b, v_b, w_b)$	Wave velocity at the bathymetry	m/s
$\mathbf{U}_b = (U_b, V_b, W_b)$	Current velocity at the bathymetry	m/s
(u'_n, v'_n, w'_n)	Normalised wave velocities	
z_d	Dissipative layer depth	m

Greek Symbols	Description	Units
Δx	Horizontal resolution	m
Δz	Vertical resolution	m
Δt	Time step	s
κ	Molecular diffusivity	m^2/s
κ_h	Horizontal eddy diffusivity	m^2/s
κ_v	Vertical eddy diffusivity	m^2/s
ν	Molecular kinematic viscosity	m^2/s
ν_h	Horizontal eddy kinematic viscosity	m^2/s
ν_v	Vertical eddy kinematic viscosity	m^2/s
ρ	Total density	kg/m^3
ρ_0	Background density	kg/m^3
$\overline{\rho}$	Horizontally averaged density	kg/m^3
ρ'	Density anomalies	kg/m^3

Greek Symbols	Description	Units
ϕ	Wave propagation angle to the horizontal	$^\circ$
Ω	Lagrangian wave frequency	s^{-1}
Ω_b	Wave generation frequency	s^{-1}
ω	Eulerian wave frequency	s^{-1}

Mathematical operations	Description	Units
$\bar{\cdot}$	Horizontal average	
$<>$	Time average	

Abreviation	Description
BIC	Bottom intensified current
SIC	Surface intensified current
IRL	Internal reflective layer
DL	Dissipative layer
NS	Navier-Stokes
RHAC	Residual horizontally-averaged current
SSA	Sea surface anomaly

Acknowledgements

Thank you to Ruth and my research committee, Dan and Carly for the guidance and support they gave me throughout the completion of my Masters degree.

Un immense merci à ma famille pour leur soutient et leur amour qui s'est fait sentir a plus de 1000 km de distance.

Chapter 1

Introduction

Winds blowing over the ocean provide $\mathcal{O}(1\text{TW})$ of power to geostrophic flow (*Wunsch*, 1998). This, energy is dissipated, leading to turbulence and mixing, with impacts on the distribution of chemical and physical water properties throughout the ocean. Importantly, the different processes leading to dissipation and their spatial distribution are still poorly understood and under active research (*Nikurashin and Ferrari*, 2011; *Waterman et al.*, 2014; *Klymak*, 2018; *Kunze and Lien*, 2019; *Shakespeare*, 2020). Among the main pathways under investigation is turbulence generated by waves propagating in the ocean's interior, known as internal gravity waves (*Shakespeare et al.*, 2021; *Sun et al.*, 2022; *Wu et al.*, 2023). This thesis explores this pathway by contrasting the impacts of bottom and surface intensified currents on the propagation, energetics and turbulence of topographically generated internal lee waves.

Lee waves are a type of internal wave generated by currents flowing over rough bathymetry, lifting isopycnals (layers of constant density) upstream of an obstacle and lowering them downstream, i.e. on the lee side (*Legg*, 2021). In an Eulerian frame of reference, a frame fixed to bathymetry, they are stationary and propagate energy upwards and downstream with regards to the current. At large amplitude, they can become unstable, leading to wave breaking and turbulence. In turn, turbulence erodes the density gradients which allows for mixing (*Osborn*, 1980). Several studies predict that lee wave breaking is an important contributor to mixing in the water column (*Garrett and Kunze*, 2007; *Nikurashin and Ferrari*, 2010a; *Melet et al.*, 2014, 2015; *Naveira Garabato et al.*, 2013; *Waterman et al.*, 2013), which in turn contributes to the global overturning circulation and large-scale climate by maintaining the deep

ocean stratification (see e.g. *Wunsch and Ferrari* (2018) for a review). Considering the influence of lee waves on climate, they should be adequately represented in climate models. However, these use a 1° to 1/4° (≈ 111 km to ≈ 28 km) resolution for oceanic components and the scale of lee wave, ranging from 100 m to 10 km, is too small to be directly resolved (*Melet et al.*, 2014). Therefore, a parametrization is needed. Fieldwork in the Southern Ocean has found discrepancies between the predicted and observed energy dissipation, with theory over-predicting dissipation rates (e.g. *Cusack et al.* (2017)). As the required parametrization for lee waves is based on theoretical estimates, the aforementioned discrepancies highlight the need to better understand lee waves, supported by results from *Waterman et al.* (2013).

Studies using linear theory to predict lee wave generation and energy dissipation estimate that they dissipate 0.2-0.75 TW of the deep ocean power input (*Scott et al.*, 2011; *Nikurashin and Ferrari*, 2011; *Wright et al.*, 2014; *Melet et al.*, 2014; *Trossman et al.*, 2016; *Yang et al.*, 2018). Using numerical simulations, *Nikurashin and Ferrari* (2011) estimate that 50% of the energy input into lee waves is dissipated within 1 km above bathymetry. Dissipation rates calculated from obervations show enhanced values over rough bathymetry, as expected by linear theory (*Waterman et al.*, 2013; *Sheen et al.*, 2013; *Cusack et al.*, 2017; *St. Laurent et al.*, 2012). However, these predictions break down as discrepancies between the predicted and observed dissipated energy were found when comparing observations to estimates from *Nikurashin and Ferrari* (2011). *Waterman et al.* (2013) report that only 2-20% of the radiated energy is dissipated within the first kilometre above topography, with the biggest discrepancies in zones where the flow decreases with height.

Different hypotheses like topographic blocking, 3D effects of bathymetry and interactions between waves and varying background currents could explain these energy dissipation discrepancies (*Nikurashin et al.*, 2014; *Trossman et al.*, 2016; *Zheng and Nikurashin*, 2019; *Kunze and Lien*, 2019). When applying non-linear theory, which accounts for the effects of relatively tall topography on lee wave generation, *Sheen et al.* (2013) calculate a lower dissipation rate than expected with only 10-30% of predicted energy flux dissipating within 1 km of the seafloor. Flow blocking and 3D effects were numerically tested and resulted in a reduction of 35% of the energy converted into lee-waves (*Nikurashin et al.*, 2014). Overall, predicted dissipation

rates from regions with tall topography and weak bottom current like the Indian Ocean ridges were significantly reduced by 3D effects, whereas the Southern Ocean is less affected because of the nature of its bathymetry. Recent work from *Kunze and Lien* (2019) suggest that depth varying background currents should also be considered because there is evidence of internal waves interacting with the current, being advected and in some cases, dissipating energy away from their generation site (*Cusack et al.*, 2017; *Zheng and Nikurashin*, 2019). Furthermore, when lee waves propagate into depth varying background currents, their frequency changes with depth and wave energy is not conserved. For waves propagating into slowly varying, inviscid and non-rotating background current, the conserved quantity is *wave action*:

$$\mathcal{A} = \frac{E}{\Omega} \tag{1.1}$$

which relates the wave frequency, Ω to the wave energy E in a frame of reference moving with the flow, i.e. a Lagrangian frame (*Bretherton et al.*, 1968).

For lee waves, the Lagrangian wave frequency $\Omega = -kU(z)$ is set by the bathymetric wave number k and the background current $U(z)$. When lee waves propagate through bottom intensified currents (BIC), their frequency is Doppler-shifted and decreases with height. For wave action to be conserved, the wave energy varies proportionally to changes of the wave frequency through an energy exchange with the background current. In the case of BIC, a fraction of the wave energy is lost to the background flow, which reduces the energy available for turbulence. This case has been theoretically explored by *Kunze and Lien* (2019) and they suggest that this mechanism could partially resolve the discrepancies between observations and theory and that it should be taken into account in energy budgets.

Lee wave propagation through surface intensified currents (SIC) is explored by *Baker and Mashayek* (2021). For this case, conservation of wave action states that the wave will gain energy from the background flow as the wave propagates upwards and the frequency increases with height. This theoretical study shows an energy increase in the lee wave field. Lee wave theory was derived based on an infinitely deep ocean, where surface reflection does not occur (*Scorer*, 1949; *Bell*, 1975). However, work from *Baker and Mashayek* (2021) show that wave reflection at

the surface has the potential to increase vertical velocities, mixing and dissipation, thus substantially modifying the lee wave field. The interaction of downward and upward propagating waves complexifies the energetics of the current. As this study was based on hydrostatic, linear theory and idealized bathymetry, velocity and stratification profiles, questions remain on the applicability of these results to the real ocean, leaving a gap for the integration of data-derived profiles and bathymetry into numerical simulations. Furthermore, the case of internal reflective layers (IRL), explained in detail in the Chapter 2, is not considered in *Baker and Mashayek* (2021).

A summary of wave propagation through constant and depth varying currents is presented in figure 1.1. Two critical layers are illustrated in this figure: the dissipative layer (DL), where the wave energy dissipates if the the Lagrangian frequency equals the Coriolis parameter, f, and the internal reflective layer, where the wave energy is reflected downwards if the wave frequency is Doppler-shifted to the Buoyancy frequency, N. These critical layers are further explained in Chapter 2.

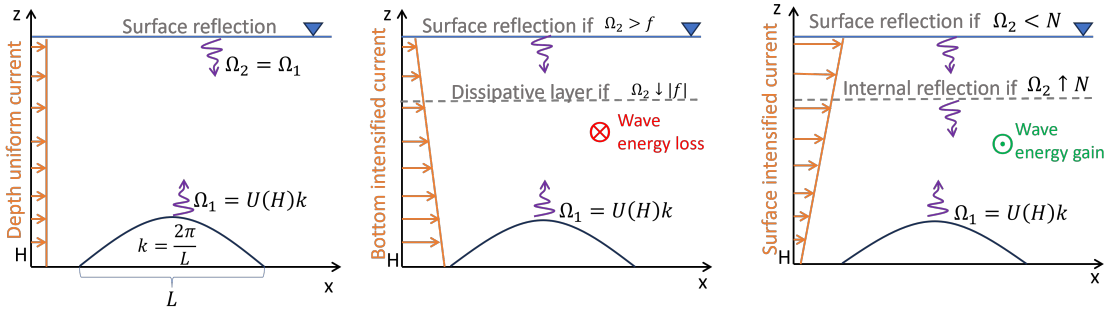

Figure 1.1: Lee wave propagation. (left) Propagation through a depth uniform current. The Langrangian frequency stays constant with depth, no energy is exchanged with the background current. (middle) Propagation through a bottom intensified current. The Lagrangian wave frequency decreases with height and energy is lost to the background current. It reaches a *dissipative layer* where its frequency equals the Coriolis frequency, f. (right) Wave propagation through a surface intensified current. The Lagrangian wave frequency increases with height and energy is gained from the background current. If it reaches the buoyancy frequency, N, within the water column, the wave will reflect downwards.

1.1 Objectives

This Master's thesis tested and extended the theory described by *Kunze and Lien* (2019) and *Baker and Mashayek* (2021) by using a numerical model to calculate the energy flux and dissipation to answer the following research questions: **What are the impacts of depth varying currents on oceanic lee wave energetics and the energy available for turbulence?** The goal is to quantify, map and compare energy profiles, turbulence and dissipation arising from different currents to assess the range of lee wave variability in the water column. This work gives insight into ocean mixing, as part of the energy transferred to small turbulent scale will be dissipated and part of it will be available for mixing. Identifying turbulent zones with high dissipation rates will help to identify zones where mixing is high.

In this thesis, numerical results are compared to theoretical predictions. Chapter 2 presents the theoretical framework and predictions for linear lee wave theory. In Chapter 3, the impacts of bottom intensified currents are explored and tested by comparing theoretical predictions to numerical results from idealised 2D simulations. Chapter 4 includes a similar analysis, but for surface intensified currents. Finally, in Chapter 5, I present overall conclusions.

Chapter 2

Theoretical framework

Aviation accidents caused by enhanced turbulence in the lee of mountains sparked interest in stratified atmospheric flow over mountains and the internal oscillations that result (*Colson*, 1952). Theoretical analysis and laboratory experiments from *Long* (1953, 1954, 1955) investigate these atmospheric lee waves. Results from Long's experiments illustrate many physical aspects associated with a lee wave: an eddy, wave reflection at the surface and energy dissipation caused by turbulence (Figure 2.1 a), *Long* (1953)). The circular streamline on the plot below the picture illustrates the eddy, and the wave reflection is identifiable by the oscillating pattern in the streamlines. The surface acts as a rigid lid, and upward propagating waves reflect downwards. Finally, the energy dissipation caused by turbulence can be seen as the second undulation after the obstacle is dampened. The general streamline pattern illustrated in Long's experiment can also be seen in Figure 2.1b). However, the depth of the numerical simulation is bigger than the numerical tank, and the simulation time is shorter than the time required for the wave energy to reach the surface. Thus, reflection does not occur. Figure 2.1 provides visual insight on lee waves, but a theoretical analysis is necessary to fully understand how energy propagates, how instabilities develop, and how turbulence is generated.

2.1 Lee Wave Theory

Lee waves have been described using linear theory, valid when wave amplitudes are small compared to horizontal scales. Here, the Navier-Stokes (NS) equations are simplified by making the Boussinesq approximation. The continuity equation

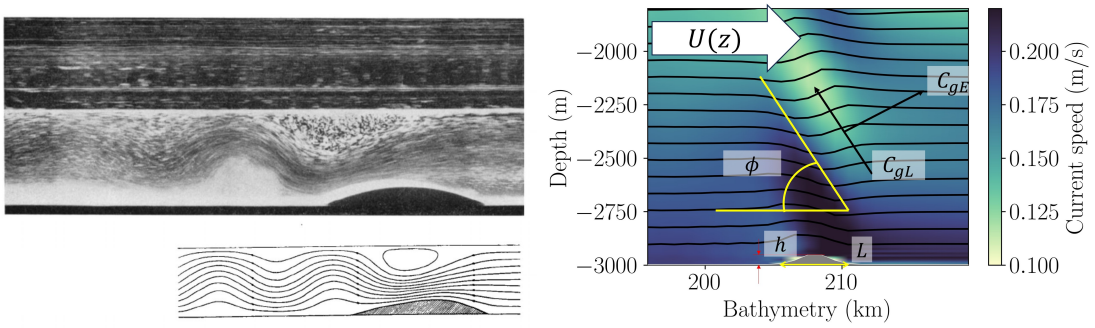

(a) (b)

Figure 2.1: (a) Lee wave generated by stratified flow over an obstacle in an experimental tank, from *Long* (1955) with streamline plot (bottom). (b) Numerical lee wave generated by stratified flow over an idealized topography, and some characteristic parameters like the length-scale L, the characteristic height h_0, the propagation angle of the wave ϕ, and the direction of the group velocity, i.e. is the speed at which the wave energy propagates in a Lagrangian frame C_{gL}, and an Eulerian frame of reference C_{gE}.

and the three momentum equations have five unknowns: the velocity field ($\mathbf{u}_t$), pressure (p), and density (ρ). The buoyancy equation, obtained by multiplying the density-tendency equation by the ratio of the gravitational acceleration to the background density, $-g/\rho_0$, is used in combination with thermal winds to close the problem. A vertically varying background current is accounted for by decomposing the total current as:

$$\begin{aligned}\mathbf{u}_t =&(u,v,w) = U(z)\widehat{i} + \overline{\mathbf{u}} + \mathbf{u}' \\ =&(U(z) + \overline{u} + u', \overline{v} + v', \overline{w} + w')\end{aligned} \tag{2.1}$$

where $U(z)$ is a constant background current, $\overline{\mathbf{u}} = (\overline{u}, \overline{v}, \overline{w})$ is the residual horizontally-averaged current current (RHAC), averaged in the x-direction, and **u'** $= (u', v', w')$ are the wave perturbations. The residual horizontally averaged current allows us to isolate physical phenomenon such as the development of inertial oscillations in the water column (*Nikurashin and Ferrari*, 2010a). Density and pressure are also decomposed into a background component and a perturbation: $\rho = \rho_0 + \overline{\rho_{y,z}} + \rho', p = \overline{p} + p'$. The 2D, non-hydrostatic, and Boussinesq governing equations are:

$$\frac{\partial u'}{\partial x} + \frac{\partial w'}{\partial z} = 0 \tag{2.2}$$

$$\frac{\partial}{\partial t}(u) + \mathbf{u}_t \cdot \nabla u + fv = \frac{-1}{\rho_0}\frac{\partial p'}{\partial x} + \nu\nabla^2 u \tag{2.3}$$

$$\frac{\partial}{\partial t}(v) + \mathbf{u}_t \cdot \nabla v + fu = \frac{-1}{\rho_0}\frac{\partial p'}{\partial y} + \nu\nabla^2 v \tag{2.4}$$

$$\frac{\partial}{\partial t}(w) + \mathbf{u}_t \cdot \nabla w = \frac{-1}{\rho_0}\frac{\partial p'}{\partial z} + b + \nu\nabla^2 w \tag{2.5}$$

$$\frac{\partial}{\partial t}(b) + \mathbf{u}_t \nabla b = \kappa\nabla^2 b \tag{2.6}$$

where f is the Coriolis parameter, κ is the diffusivity, ν is the kinematic viscosity and $\nu\nabla^2\mathbf{u}$ represents viscous effects. Buoyancy is $b = -\rho' g/\rho_0$ and the buoyancy frequency also name Brunt-Väisälä frequency, N is given by:

$$N^2 = -\frac{g}{\rho_0}\frac{\partial \rho}{\partial z}. \tag{2.7}$$

The dispersion relation describes the relationship between the wave frequency and wavenumbers. For a classic treatment of the steady lee wave problem, the equations are assumed to be linear, i.e. the products of perturbations are negligible, inviscid, and the background current is constant, see *Bell* (1975) for a detailed derivation. Using these assumptions, the equations 2.3 to 2.6 can be simplified and combined to obtain an expression for w' alone. The expression is :

$$\frac{\partial^2}{\partial t^2}\left(\frac{\partial^2 w'}{\partial x^2} + \frac{\partial^2 w'}{\partial y^2} + \frac{\partial^2 w'}{\partial z^2}\right) + f^2\frac{\partial^2 w'}{\partial z^2} + N^2\left(\frac{\partial^2 w'}{\partial x^2} + \frac{\partial^2 w'}{\partial y^2}\right) = 0. \tag{2.8}$$

The dispersion relation is obtained by substituting a wave-like solution of the form

$$w' = w_0 \exp^{i(kx+ly+mz-\Omega t)} \tag{2.9}$$

into equation 2.8. The different variables are w_0, the wave amplitude, $k = 2\pi/L$, the x-direction horizontal wavenumber set by the topographic length L, l the y-direction wavenumber, m the vertical wavenumber and Ω the Lagrangian wave frequency. The y-derivatives and the horizontal wavenumber in the y-direction are null for a two-dimensional system. The dispersion relation is then:

$$m^2 = \frac{k^2(N^2 - \Omega^2)}{(\Omega^2 - f^2)}. \tag{2.10}$$

Equation 2.10 is highly simplified, making it easy to use and understand. However, viscous and diffusive effects can be non-negligible (*Shakespeare and Hogg*, 2017; *Kunze and Lien*, 2019; *Gill*, 2003). For a derivation of the steady lee wave dispersion relation including energy dissipation see *Baker and Mashayek* (2021). For a non-hydrostatic derivation that includes the effects of non-uniform stratification, a shear background flow, and viscous and diffusive effects, see *Sun et al.* (2022). The wave frequency at which an observer moving with the current would encounter peaks or troughs of the wave, i.e. in a Lagrangian frame of reference, is $\Omega = \omega - U(z)k$, where ω is the wave frequency in a frame of reference fix with topography (an Eulerian frame) (*Bretherton et al.*, 1968). Lee waves are steady, meaning that $\omega = 0$ and have a stationary pattern to an Eulerian observer (*Legg*, 2021). Thus, the Lagrangian frequency for lee waves is $\Omega = -U(z)k$. The latter is often referred to as the Doppler-shifted frequency.

To have a vertically propagating wave solution, the vertical wavenumber, m, set by equation 2.10, must be real (*Gill*, 2003). Thus, the lee wave frequency, Ω, is bounded by the Coriolis parameter f, and the buoyancy frequency N: $f < \Omega < N$. When the wave propagates through a depth-varying current, $U(z)$, its frequency $\Omega = U(z)k$ can change to the point where it lies outside the radiating range. Then, the wave becomes evanescent and can not propagate anymore.

The energy propagation speed is given by the group velocity C_g. In a Lagrangian frame of reference, the group velocity for internal waves generated at a horizontal boundary, such as lee waves, is given by the gradient of the Eulerian wave frequency in wavenumber space:

$$\begin{aligned} C_{gL} &= \left(\frac{\partial \omega}{\partial k}, \frac{\partial \omega}{\partial m} \right) \\ &= \left(\frac{-(N^2 - U(z)^2 k^2)(U(z)^2 k^2 - f^2)}{U(z) k^2 (N^2 - f^2)}, \frac{(N^2 - U(z)^2 k^2)^{1/2} (U(z)^2 k^2 - f^2)^{3/2}}{U(z) k^2 (N^2 - f^2)} \right), \end{aligned} \tag{2.11}$$

where the dispersion relation (equation 2.10) gives an expression for ω, using $\Omega = \omega - U(z)k$. As stated earlier, the Eulerian lee wave frequency (ω) is null, but equation 2.11 shows that its derivatives are non-zero.

The direction in which the group velocity propagates is obtained by rearranging

equation 2.10 to get k/m, the ratio of the vertical length scale of the wave over the horizontal length scale. The arctangent of this ratio gives the angle of propagation to the horizontal, ϕ, which also represents the angle of lines of constant phase:

$$\phi = \arctan(k/m). \tag{2.12}$$

Figure 2.1 b) illustrates these parameters.

When the wave propagates through a positively sheared background current, the Lagrangian frequency will increase with height. The angle of wave propagation will steepen (see equations 2.10 and 2.12), and the vertical group velocity accelerates with height while the horizontal group velocity decelerates. When $\Omega \sim N$, the wave has reached an internal reflective layer and reflects downward (*Scorer*, 1949; *Teixeira et al.*, 2013; *Baker and Mashayek*, 2021). The depth of this layer is also affected by varying stratification as it changes the upper bound of the radiating regime, N. Note that a part of the energy might cross this layer, a phenomenon called wave transmission, while the rest is reflected downwards (*Nault and Sutherland*, 2007). For waves propagating through a negatively sheared current where the velocity decreases above bathymetry, the Lagrangian wave frequency decreases as the wave propagates upwards and the angle to the horizontal gets smaller. The wave will encounter a dissipative layer where its frequency reaches a near-inertial state, $\Omega \sim f$ (*Jones*, 1967). Vertical wave shear will become large, dissipating the wave energy.

2.1.1 Ray Tracing

The evolution of the propagation angle of the wave to the horizontal as a function of the Lagrangian wave frequency can be theoretically calculated using dispersion relation (eq. 2.10) and equation 2.12 and is illustrated in Figure 2.2. As the propagation angle of the lee wave changes, the path followed by the energy also changes. Ray tracing treats wave energy as a particle moving along a ray, and it can be used to predict the path followed by wave energy when propagating through a slowly varying non-uniform background (*Sutherland*, 2010). For internal waves, in a frame of reference fixed with topography, it is possible to combine the horizontal and vertical group velocities to get the vertical over the horizontal particle displacement,

$\frac{dz}{dx}$, i.e. the trajectory of the wave energy:

$$\frac{dz}{dx} = \frac{C_{gz}}{C_{gx} + U(z)}, \tag{2.13}$$

where the components of the group velocity are given in eq. 2.11. Ray-tracing predicts that wave energy propagating through a surface-intensified current will reflect at an internal reflective layer when its frequency matches the buoyancy frequency and that wave energy propagating through a backing current will asymptotically approach a layer when its frequency matches the Coriolis parameter. Ray tracing is based on a slowly varying and hydrostatics approximation, which breaks down when m approaches 0. However, mathematical treatment of the ray path equation allows to estimate the trajectory near the level where m vanishes and gives an acceptable qualitative image of wave reflection. For further information and detailed equations, consult e.g. *Gill* (2003), Chapter 8 and *Sutherland* (2010), Chapters 3 and 6.

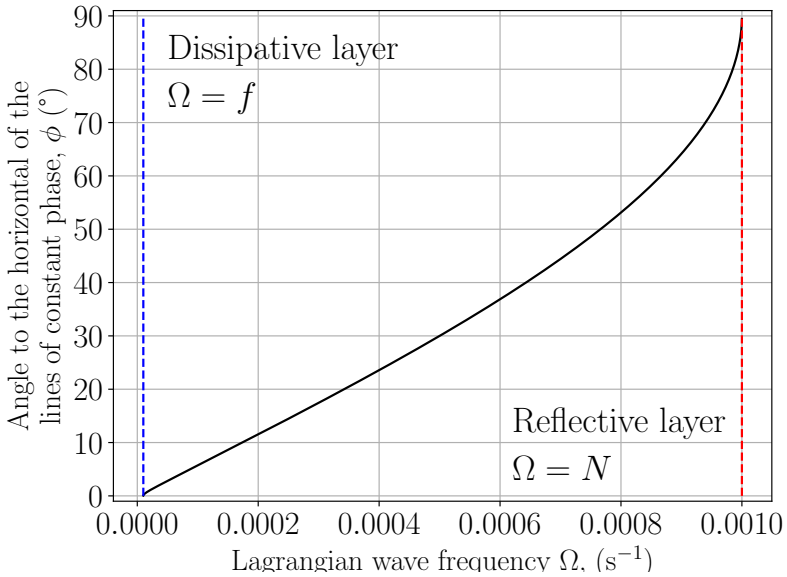

Figure 2.2: Evolution of the wave angle to the horizontal as a function of the wave frequency for a linear lee wave flowing over a sinusoidal topography with a length-scale $L = 1$ km, a Coriolis parameter $f = 1.2 \times 10^{-4}$ s^{-1}, and a buoyancy frequency $N = 10^{-3}$ s^{-1}. As the wave frequency changes towards the Coriolis parameter, the angle to the vertical reduces, and the wave becomes more and more horizontal. Contrarily, when the frequency is Doppler shifted and approaches the buoyancy frequency, the vertical scale of the wave dominates.

2.1.2 Wave Velocity Predictions

For a depth uniform current, the vertical component of velocity of a wave generated at an idealized bathymetry, w_b, can be expressed as :

$$w_b = -\mathbf{U}_b \cdot \nabla h \tag{2.14}$$

where $\mathbf{U}_b = (U_b, 0, 0)$ is the current velocity at the bathymetry, $h = 0.5h_0 \cos(kx)$ and h_0 is amplitude the bathymetric bumps. Using the no-flux boundary condition, the vertical velocity at the bottom of the domain is

$$w_b = U_b \frac{h_0}{2} k \sin(kx)|_{z=0}. \tag{2.15}$$

Expressions for u and v are derived using the polarization relation:

$$u_b = \frac{h_0}{2} U_b m \sin(kx + mz) \tag{2.16}$$

$$v_b = \frac{f}{\Omega_b} \frac{h_0}{2} U_b m \sin(kx + mz). \tag{2.17}$$

At the bathymetry, equation 2.15 shows that for a fixed value of h_0 and bottom velocity U_b, the vertical wave velocity depends on the horizontal wavenumber k, meaning that larger vertical velocities are expected for larger wavenumbers. As k is inversely proportional to bathymetric length scales, smaller length scales will generate lee wave with faster upward velocity. Conversely, the magnitude of the horizontal wave velocity u_b depends only on m, which decreases as k increases. Therefore, slower horizontal velocities are expected for wave generated over smaller bathymetric scales.

For a wave propagating in a depth-varying current, the vertical wavenumber given by equation 2.10 changes with height. The expression for vertical and horizontal velocity profiles will change to:

$$w_b = U_b k h_0 \sin(kx + m(z)z) \tag{2.18}$$

and

$$u_b = -U_b h_0 \left(\left(\frac{\partial}{\partial z} m(z) \right) z + m(z) \right) \sin(kx + m(z)z), \tag{2.19}$$

$$v_b = \frac{f}{\omega_b}\frac{h_0}{2}U_b\left(\left(\frac{\partial}{\partial z}m(z)\right)z + m(z)\right)\sin(kx + m(z)z). \tag{2.20}$$

The horizontal magnitude of the wave velocity is now depth-dependent.

2.2 Lee Wave Energetics

When lee waves propagate through a vertically sheared flow, their energy will not be conserved. This can be seen by deriving the energy equation and allowing perturbation in the presence of a sheared background current. The wave kinetic energy (K) equation in an Eulerian frame of reference is obtained by taking the dot product of the momentum equations (equations 2.3 to 2.5) and the wave velocity, $\mathbf{u}' = (u', v', w')$, and multiplying by the background density ρ_0. It is given by:

$$\begin{aligned}\underbrace{\frac{\partial}{\partial t}K}_{1} + \underbrace{\rho_0\mathbf{u}'\cdot\left(\frac{\partial}{\partial t}\overline{\mathbf{u}}\right)}_{2} = &-\underbrace{U\frac{\partial K}{\partial x}}_{3} - \underbrace{\overline{u}\cdot\nabla K}_{4} - \underbrace{\mathbf{u}'\nabla K}_{5} - \underbrace{\rho_0 u'w'\frac{dU}{dz}}_{6} \\ &\underbrace{- w'\left(\mathbf{u}'\cdot\frac{\partial\overline{\mathbf{u}}}{\partial z}\right)}_{7} - \underbrace{w'\rho g}_{8} - \underbrace{\nabla(\mathbf{u}'p)}_{9} + \underbrace{\nu\nabla^2(K)}_{10} - \underbrace{\nu\rho_0(\nabla\mathbf{u}')^2}_{11}\end{aligned} \tag{2.21}$$

with $K = \frac{1}{2}\rho_0(u'^2 + v'^2 + w'^2)$. Equation 2.21 is similar to the one derived by *Nikurashin and Ferrari* (2010a), with the exception that the geostrophic current, i.e. the background current in our case, varies with depth. The terms in the kinetic energy equation are: (1) the time derivative of the K, (2) the time variability of the RHAC, (3) the advection of K by the background flow, (4) the advection of K by the residual horizontally averaged flow, (5) the K advection by perturbations, (6) the shear production from the prescribed background current, (7) the shear production from the residual horizontally averaged currents (RHAC), (8) the potential to K transfer, (9) the pressure work, (10) the viscous diffusion of K and finally, (11) is the K dissipation. The advection and transport terms, 3, 4 and 5, arise from the non-linear term in the momentum equation. The shear production terms 6 and 7 represent the wave energy exchange with the different current components, i.e. background current and the residual horizontally averaged currents. The pressure work term (9) comes from the pressure force and is also usually written $\nabla\cdot\mathbf{u}p$ where

we have taken advantage of the fact that $\nabla \cdot \mathbf{u} = 0$. Diffusion of kinetic energy (10) represents the diffusion of kinetic energy due to the fluid's viscosity. The dissipation of K (11) is an energy sink and relates to ocean mixing through the Osborn relation. For a detailed derivation of the energy equation, see appendix A.

2.3 Wave Action

As explicitly shown by the shear production terms in the energy equation, energy is not conserved for waves propagating through a varying background current. The conserved quantity is called *wave action* (eq. 1.1), $\mathcal{A} = \frac{E}{\Omega}$, for inviscid and non-rotating fluids. It describes wave-mean flow interactions (*Bretherton et al.*, 1968) and links the total energy density (E) to the frequency shift. Under conservation of wave action, waves that propagate through depth-varying currents see their Lagrangian frequency, $\Omega = -kU$, being Doppler-shifted, and their total energy change, as it is partially reabsorbed (enhanced) in a bottom (surface intensified) currents (*Bretherton et al.*, 1968). Looking at eq. 1.1, the energy will vary proportionally to the wave frequency when conservation of wave action applies.

Some limitations regarding the applicability of conservation of wave action in the ocean are that this theory was developed for an inviscid fluid, non-dispersive wave packet in an unbounded domain. First, when considering a viscous fluid, part of the total wave energy is dissipated by viscous forces and part of the energy is exchanged with the background flow. Enhanced dissipation, caused by dissipative layers or the steepening and breaking of the wave, may break the relationship between Ω and the energy, thus breaking down the conservation of wave action. Second, is it hard to keep track of wave packets when the wave is dispersive, i.e. when its phase speed depends on the length scale of the wave, $C_p = \frac{\omega}{k} = f(k)$ where $f(k)$ is a function of the horizontal wavenumber. As conservation of wave action applies to a wave packet, dispersion effects make it harder to use eq. 1.1 directly. Finally, assuming an unbounded domain does not always hold for the real ocean. As waves propagate, they can reach the surface or an internal reflective layer, which acts as a boundary, and reflect downwards. This reflection could lead to vertical mode and interference, complicating the interpretation of eq. 1.1.

2.4 Wave Interactions

As the wave propagates through a depth-varying current, it will lose (gain) energy to (from) the background through a momentum exchange (*Bretherton et al.*, 1968). Energy lost from the wave will be gained by the background current and lead to an acceleration of the latter (*Grimshaw*, 1984). The opposite is also true; for the case where the wave gains energy from the current, the latter loses some of its momentum. Therefore, a bottom-intensified background current is expected to slow down as lee waves are propagating upwards, and a surface-intensified current is expected to accelerate. The trajectory of the wave energy has a horizontal component leading to a lateral advection of kinetic energy. When reflection occurs, the wave will lose what has been gained downstream of its upward trajectory. Depending on the background current, reflected waves can superpose with upward propagating waves, generating vertical modes and potentially modifying wave generation at the bathymetry (*Zheng and Nikurashin*, 2019; *Baker and Mashayek*, 2021).

Lee wave breaking also influences the background conditions. The energy dissipation can slows down the mean flow, and inertial oscillations, IO and other higher-frequency internal waves can be generated (*Nikurashin and Ferrari*, 2010a).

2.5 Limits of Linear Theory

A limit of applicability of the linear theory is defined by the Lee-wave Froude number, Fr_{lee}:

$$\mathrm{Fr}_{lee} = \frac{h_0 N}{U}, \tag{2.22}$$

where h_0 represents the characteristic topographic height and N/U, the vertical scale of the lee wave, calculated with the velocity U (m/s) and buoyancy frequency N (s^{-1}) at the ocean floor (*Sutherland*, 2010). The theoretical, critical value for which linear theory can be applied is $\mathrm{Fr}_{lee} = 1$, where topographic features are small enough that the deepest currents can flow over the crest of the topography. The flow is said to be supercritical when $\mathrm{Fr}_{lee} > 1$ (*Nikurashin et al.*, 2014). Then, topographic blocking happens, and the lower layers of the flow get blocked by topography. This stationary layer acts as a virtual seafloor, reduces the effective topographic scale

generating lee waves, and the flow becomes non-linear. The effective topographic height, $h_{eff} = U/N$, is the vertical scale, measured from the crest of the topography, associated with potential energy equal to the flow kinetic energy (*Winters and Armi*, 2012). In a supercritical regime, the waves generated directly above topography have a large amplitude. They can rapidly become non-linear and break, dissipating energy above their generation site.

Chapter 3

Lee Waves in a Bottom-Intensified Current

3.1 Introduction

The goal of this chapter is to examine lee wave propagation through a bottom-intensified current (BIC) and compare numerical model outputs of energy exchange and dissipation to theoretical energy predictions. To do so, a series of eight 2D simulations using periodic bathymetry was run using the MITgcm numerical model with the parameters presented in section 3.2 (*Marshall et al.*, 1997). Horizontal wave numbers, k, were varied between each simulation to test wave-mean flow interactions. Eight values of k were selected to cover the lee wave radiating range given the chosen buoyancy frequency and Coriolis parameter. This allows for a comparison of two different regimes: the propagating regime, where the lee wave reaches the surface and the dissipative regime, where the wave encounters a dissipating layer within the water column. This variation of wave number also allows us to assess gradual changes between lee waves generated over a range of length scales as $k = 2\pi/L$ (as defined in Chapter 2.1). Two additional simulations were run with a depth-uniform current to compared lee wave propagation and highlight the impacts of depth-varying currents. For the simulation's nomenclature, the first three letters are the type of background current, followed by a number corresponding to the topographic length scale in kilometres, e.g. BIC5km corresponds to a bottom-intensified current simulations where the length scale is 5km. For the depth-uniform simulations, the first letter, "B", relates to the type of current used in the chapter, the second and third indicate

the type of shear followed by the bathymetric scale, e.g. BNS5km corresponds to a simulation associated with the bottom-intensified chapter (B), with a non-sheared (NS) background current and a 5 km lengthscale (5km).

3.1.1 Expectations

Chapter 2 presented in detail linear lee wave theory and wave-mean flow interactions. The main theoretical predictions that we aim to examine are summarized hereafter:

1. For smaller values of k, bottom horizontal wave velocity u'_b and v'_b are faster and vertical wave velocity w'_b are slower compared predictions for larger values of k, based on the polarisation relation presented in Chapter 2. In mathematical terms, for $k_1 < k_2$: $u'_{b,k1} > u'_{b,k2}$, $v'_{b,k1} > v'_{b,k2}$ and $w'_{b,k1} < w'_{b,k2}$;

2. An exponential increase of the vertical wavenumber m associated with flattening of the lines of constant phase as the wave energy propagates upwards and away from its generation site, based on the dispersion relation;

3. An exponential decrease of the vertical group velocity C_{gL-v} associated with a flattening of the energy path with height as energy propagates upwards and away from its generation site, based on the dispersion relation;

4. A decrease of the Doppler-shifted wave frequency with height with a dissipative layer where the wave frequency matches the Coriolis parameter

5. Wave reflection from the surface leading to normal modes if the wave energy propagates to the surface;

6. A larger fraction of kinetic energy dissipation for wave encountering lower dissipative layers as less energy is lost to the background flow, leaving more energy available for dissipation;

7. A modification of the background current because of wave-mean flow interactions;

8. The generation of inertial oscillations (IO) ;

9. The generation of surface displacements by waves freely propagating through the water column (*de Marez et al.*, 2020).

3.1.2 Energy Predictions for Bottom-Intensified Currents

Linear theory provides an equation for the rate of upward propagation of energy for waves generated at a horizontal boundary in a rotating fluid, i.e. the rate of energy input into the ocean at the bathymetry. Prediction 6 is specific to this chapter, and numerical results will be compared to theoretical estimates developed by *Kunze and Lien* (2019), who used the following expression to predict the energy flux cospectrum:

$$coS[wp](k) = U_b \rho_0 \sqrt{N^2 - k^2 U_b^2} \sqrt{k^2 U_b^2 - f^2} S[h](k) \tag{3.1}$$

where ρ_0 is the background stratification, N^2 the buoyancy frequency, U_b is the current speed at the bathymetry, k is the horizontal wavenumber, f the Coriolis parameter and $S[h](k)$ topographic height spectrum. The numerical simulations have sinusoidal topographies of amplitude h_0 and lengthscale $2\pi/k$. Thus the flux cospectrum for each wavelength is determined using a spectrum given by :

$$S[h] = h_0^2/k. \tag{3.2}$$

Linear theory and wave action can be used to predict the energy available for dissipation. The latter depends on the depth of the dissipative layer, as the wave will exchange less (more) energy with the background flow if it reaches a deeper (shallower) dissipative layer. If the total energy is considered the sum of that exchanged and dissipated, energy losses to the current result in less energy available to dissipate. Two adaptations of figure 6 from *Kunze and Lien* (2019) made with equation 3.1 using the parameter space of this thesis are presented in figure 3.1. Panel a) presents the vertical energy flux for a k^{-2} topographic spectrum discussed in *Kunze and Lien* (2019), and panel b) the energy flux for the uniform spectrum (without accounting for topographic blocking). Predictions for our sinusoidal simulations are extracted from b) by matching topographic lengthscales to the x-axis. On both panels, the dissipative fraction (F_d, red line)is the largest for wavenumbers $k < 10^{-4}$ m^{-1}, as their frequencies are smaller and closer to f. For wave numbers larger than $k = 10^{-4}$ m^{-1}, the energy lost to the background dominates as the wave propagates further into the water column and thus has more time to exchange energy. For single wavelength topographies, the energy flux increases with the wavenumber, meaning that more

energy is transferred upwards for lee waves generated over small-scale bathymetry. The energy flux increases until $k \approx 2.5 \times 10^{-3}$ m^{-1} after which it decreases abruptly.

3.2 Methods

3.2.1 Numerical Simulations

Eight BIC simulations were run using sinusoidal bathymetry of different length scales illustrated in figure 3.2 alongside the background current and stratification profiles used in this chapter. The length scales were chosen to cover the radiating range $f < \Omega_g < N$ where $f = 10^{-5}$ s^{-1} and $N = 10^{-3}$ s^{-1}. The *generation frequency*, Ω_b, is the Lagrangian wave frequency generated by the current flowing at the bottom of the domain. Simulations BIC1.4km to BIC7km are run with a horizontal resolution of $\Delta x = 50$ m and $\Delta t = 2$ s, and simulations BIC13km to BIC72km were run with $\Delta x = 200$ m and $\Delta t = 5$ s. Different horizontal resolutions are used because of the range of length scales, and the time steps were adjusted to ensure numerical stability. The vertical resolution is uniform across all simulations with $\Delta z = 10$ m. The horizontal eddy viscosity and diffusivity are set to 5×10^{-2} m^2/s and set to 5×10^{-4} m^2/s in the vertical. The background current is forced by adding a body force of $U(z)f$ to the y-direction momentum equation. All simulations are run with a free surface upper boundary condition to allow for surface reflection of the propagating waves.

Two additional depth-uniform current simulations were run to offer a comparison point with BIC simulations. The chosen lengthscale are 5 km and 72 km. The numerical set up is identical to the analogous BICs simulations. A detailed description of the simulations is presented in Appendix B.

Predicted horizontal and vertical group velocities are calculated using equation 2.10 for the prescribed background-current profile. Then, equation 2.13 is integrated numerically to obtain the theoretical ray path and propagation depth h_p, i.e. the depth of the dissipative layer. Where no dissipative layer exists, h_p is the entire domain depth. The time required for the wave energy to reach a dissipative layer or the surface is defined as the *propagating time*, t_p, and it was estimated by integrating

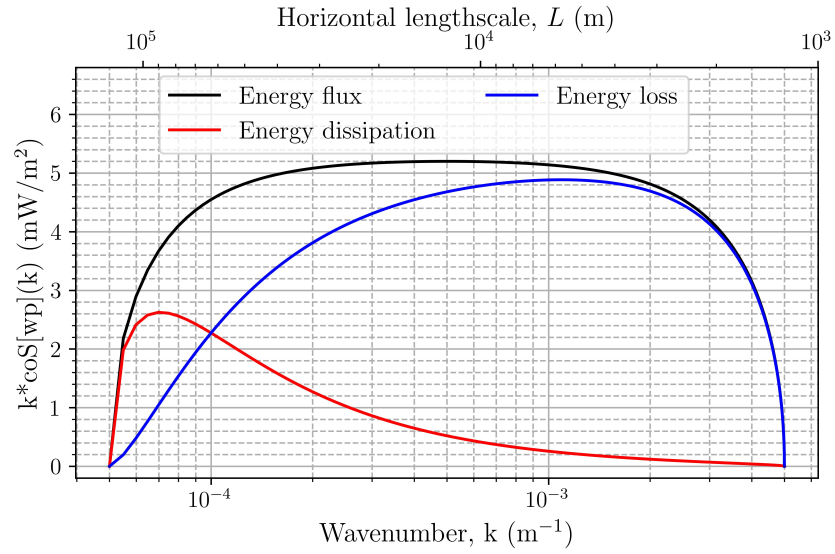

(a)

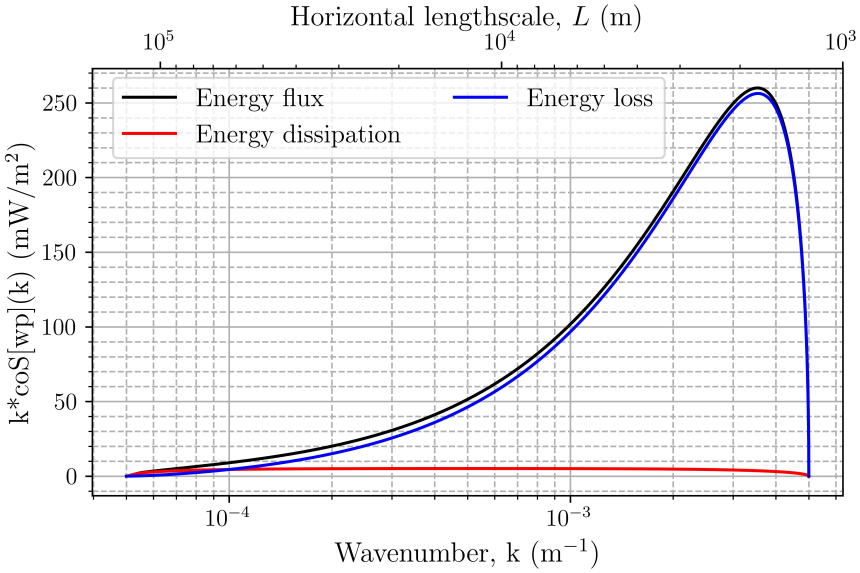

(b)

Figure 3.1: Reproductions of Figure 6 from *Kunze and Lien* (2019), lee wave vertical energy flux $\langle wp \rangle$ for lee waves propagating through negatively sheared flow from (a) a k^{-2} topographic height spectrum and (b) a uniform topographic spectrum with $h_0 = 50$ m for all wavenumbers. Here, topographic blocking is not taken into account. The total wave energy (black) has been separated into a fraction of energy dissipated, F_d (red) and energy lost to the background flow, F_e (blue). A bigger fraction of wave energy is available for turbulence and mixing for lower values of horizontal wavenumber k than for higher values. The Coriolis parameter is $f = 10^{-5}$ s^{-1}, $N = 0.001$ s^{-1} and $U_b = 0.2$ m/s.

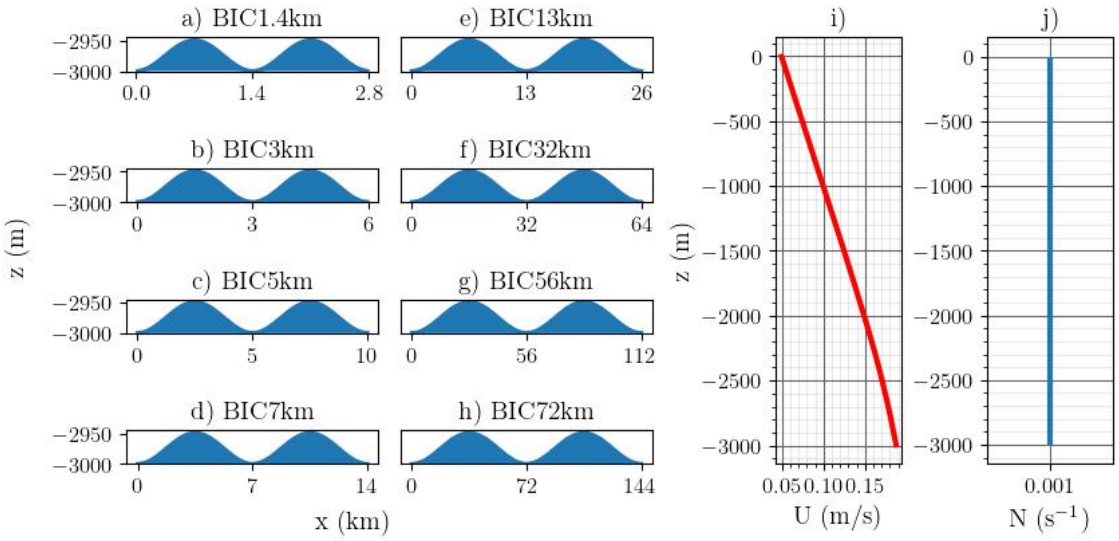

Figure 3.2: a) to h) Bathymetry for each simulation, f) Background current profile and g) Stratification profile.

the vertical group velocity C_{gz} over the propagating depth. An *analysis time*, t_a is set to $1.5t_p$ for the simulations to be dynamically comparable. The theoretical propagation time is infinite for simulations with a dissipative layer because the vertical group velocity tends to zero near the dissipative layer. Thus, the actual propagation time used to analyze the simulation corresponds to the time it takes for the wave to reach a depth where its frequency equals $1.1f$. This choice is motivated by results from *Garrett* (2001), who defined the near-inertial band as $1.1f$. The background flow is prescribed over the whole domain and ramped up to the desired value over 14 hours for simulation BIC1.4km and over 24 hours for the other simulations to limit the numerical noise generated by a sudden simulation start-up. The ramping-up forcing accelerates the background flow over four hours and stays steady for the last 20 hours. However, since the propagation time of BIC1.4km is less than 24 h, the ramping-up period was shortened for this simulation. Table 3.1 shows the simulation parameters. The first five simulations, BIC1.4km to BIC13km, are referred to as *propagating simulations* because the wave energy is free to propagate through the depth of the domain. Simulations BIC32km to BIC72km are referred to as *dissipative simulations* because of the presence of the dissipative layer.

Table 3.1: Parameter of the sinusoidal simulations with a bottom-intensified current. The Coriolis parameter is $f = 10^{-5}$ s^{-1} and buoyancy frequency $N = 10^{-3}$ s^{-1}.

	Length scale L km	Horizontal wavenumber k m^{-1}	Generation frequency Ω_b s^{-1}	Propagation depth h_p m	Propagation time t_p h	Analysis time t_a h
BIC1.4km	1.4	44.88×10^{-4}	8.98×10^{-4}	0	21	33
BIC3km	3	20.94×10^{-4}	4.18×10^{-4}	0	40	61
BIC5km	5	12.57×10^{-4}	2.51×10^{-4}	0	67	101
BIC7km	7	8.98×10^{-4}	1.79×10^{-4}	0	95	143
BIC13km	13	5.03×10^{-4}	0.97×10^{-4}	0	191	287
BIC32km	32	1.96×10^{-4}	0.38×10^{-4}	19	1005	1507
BIC56km	56	1.16×10^{-4}	0.23×10^{-4}	842	924	1386
BIC72km	72	0.87×10^{-4}	0.17×10^{-4}	1394	809	1213

3.2.2 Energy Calculations

First, horizontal averages of the currents are assumed to be associated with inertial oscillations. The inertial component of the flow is calculated by subtracting the prescribed background current profile from the model output and then horizontally averaging:

$$(\overline{u}, \overline{v}, \overline{w}) = \frac{1}{n_x} \sum_{0}^{n_x} (u - U(z), v, w)\delta x, \tag{3.3}$$

where n_x is the number of grid points in the x-direction. The velocity perturbation fields (u', v', w') are:

$$u' = u - U(z) - \overline{u}, \tag{3.4}$$

$$v' = v - \overline{v}, \tag{3.5}$$

and

$$w' = w - \overline{w}. \tag{3.6}$$

The density and pressure perturbations, (ρ', p'), are calculated similarly, except that there are no inertial profiles for these quantities. The energy budget is calculated away from topography and the surface, from a depth of $z = -2750$ m to $z = -250$ m to exclude boundary phenomena. Horizontally, the energy budget is calculated over the width of the simulation domain, i.e. two bathymetric length scales.

3.2.3 Time Averaging

Although lee wave dynamics are often thought to be steady in time, wave reflection and interactions of upwards and downwards propagating waves and the development of inertial oscillations bring a time dependency to the model outputs. As mentioned above, an analysis time of $t_a = 1.5t_p$ is set to ensure dynamical similarity between the simulations. Below, some results are presented at the analysis time. However, quantitative results must be time-averaged to make a general statement about wave dynamics due to the presence of time variability. Unless specified otherwise, model results are averaged from the ramping-up time to the analysis time for simulations BIC1.4km to BIC7km and over the last inertial period for simulations BIC13km to BIC72km. These two different averaging windows are chosen because the analysis time of the first four simulations is smaller than an inertial period. For the last four simulations, since no total reflection is happening in the domain, time variability mostly comes from inertial oscillations. Therefore, averaging over an inertial period removes this time dependency. Only one inertial period is considered for the average since the length of simulation SIC13km only allows for one complete inertial period.

3.3 Results

3.3.1 Wave Velocity Predictions

Lee wave bottom velocity predictions are made using equations 2.18 and 2.19. The numerical magnitude is the maximum of the time and vertically averaged velocity perturbation. The time average is described in section 3.2.3. The vertical average is taken 50 m above bathymetry, from $z = -2955$ m to $z = -2805$ m. The numerical model results are generally similar to the theoretical predictions for the vertical and x-direction velocities, with values slightly higher than predicted (figure 3.3). For the x-direction velocity, u', and the vertical wave velocity, w', the model wave velocities are 1 to 2.5 times larger than theoretical values. For the y-direction velocities, simulation BIC1.4km shows the most significant discrepancy as the model output is 14 times larger than predictions. The largest disparities for the x-direction velocity predictions are also associated with smaller length scales. These differences are likely caused by the time average, which does not cover an entire inertial period for these simulations.

The changes in the magnitude of the x-direction velocity as the topographic scales vary are smaller than those for the y-direction and z-direction velocities. When looking at theoretical velocities for waves produced over the largest scale to the smallest scale, x-direction velocities range from $u'_{b,BIC72km} = 0.01$ m/s to $u_{b,BIC1.4km} = 0.03$ m/s, y-direction velocities range from $v_{b,BIC72km} = 1 \times 10^{-4}$ m/s to $v'_{b,BIC1.4km} = 6 \times 10^{-3}$ m/s and vertical velocities vary from $w'_{b,BIC72km} = 0.02$ m/s to $w'_{b,BIC1.4km} = 4 \times 10^{-4}$ m/s. These changes in magnitude can be seen in figure 3.4 and 3.5 as the horizontal wavefield becomes darker for larger lengthscales and lighter for the vertical velocity. The numerical model shows overall agreement with the theoretical predictions as the magnitude of numerical velocities generally agrees with theoretical predictions and follows the same spatial trends.

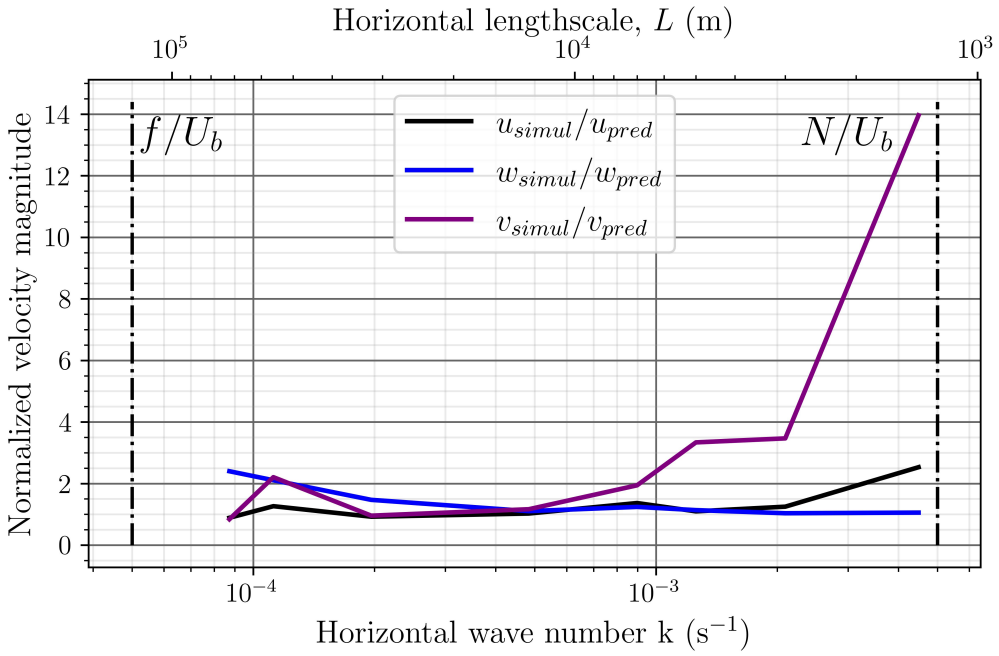

Figure 3.3: Bottom numerical velocities normalized by theoretical wave velocities for the different BIC simulations. The left-most point is associated with BIC72km, and the right-most point with BIC1.4km. The Coriolis parameter and buoyancy frequency are normalised by the background current above bathymetry, $U_b = 0.2$ m/s.

3.3.2 Wave Field

The theoretical dissipative layer depth calculated using ray tracing is $z_d \approx -19$ m, $z_d \approx -842$ m and $z_d \approx -1394$ m for simulations BIC32km, BIC56km and BIC72km,

respectively, which fits with results as the wave velocities u' and v' abruptly decrease above within 500 m of predicted level (figure 3.4, black dotted line, second and last column). The lines of constant phase flatten and disappear. The impact of the dissipative layer is also visible in the wave kinetic energy, where little to no energy remains above the dissipative layer, marked by the greyed areas in figure 3.5). The horizontal black line marks the theoretical dissipative layers, and the greyed zones represent the numerical dissipative layer. The thickness of the dissipative layer is further discussed in section 3.3.3.2. Above the dissipative layers, the wave field is not fully evanescent, and some energy can still be seen. This is likely caused by the multichromatic wave field generated by the development of inertial oscillations. The proximity of the dissipative layer to the surface makes simulation BIC32km harder to interpret as some energy is reflected downwards at the surface.

Theory predicts that the lines of the constant phase are perpendicular to the energy path and flatten with height, illustrated by the coloured stripes on figure 3.4 for all simulations, except for BIC32km. This trend is not evident for simulation BIC32km, as the lines of constant phase are broken by two horizontal stripes presenting enhanced y-direction wave speed at a depth of $z = -2250$ m to $z = 2000$ m and $z = -1250$ m to $z = -750$ m. Wave-IO interactions cause the horizontal stripes and are further discussed in the next section. For all the propagating simulations at the analysis time, the energy has reflected from the surface and travelled down 700 m. Upward and downward propagating wave interactions are only captured for this top layer. This is identifiable by the checker-board pattern and breaking down of the phase lines in this layer for simulation BIC1.4km to BIC13km.

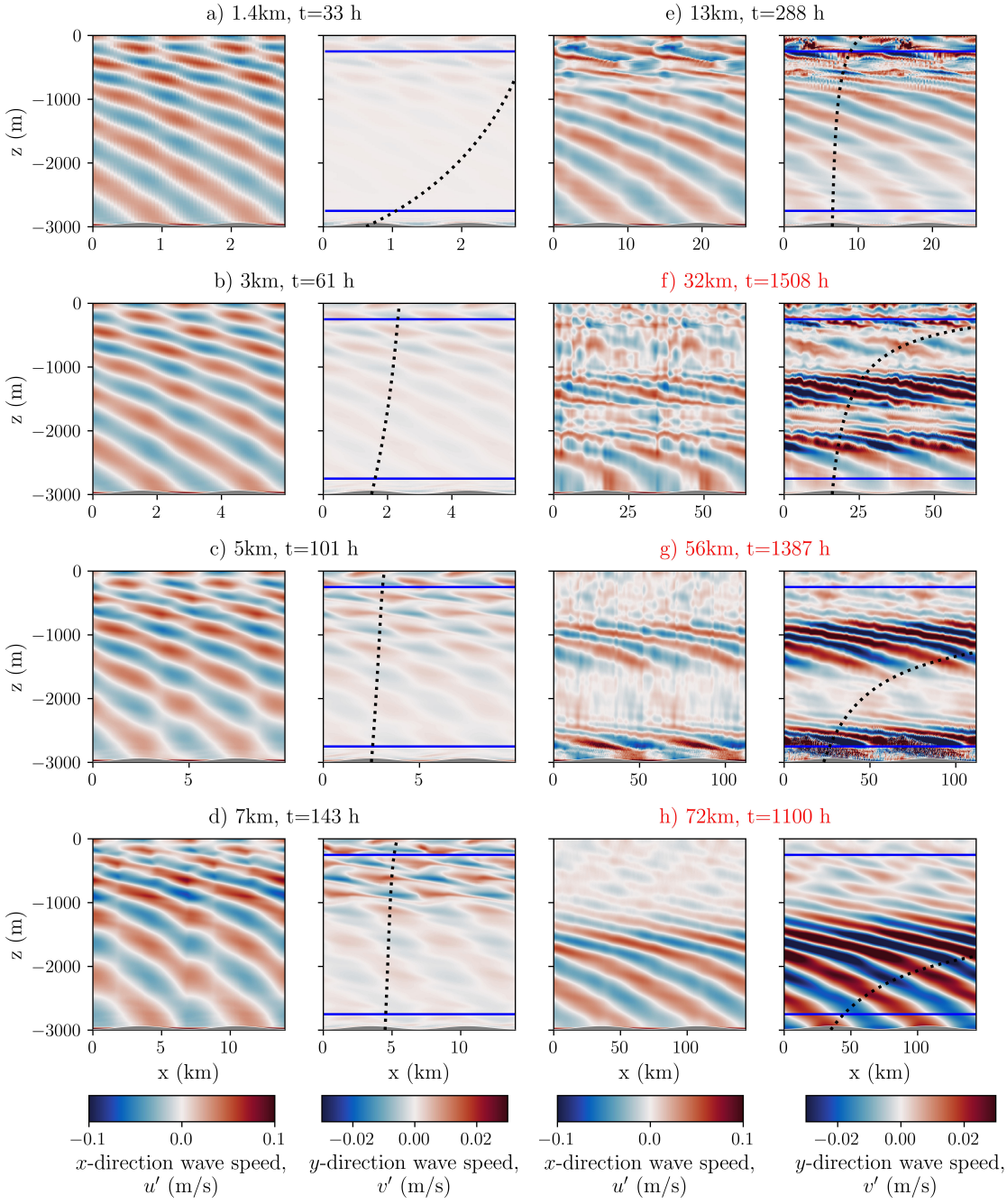

Figure 3.4: (Left) Wave velocity in the x-direction, u' (m/s) for all simulations, (Right) wave-velocity in the y-direction v' (m/s) and energy path (black dotted line) at the analysis time. The titles for the dissipative simulations (BIC32km to BIC72km) are red. The blue and red strips illustrate the lines of constant phase of the wave. Simulations BIC32km to BIC72km have a dissipative layer where the ray path (black dotted line on the right panels) flattens. Above the critical layer, the wave velocities are smaller. In the propagating domain, larger horizontal velocities are associated with smaller topographic wave numbers. Across all wavenumbers, the variations in y-direction velocities are an order of magnitude and the order of (mm/s) for x-direction velocities.

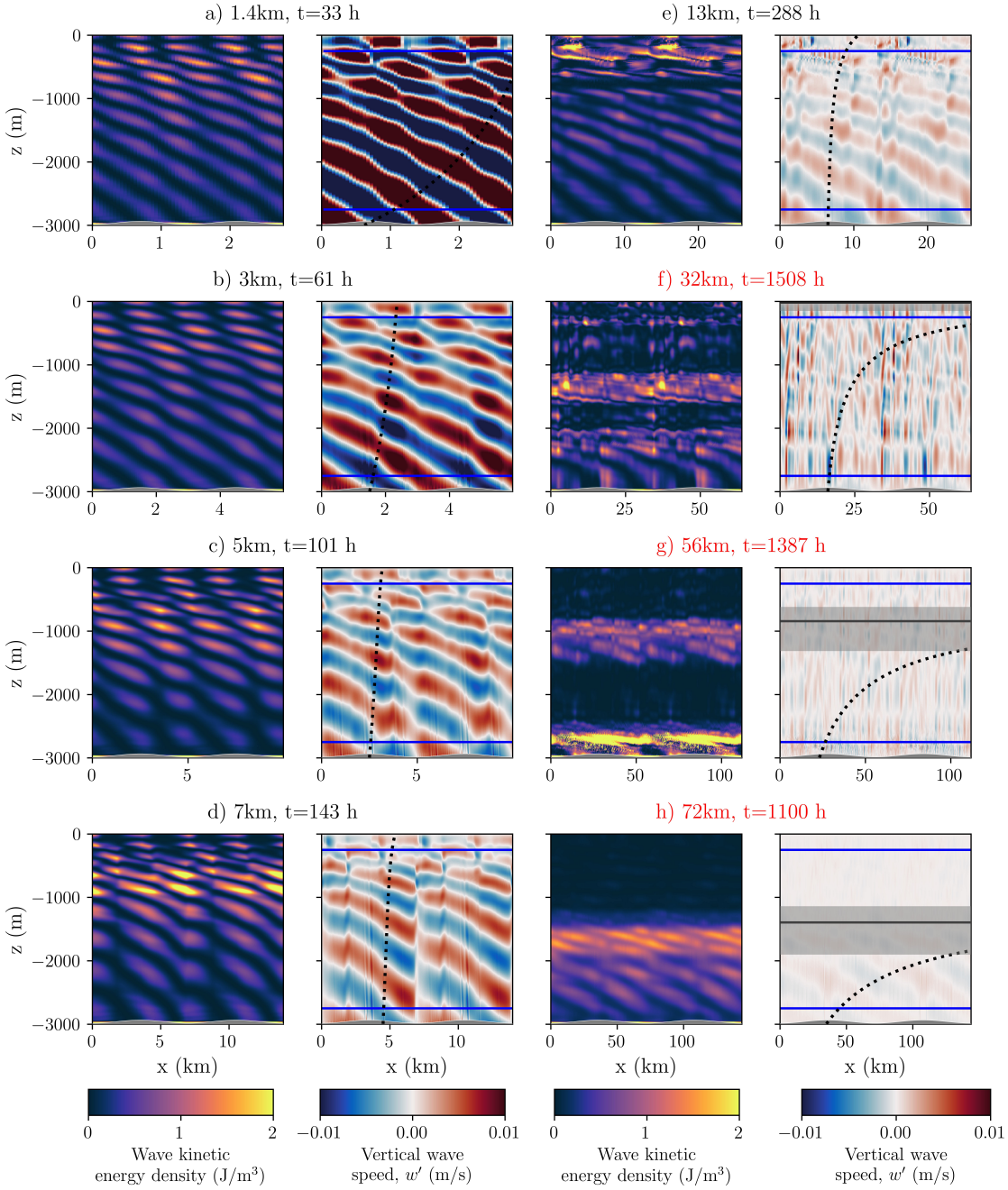

Figure 3.5: Similar to figure 3.4, but for the wave kinetic energy density (J/m^3) (first and third columns) and the vertical velocity w' (m/s) and energy path (black dotted line) (second and last column). Simulations BIC32km to BIC72km (red titles) have a dissipative layer where the ray path (black dotted line on the right panels and grey zone) flattens. Most of the wave energy vanishes above this layer. The magnitude of the vertical wave velocity decreases as the lengthscales increase.

3.3.3 Energetics

The kinetic energy budget for all simulations from the ramping-up time to the analysis time (BIC1.4km to BIC7km) or over the last inertial period (BIC13km to BIC72km) is presented in figure 3.6. The most significant terms of the energy budget, i.e. the wave K time derivative (blue line), the divergence of the energy flux (black line), the background and inertial energy shear production (green solid and dotted lines, respectively), and the buoyancy production (purple line), as well as the K dissipation (cyan line), are plotted on figure 3.6. For clarity, the other terms in equation 2.21 are not included in the figure as they are small. The budget residue is calculated, time-averaged and normalized by the magnitude of the divergence of the energy flux. A |10%| bound assesses whether a budget is closed. Table 3.2 presents the normalized residue. All budgets are considered closed. The larger residue for BIC56km is due to the growth of instabilities in the model, starting around 1200h. When the residue is calculated over the last inertial period before 1200h, it reduces to 0.03%.

Table 3.2: Time averaged energy budget residue, normalized by the magnitude of the energy flux divergence. The average is taken from the ramping-up time to the analysis time (BIC1.4km to BIC7km) or over the last inertial period before the analysis time (BIC13km to BIC72km).

	BIC1.4km	BIC3km	BIC5km	BIC7km	BIC13km	BIC32km	BIC56km	BIC72km
Residue	11.8%	7.53%	7.44%	5.53%	4.53%	3.57%	7.74%	2.06%

The background shear production term is negative for all simulations, consistent with the theoretical predictions that lee waves lose energy to the background current. The dominant term in each budget is the energy flux divergence, and its magnitude decreases with the horizontal wave number. This reflects theoretical predictions of energy flux (figure 3.1). The potential kinetic energy transfer term, $-w'\rho'g$, oscillates in time and often changes sign. The time derivative of the wave kinetic energy is also time-dependent, meaning that there is a net gain or loss of kinetic energy from one time step to the other. The time derivative of kinetic energy and the potential to kinetic energy transfer follow similar time patterns, often overlapping and balancing each other out. The divergence of the energy flux and background shear

production shows similar time variability but with opposite signs. The magnitude of the shear production is closer to the magnitude of the flux divergence for the propagating simulations, qualitatively showing a larger exchange fraction than simulations BIC32km to BIC72km. On the other hand, the energy dissipation is larger for the dissipative simulations. This was expected as theory predicts that waves encountering dissipative layers deeper in the water column will lose less energy to the sheared current, resulting in a larger fraction of energy left to dissipate. Wave-IO interactions also cause enhanced dissipation as the inertial oscillations are fully developed in these simulations. Finally, the budgets from the smaller length scale simulations are more energetic than the larger ones, with energy term magnitude ranging from ± 0.15 W/m^2 to ± 0.002 W/m^3.

3.3.3.1 Shear Production

Over time, the normalized integrated background shear production, $-u'w'\frac{dU}{dz}$ is negative for all simulations and averages from -0.0005 W/m^2 for BIC72km to -0.0304 W/m^2 for BIC1.4km, consistent with theoretical expectations that the shear production is an energy sink for the wave. The Hovmoller diagram of the horizontally averaged shear production profiles shows energy loss to the background current (blue, negative values) over the propagation depth (figure 3.7).

The energy lost from the wave represents a transfer of momentum to the background current and will act to accelerate the latter. The percentage difference between horizontally and time-averaged background current and the initial profile shows an acceleration of the background current over most of the water column (figure 3.8). The time average is taken over the last inertial oscillation to isolate the background changes from the effects of the IO. Only simulations BIC13km to BIC72km are shown, as the other simulations were not run long enough for IO to fully develop. Simulations BIC13km to BIC72km normalized profiles are $\approx 2\%$ larger than the initial value, indicative of a background acceleration. The vertical variability of the percentage difference profile shows the generation of horizontal jets in the water column.

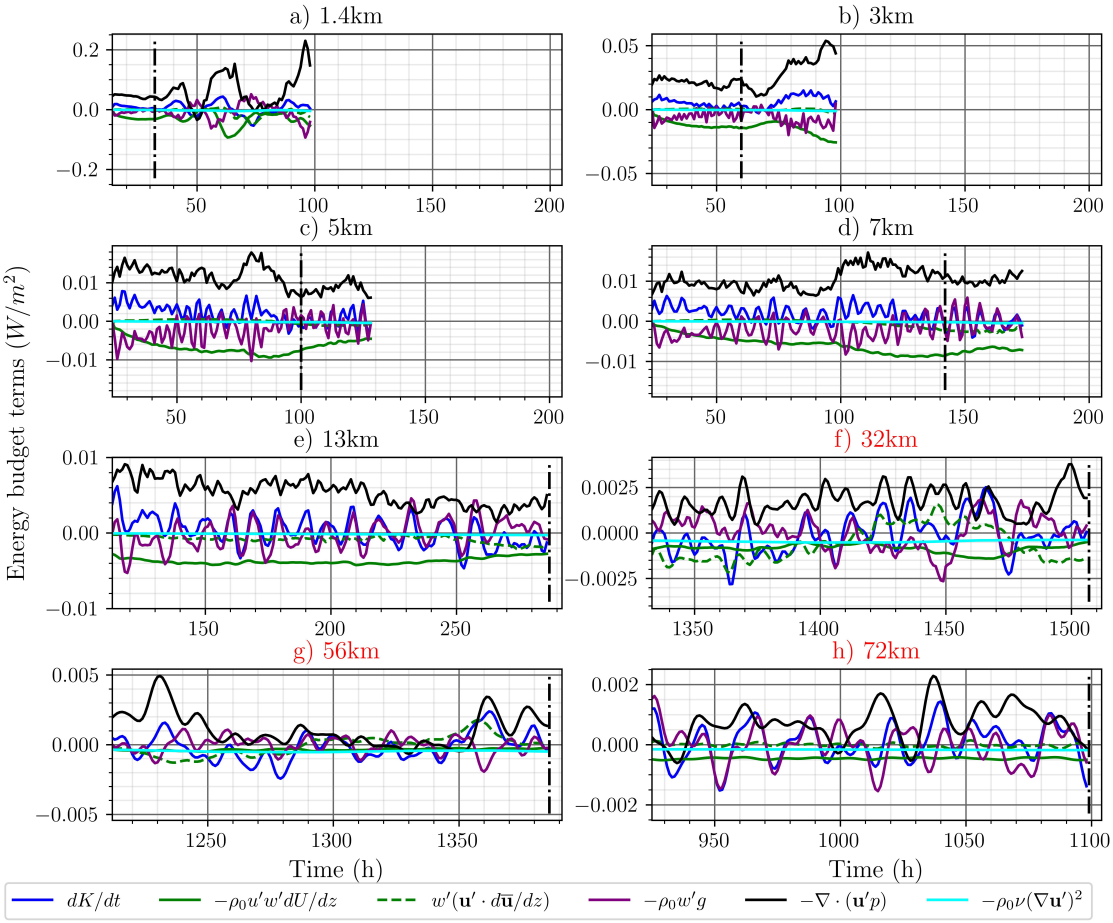

Figure 3.6: Kinetic energy budget normalized by the length of the integration domain. The complete simulated time series is presented in panels a) to e), and panels f) to h) present the last inertial period. The vertical black line delimits the analysis time for each simulation. The magnitude of the energy terms decrease as the bathymetric scale increases, with energy peaks around ± 0.15 (W/m^2) for simulations BIC1.4km and BIC3km to ± 0.002 W/m^2 for BIC72km. The dominant terms in these budgets are the time derivative of kinetic energy (blue), the buoyancy flux (purple), the shear production from the background current (green) and the divergence of the energy flux (black). The shear production from the RHAC (dotted green line) is large for simulation BIC32km (f). Energy dissipation stands out in panels f), g) and h) (light blue and grey lines). This enhanced energy dissipation is due to the dissipative layer, wave-mean flow and wave-wave interactions. Red titles are associated with dissipative simulations.

3.3.3.2 Wave-Inertial Oscillation Interactions

As shown by *Nikurashin and Ferrari* (2010a), the breakup and dissipation of internal waves trigger inertial oscillations, which we observe in this set of simulations. A spectrum for the de-meaned horizontally averaged current perturbations, $\overline{u}$ for simulation BIC32km is shown in figure 3.9 a). The power spectra were calculated

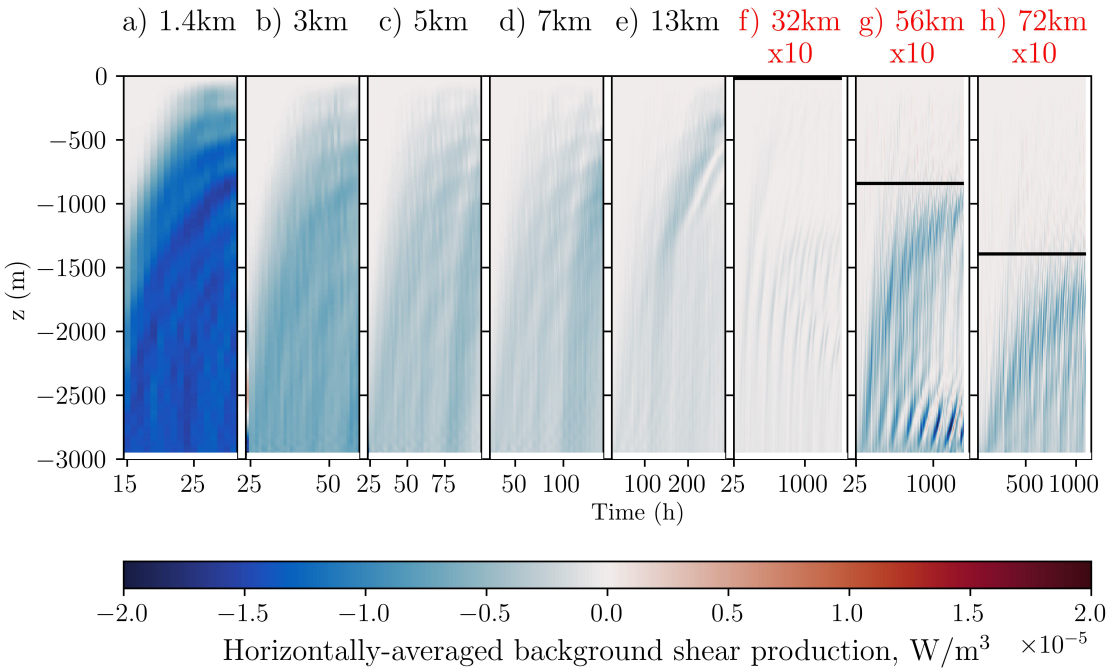

Figure 3.7: Horizontally averaged shear production profiles in time. The horizontal average is calculated over the width of the energy budget domain. The wave is losing energy to the background current. After 50 h, vertical modes appear in the domain.

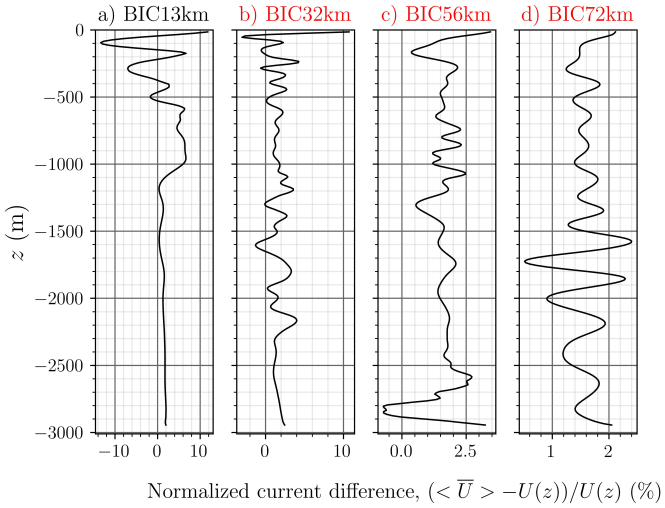

Figure 3.8: a) to d) Horizontally and time average difference percentage between the background field and the initial background current. Simulations BIC1.4km to BIC7km are not shown as they were not run long enough for near-inertial oscillations to fully develop and be removed by time averaging.

by averaging together spectra calculated at each vertical point in the integration domain. A total of 250 spectra are averages for each simulation. The inertial

oscillations are well captured by the horizontal average of the velocity perturbation field, with the dominant frequency being close to the Coriolis parameter (figure 3.9). This phenomenon is observable in all simulations. For simulations that were run for less than 174 h, i.e. the inertial period, IO is still triggered but has not fully developed. Thus, they are not captured properly by the spectrum analysis. However, when plotting the inertial components of the current, a good fit is observed between inertial current magnitudes and periods. Inertial oscillations develop in all simulations, which can be seen in the y-direction RHAC as the magnitude and time variability of this component is similar for the BIC5km simulation to the BIC72km simulation (figure3.9b). For clarity, only two simulations are presented because the results are similar between all eight study cases.

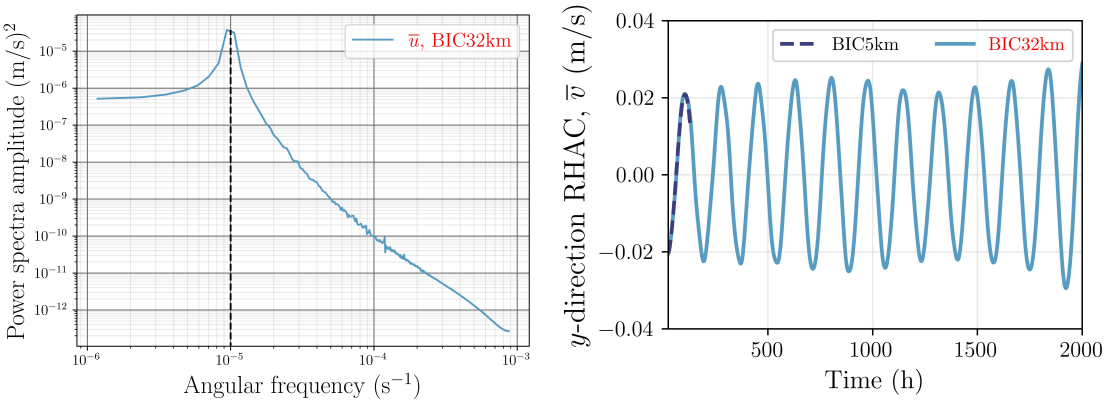

(a) (b)

Figure 3.9: (a) x-direction RHAC, $\overline{u}$, power spectrum for BIC32km. The Coriolis frequency is $f = 10^{-5}$ s^{-1}, which corresponds to the largest peak of the spectra and is marked by the vertical dashed line. (b) Magnitude of the RHAC averaged over the bottom 50 m above bathymetry for simulation BIC5km and BIC32km. An incomplete inertial oscillation can be seen for simulation BIC5km. The magnitude of the oscillation changes slightly with time for BIC32km.

With the total flow field separated in a linear background current, wave perturbations and an inertial current, $\mathbf{u}_t = U(z) + \mathbf{u}' + \overline{\mathbf{u}}$, a production term associated with the inertial component appears in the energy equation. At the analysis time, the normalized integrated RHAC production is negative for all simulations. The RHAC profiles are of the same order of magnitude as the background shear production profiles (figure 3.10). They show positive and negative values, meaning lee wave both

gains and loses energy from and to the inertial oscillations. RHAC shear production is strong in areas associated with enhanced energy dissipation (see figure 3.11). This is expected since energy dissipation acts to trigger inertial oscillations and the horizontally-averaged residual current is mostly inertial.

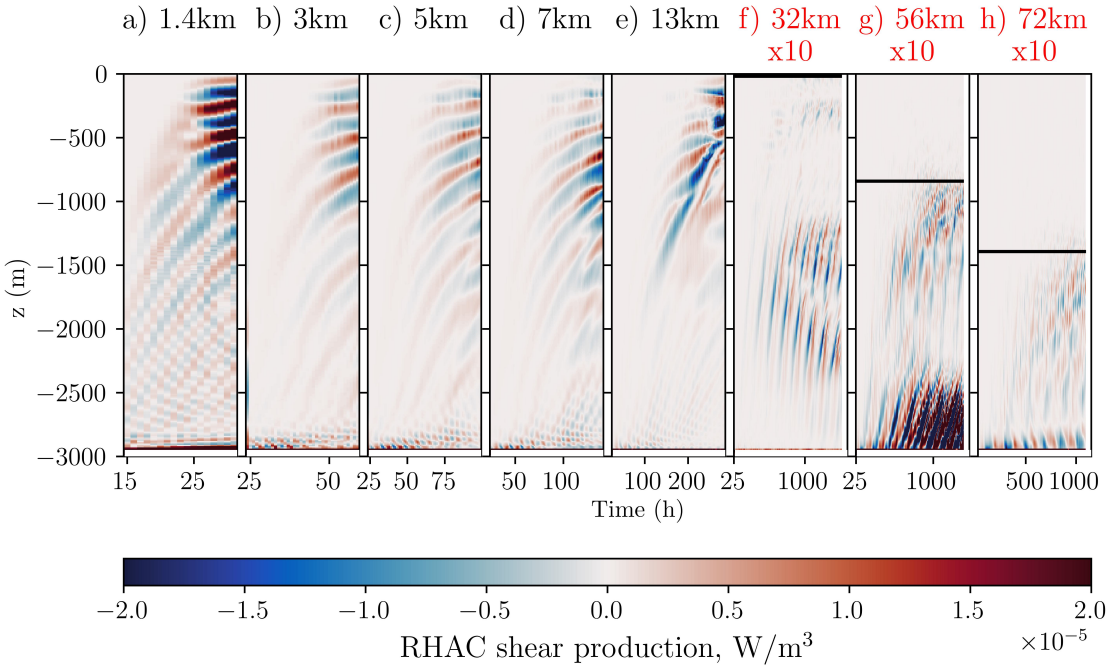

Figure 3.10: Like figure 3.7, but for the inertial shear production. The values are of the same order of magnitude as the background shear production and present vertical modes, meaning that the lee waves both gain and lose energy from the inertial current.

Finally, the magnitude of the inertial current is relatively small compared to the background current(figure 3.8 and 3.9). However, it is strong enough to accelerate and decelerate the background flow. In turn, this affects the lee wave generation frequency. The wave field is then composed of lee waves of different generation frequencies with different propagation and dissipation depths. Table 3.3 compiles the minimum and maximum vertically averaged current speed above bathymetry, the wave generation frequency associated with these currents and the resulting propagation depth. The vertical average is taken 50 m above bathymetry and the time average over the periods presented in section 3.2.3. The theoretical depth range of the dissipative layer presented in table 3.3 fits with the numerical depth of the dissipative layer as highlighted by the greyed zones on figure 3.5.

Table 3.3: Minimum and maximum values of the background current near bathymetry, the generation frequency and propagation depth

	Minimum bottom current U_{min} m/s	Maximum bottom current U_{max} m/s	Minimum generation frequency Ω_{bmin} $\times 10^4$ s^{-1}	Maximum generation frequency Ω_{bmin} $\times 10^4$ s^{-1}	Minimal propagation depth h_{pmin} m	Maximal propagation depth h_{pmax} m
BIC1.4km	0.17	0.20	≈ 7.6	≈ 8.98	0	0
BIC3km	0.18	0.19	≈ 3.7	≈ 3.98	0	0
BIC5km	0.18	0.21	≈ 2.14	≈ 2.64	0	0
BIC7km	0.18	0.22	≈ 1.53	≈ 1.06	0	0
BIC13km	0.17	0.22	≈ 0.87	≈ 0.30	0	0
BIC32km	0.17	0.22	≈ 3.3	≈ 0.43	≈ -23	≈ -16
BIC56km	0.16	0.24	≈ 0.18	≈ 0.27	≈ -1067	≈ -618
BIC72km	0.17	0.22	≈ 0.15	≈ 0.19	≈ -1140	≈ -1615

3.3.3.3 Energy Dissipation

Energy dissipation is seen in all simulations, particularly close to the surface for the freely propagating simulations, BIC1.4km to BIC13km, and near the dissipative layer for simulations BIC32km to BIC72km (figure 3.11). Simulation BIC56km shows dissipation near the topography, and simulation BIC32km, in the middle of the water column. The enhanced dissipation seen in the top 700m of figure 3.11 a) to e) could be attributed to interactions between upward propagating and downward reflected waves. For all these simulations, the analysis time is almost equal to the time it takes for the wave to travel to the surface and back to a depth of $z \approx -700$ m. Therefore, the analysis does not capture the interactions of downward and upward propagating waves and their impact on energy dissipation below 700 m. As expected for simulations BIC32km to BIC72km, energy dissipation is high below the dissipative layer. A vertical spread of enhanced energy dissipation near the predicted dissipative layer is illustrated by the red patches underneath the greyed zones in figure 3.11. First, the time and spatial variations of the background current due to the IO generate wave packets with a different generation frequency, thus propagating to a different dissipative depth. Second, the lee waves become unstable when they reach a near-inertial frequency. The near-inertial band is bounded by frequency greater or equal to 10% of the Coriolis frequency following *Garrett* (2001). With the 10% bound and the range of generation frequencies, the thickness of the

dissipative layers spans from the depth at which the lee wave frequency equals $1.1f$ to the dissipation depth of the highest generation frequency. This interval, shaded in grey on figure 3.11, overlaps with the areas of enhanced dissipation. The dissipation peaks in the middle of the water column for f) and near the bathymetry for g) fit with zones of large vertical shear for the RHAC profile (see figure 3.8). The areas of enhanced energy dissipation are similar to the zones of higher kinetic energy density (see figure 3.5). The interaction of upward and downwards propagating waves causes the vertical modes present in the top 700 m of the propagating simulation. Lastly, when internal waves dissipate, they deposit their momentum. The force generated will then act to slow down the background current. This forcing is opposite to the background acceleration caused by the momentum gained from the shear production. A deceleration of the background current shown in figure 3.8 c) from $z = -2900$ m to $z = -2700$ m overlaps with the zone of enhanced dissipation on figure 3.11.

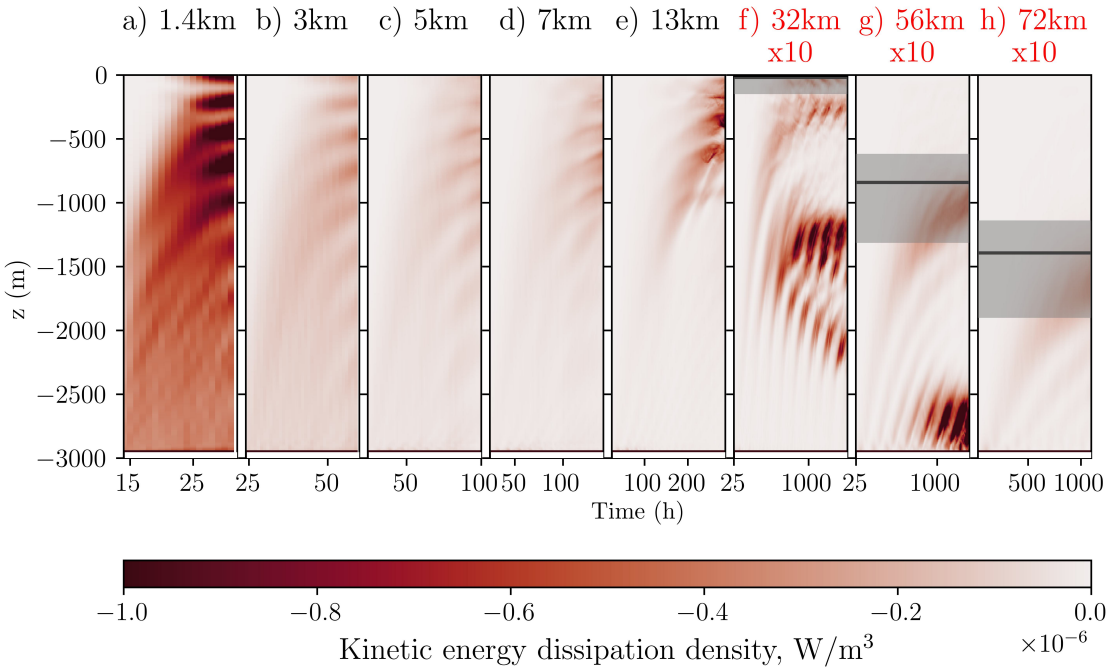

Figure 3.11: Energy dissipation profiles in time. The wave frequency is near-inertial in the shaded areas where $\Omega \leq 1.1f$, and the depth of the dissipative layer is illustrated by the coloured dot on the y-axis. Energy dissipation is high in the top 700m of the domain for the freely propagating simulations (a to e). There is enhanced energy dissipation under the dissipative layer in simulation BIC32km to BIC72km.

Predictions of the vertical distribution of energy dissipation were made for lee

waves propagating through depth-uniform current and state that 50% of the energy dissipation takes place in the layer 1000 m above bathymetry (*Nikurashin and Ferrari*, 2010a). For the propagating simulations, most of the dissipation occurs near bathymetry in the absence of wave reflection from the surface (figure 3.12). For simulations with a dissipative layer, the theory predicts that most energy dissipation will occur near the critical layer. However, enhanced dissipation is seen in the middle band for BIC32km and near bathymetry for BIC56km, with neither of these regions containing the simulation's dissipative layer. This enhanced dissipation also correlates to large inertial current shear. Finally, simulation BIC72km shows enhanced dissipation in the middle band, which includes the dissipative layer. When comparing the kinetic energy dissipation distribution, inertial oscillations dominate the dissipative processes over dissipative layers for simulations BIC32km and BIC56km. Dissipative fractions are ten to twenty times larger for the dissipative simulations than the propagating ones (figure 3.12). The enlarged dissipative fractions are due to IOs and the dissipative layer.

3.3.4 Comparison with Depth-Uniform Current

Two additional simulations were run with a depth-uniform current to compare and evaluate the impacts of BICs. Simulations with lengthscales of 5 km and 72 km, respectively named BNS5km and BNS72km, were run. The numerical setup is identical to the BIC simulations. The propagation time is $t_p = 17$ h for simulation NS5km. For the BNS72km simulation, $t_p = 433$ h. The BIC simulation's analysis time is chosen to be the same for both the depth-uniform and depth-varying current simulations. The 5 km simulations are time averaged over 101 h, and the 72 km simulations are averaged over the last inertial oscillation, from $t = 925$ h to $t = 1100$ h. Results are only shown for the kinetic energy and dissipation, as the other energy terms follow similar patterns. First, depth-varying currents slow down the vertical group velocity, as shown by the faster propagation time for the depth-uniform simulations (based on equation 2.11). As expected, the depth-uniform simulations K profiles show vertical modes since the analysis time allows for approximately three reflective cycles for both lengthscales (figure 3.13). Comparatively, BIC5km shows enhanced vertical variability due to wave reflection

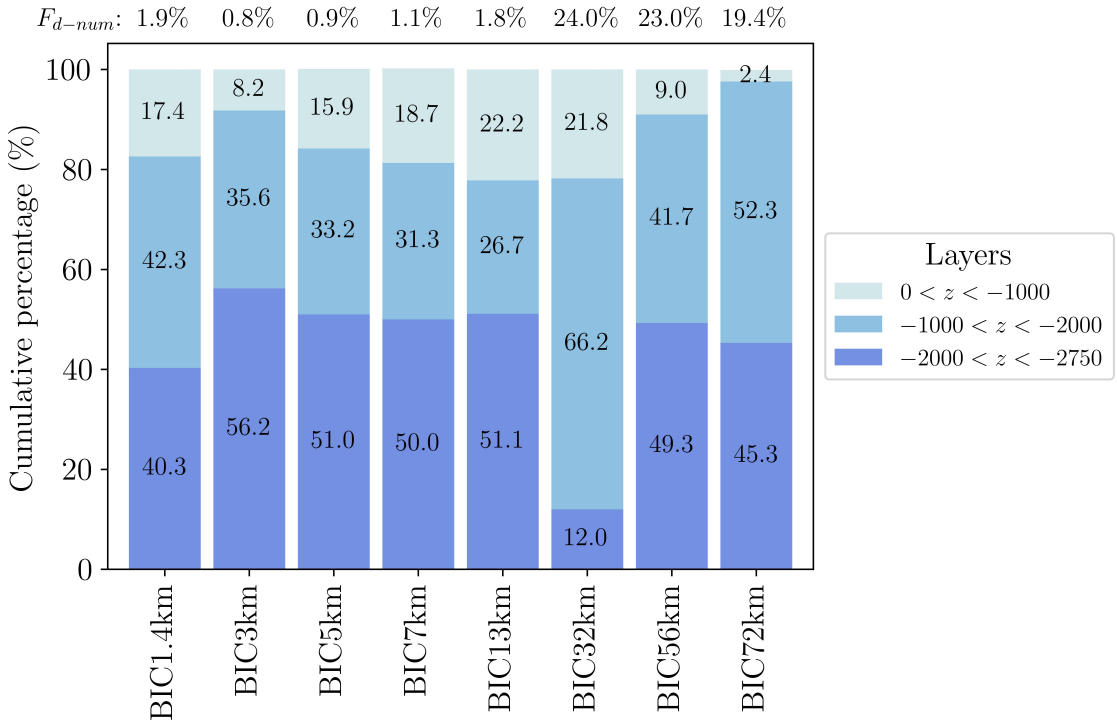

Figure 3.12: Distribution of the kinetic energy dissipation. Energy dissipation is integrated in bins of 1000 m and normalized by the total K dissipation in the domain. The dissipative fraction, i.e. the ratio of kinetic energy dissipation to energy flux into the domain, is indicated for each simulation. Quantities are time-averaged from the ramping up time to the propagation time for the propagating simulations and over the last inertial oscillation before t_p for the dissipative simulations.

in the top 700 m of the domain, which corresponds to the propagation depth at the analysis time. Discrepancies between K density near bathymetry show that wave reflection influences lee wave generation (figure 3.13a). For simulation BIC72km, K is enhanced below the dissipative layer, illustrating energy accumulation caused by the decrease of the vertical group velocity with height. Kinetic energy density is an order of magnitude smaller above the dissipative layer, confirming the evanescent field. This contrasts with the BNS72km simulation, which presents K throughout the water column.

As for the kinetic energy dissipation, the non-sheared simulations present enhanced dissipation in the bottom 1000 m, and dissipation rates decrease with height (figure 3.13b). Dissipation is more evenly distributed over the water column for the propagating BIC simulation, BIC5km. However, results are averaged over $1.5t_p$, and

the downward reflected energy has only travelled 700 m. The topmost layer then contains upward and downward propagating energy, which may bias the energy dissipation percentage. The impact of the dissipative layer is evident for BIC72km, with 67.8% of the energy dissipating in the middle layer, which includes the dissipative layer. Furthermore, energy dissipation is reduced in the top 1000 m, consistent with the evanescent wave field. The dissipative fraction is more significant for the BNS5km simulation than for the BIC5km one, likely caused by interactions of upward and downward propagating waves. As for the larger scale simulations, the dissipative fraction is larger for the BIC72km than for BNS72km, highlighting the impact of the dissipative layer.

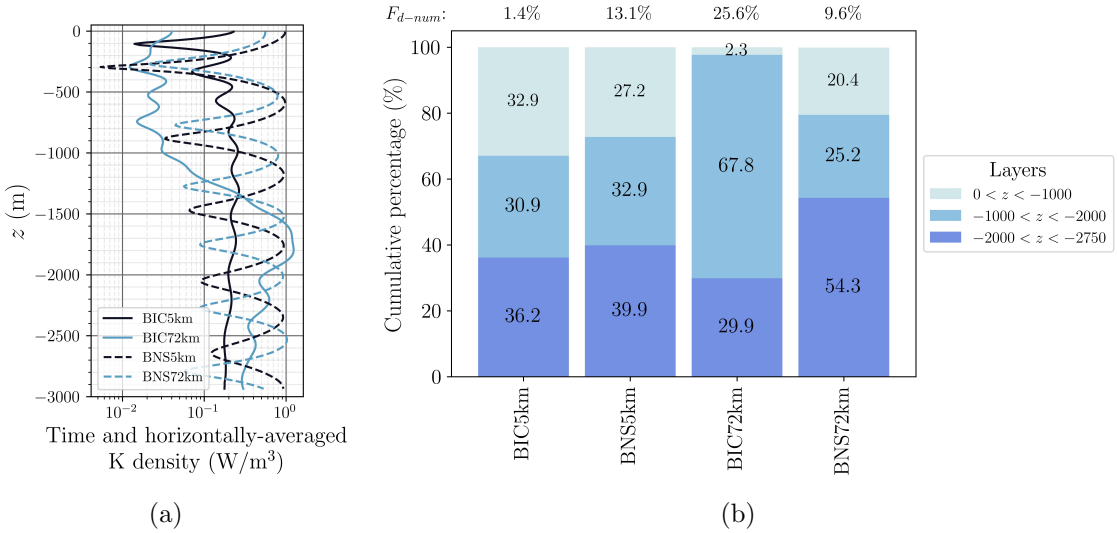

Figure 3.13: a) Horizontally averaged kinetic energy profiles. The profiles time-averaged over 101 h for the 5 km lengthscales simulations and over the last IO before the BIC72km analysis time, i.e. from $t = 925$ h to $t = 1100$ h for the 72 km simulations. b) Vertical distribution of energy dissipation. Energy dissipation is integrated in bins of 1000 m and normalized by the total K dissipation in the domain.

3.3.5 Comparison with Kunze and Lien (2019)

Kunze and Lien (2019) inspired this thesis as one of our goals is to evaluate the theoretical predictions presented in this paper. The idealized ocean conditions underlying *Kunze and Lien* (2019) predictions are an infinitely deep ocean where every lee wave generated propagates inviscidly, where energy is lost to the background

by shear production until the wave reaches a dissipative layer, where the remaining energy is dissipated (figure 3.14). However, the numerical setup used for the BIC simulations differs from this idealized ocean. First, dissipation is allowed everywhere in the water column. Second, not all waves reach a dissipative layer; some waves reach the surface and reflect downwards. Finally, the energy equation 2.20 shows that the energy budget includes more terms than the energy flux, exchange and dissipation. One obvious example is inertial shear production, another exchange term which has a magnitude similar to the shear production (as shown in figure 3.10).

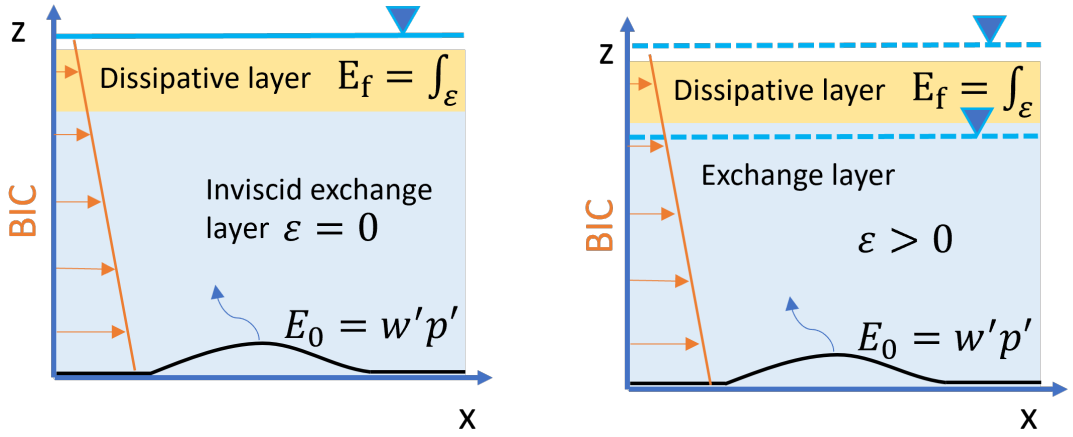

(a) (b)

Figure 3.14: (a) World view from Kunze and Lien. (b) A more realistic world view where the sea surface, marked by the dashed blue line and inverted triangle, can be situated below or above the dissipative layer.

Dissipative and exchange fractions are calculated by *Kunze and Lien* (2019) based on wave action, which states that the changes in energy with depth are proportional to the wave action multiplied by the wave frequency :

$$\mathscr{A}\Omega(z) \propto E.$$

Therefore, the exchange fraction, F_e, is defined as:

$$F_e = \frac{E_0 - E_f}{E_0} = \frac{U_0 k - f}{U_0 k}, \tag{3.7}$$

and the dissipative fraction, F_d, as:

$$F_d = \frac{E_f}{E_0} = \frac{f}{U_0 k} \tag{3.8}$$

where E_0 is the energy flux above bathymetry, E_f the minimal energy available for dissipation. If a wave propagates to the surface without encountering a dissipative layer, the upper bound of the wave frequency becomes its value at the surface. A modified exchange fraction, F_{em}, is then expressed as:

$$F_{em} = \frac{U_0 k - U_{z=0} k}{U_0 k}. \tag{3.9}$$

Dissipative and exchange fractions are calculated from the model output and compared to values predicted with the above-modified exchange fraction (figure 3.15). Data is averaged from the ramping-up time to the propagation time to ensure that no wave reflection is included in these calculations, as the modified exchange fraction neglects it. The dissipative fraction is expected to be null for the propagating simulations BIC1.4km to BIC13km, as no dissipative layer is encountered in the water column.

Numerical results agree poorly with theoretical predictions with exchange and dissipative fractions not adding up to and not matching the modified fractions (figure 3.15). This is not surprising considering the idealized setup upon which these theoretical predictions are based. The simulated exchange fraction is relatively constant across length scales. It varies from 45% to 65%, which is lower than predicted for the propagating simulations and higher than predictions for the dissipative ones. The exchange fraction does not decrease significantly for the dissipative simulations. However, the dissipation fraction is one order of magnitude larger for the dissipative simulations than the others. This does not highlight the impact of the dissipative layer, as simulations BIC32km and BIC72km showed enhanced dissipation below the dissipative layer, where inertial shear production is large.

3.3.6 Sea Surface Anomaly

Lee waves propagating to the surface are expected to affect the sea surface level and leave a trace with a horizontal lengthscale similar to the bathymetric scale.

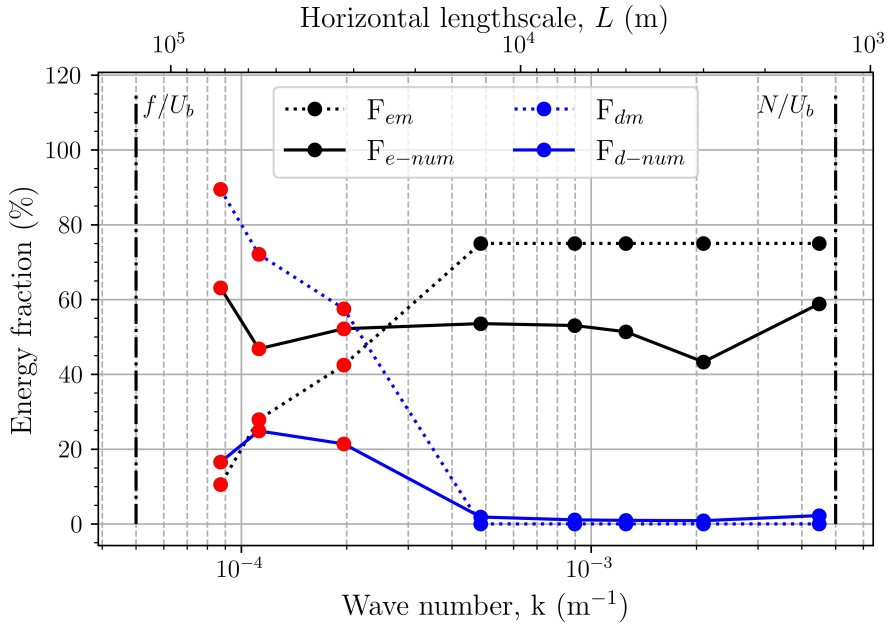

Figure 3.15: Comparison between theoretical and numerical exchange and dissipation fractions. (Dotted lines) Theoretical exchange and dissipative fractions as predicted by the modified *Kunze and Lien* (2019) equation (eq. 3.9) accounting for a finite depth ocean. (Solid lines) Numerical exchange and dissipative fractions. The red markers mark the dissipative simulations.

This is effectively the case for simulations BIC1.4km to BIC13km, as shown in figure 3.16. The sea surface anomaly (SSA) generated by the waves is similar to the bathymetry. Their amplitude is of the order of millimetres. For the waves encountering a dissipative layer within the domain, there should be no traces at the surface, as shown in figure 3.16. The proximity of the dissipative layer to the surface for BIC32km could explain the irregular undulations. SSA profiles were time-averaged.

3.4 Discussion

Ten idealized sinusoidal simulations were run to assess the impacts of bottom-intensified current on lee wave energetics and energy dissipation. First, model outputs from BIC simulations were compared to theoretical prediction for lee wave generation and showed overall good agreement (figure 3.3). Snapshots of the wave field display expected impacts of BIC, such as a flattening of the lee wave lines of constant phase with height, wave reflection and interference patterns for the propagation simulations

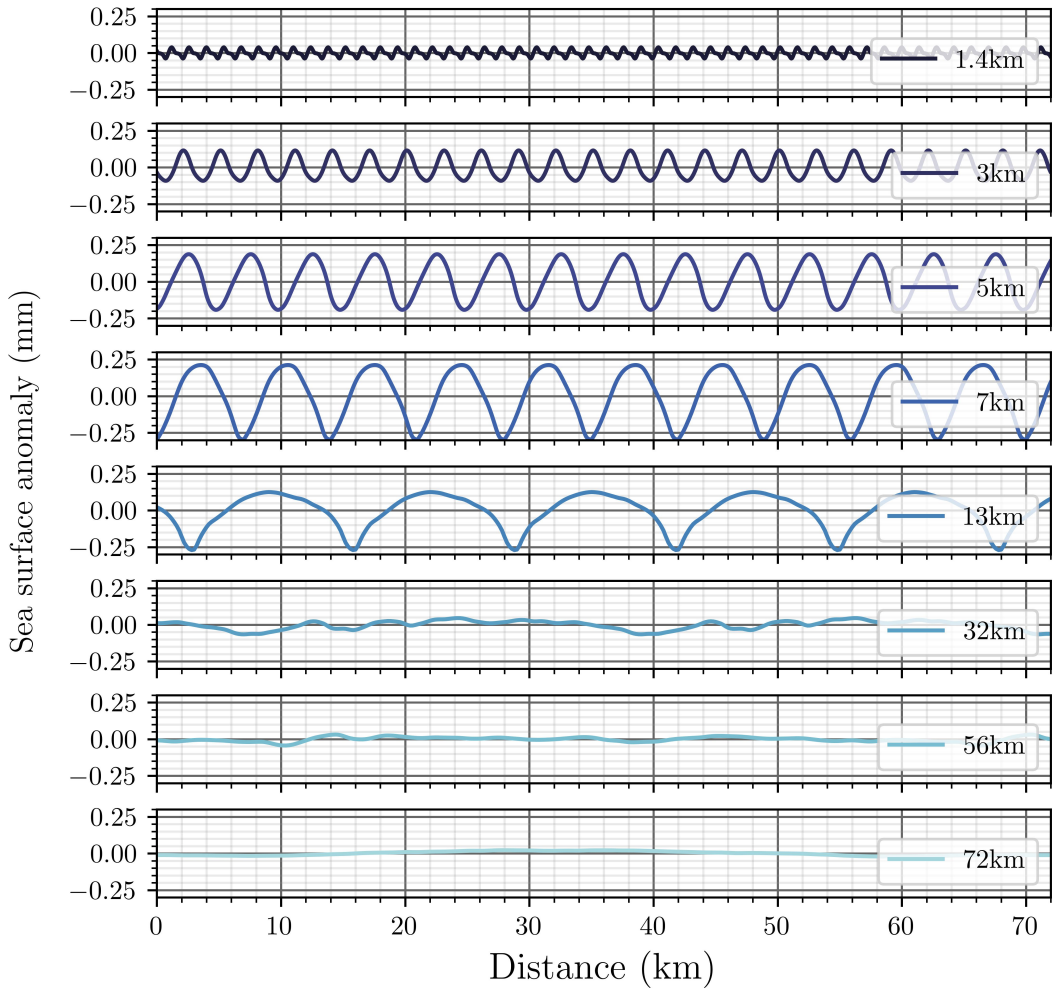

Figure 3.16: Sea surface anomalies. The profiles are irregular with rounded crests and angular through. Propagating simulations, BIC1.4km to BIC13km, present a surface trace, while dissipative simulations BIC32km to BIC72km do not.

and a dissipative layer where ray tracing predicted it (figure 3.4 and (figure 3.5)).

The energy budget has been calculated and closed with a residual smaller than 10% of the most significant energy term's magnitude, the energy flux divergence. The budget closure strengthens the calculations and the accuracy of each term. The larger residue observed for BIC56km is explained by the growth of numerical instabilities caused by small-scale phenomena not fully resolved at the scale of the simulation (see figure 3.4g). The negative shear production showed that the wave loses energy to the background flow (figure 3.7). The acceleration of the background current illustrates that the energy lost by the wave represents a momentum gain for the background

current (figure 3.8). Finally, the deceleration of the current in the bottom 250 m of simulation BIC56km correlates with a zone of enhanced dissipation, which hints that energy dissipation acts to slow down the background current. However, this interaction competes with the acceleration caused by the shear production, making it harder to quantify confidently.

The vertical distribution of kinetic energy dissipation is enhanced in the bottom 1000 m of the domain for the propagating simulations (figure B.2). For the dissipative simulations, dissipation is not necessarily dominant at the dissipative layer. For simulations BIC32km and BIC56km, enhanced dissipation zones correlate with enhanced inertial activity zones. To compare energy dissipation rates, literature often cites *Nikurashin and Ferrari* (2010b), who estimates that 50% of the lee wave energy is dissipated in the bottom 1000 m of the domain. This estimate is based on 2-D idealized sinusoidal simulations, combined with a depth-uniform current and a top sponge layer to prevent surface reflections. When reflection is not considered, results from the sheared propagating simulations agree with this prediction (figure B.2). The differences between the energy distribution, the dissipation predicted using a depth-uniform current and what has been calculated with these sheared simulations highlight the importance of including depth-varying currents and letting the energy propagate to the surface.

Two depth-uniform current simulations were run to compare energetics and dissipation for waves propagating over a 5 km and a 72 km lengthscales, covering the radiating regime and the dissipative regime. First, BIC acts to decelerate the vertical group velocity speed with height, which leads to slower propagation time compared to depth-uniform currents (based on equation 2.11). This alters the energy profiles as vertical modes develop and interference between upwards propagating and downwards reflected waves interact (figure 3.13). For the dissipative regime, kinetic energy accumulates under the dissipative layer as C_{gL-v} decreases with height. This leads to an enhanced area of energy dissipation where the dissipative layer is situated. Finally, energy dissipation is enhanced near bathymetry for the depth-uniform simulations, whereas the propagating simulation (BIC5km) presents a more evenly distributed dissipation profile.

Finally, model outputs do not agree with the *Kunze and Lien* (2019) predictions (figure 3.15). Considering how idealized these predictions were, it is not surprising that the numerical calculations differ. The energy equation and budget show the importance of some energy terms that were neglected by *Kunze and Lien* (2019) in the lee wave dynamics. For example, lee waves gain and lose energy to the inertial shear production throughout the water column (figure 3.10). Overall, the energy exchanged to the background current is relatively uniform between simulations, whereas the dissipative fraction is larger for the dissipative simulations (figure 3.15).

One major challenge associated with this set of simulations is the range of bathymetric scales. First, the length scales vary from 1.25 km to 125 km over the radiating domain. This affected the choice of horizontal resolution as the smaller length scales have a higher resolution to ensure the relative smoothness of the numerical bathymetry. The different lengthscales also introduce a time variability to the problem, where each wave propagates at a different speed, raising questions about the better analysis time. An analysis time of $1.5t_p$ was chosen to ensure dynamic consistency, and results were averaged over this period to smooth out the difference between time steps. However, the dynamic consistency results in the analysis times varying over two orders of magnitude, leading to the development of inertial oscillations in the longest simulations. For the simulations run long enough for IO to develop, averaging over the last inertial oscillation was chosen to remove inertial effects. Lastly, simulations SIC1.4km was ramped up over 14h, while the others were ramped up over 24h. Considering the analysis time, ramping up the simulation over 24 hours allows for a few hours of unforced data. As the research progressed, the pertinence of looking at unforced data for the upward propagating phase arose. Thus, simulation SIC1.4km was rerun with a ramping-up time of 14 h as a compromise on damping the sudden effect of starting the simulations and having non-forced data before the propagation time. The other simulations were not rerun due to time constraints. Time variability was also significant for the depth-uniform simulations. Results were averaged considering the analysis time of the BIC simulation, even if it means that the simulations are not dynamically consistent. This choice was made to limit the effects of the ramping-up period on wave dynamics, considering the short propagation time of the BNS5km simulations.

Further research could include more reflective periods and non-hydrostatic effects as the smaller-scale simulations have a larger vertical scale.

Chapter 4

Lee Waves in a Surface-Intensified Current

4.1 Introduction

The goal of this chapter is to analyze the impacts of surface-intensified currents (SICs) on lee wave propagation and energy dissipation using the non-hydrostatic form of the MITgcm numerical model (*Marshall et al.*, 1997). Numerical results from eight 2D simulations with sinusoidal topographies, linear surface-intensified current and constant stratification will be compared to theoretical predictions and two depth-uniform current simulations, similar to Chapter 3. The name of each simulation follows the nomenclature defined in Chapter 3.

4.1.1 Expectations

Chapter 2 presents linear wave theory in detail. Some aspects of linear theory and prior work that will be validated in this chapter are:

1. For smaller values of k, bottom horizontal wave velocity u'_b and v'_b are faster and vertical wave velocity w'_b are slower compared to predictions for larger values of k, based on the polarisation relation presented in Chapter 2. In mathematical terms, for $k_1 < k_2$: $u'_{b,k1} > u'_{b,k2}$, $v'_{b,k1} > v'_{b,k2}$ and $w'_{b,k1} < w'_{b,k2}$;

2. Wave reflection at an internal reflective layer where the Lagrangian wave frequency, Ω, matches the local buoyancy frequency, N, or at the surface, based on ray tracing (Chapter 2.1.1);

3. The generation of vertical modes and interference patterns as upward propagating waves encounter downward propagating waves (Chapter 2.4);

4. The generation of inertial oscillations triggered by the interactions of wave energy dissipation and the mean background flow (*Nikurashin and Ferrari*, 2010a)

5. The generation of surface displacements by waves freely propagating through the water column (*de Marez et al.*, 2020).

4.2 Methods

4.2.1 Numerical Simulations

Eight simulations are run with a linear surface-intensified current using the non-hydrostatic mode of MITgcm model since the lee wave vertical wave number decreases exponentially as the wave propagates upwards, making it non-hydrostatic. Two comparative depth-uniform simulations with lengthscales of 5 km and 72 km are ran, similarly to Chapter 3. Figure 4.1 illustrates the different bathymetry, background and stratification profiles used in this chapter. The numerical set up is identical to Chapter 3 and presented in details in Appendix B.

In the case of SICs, the propagation depth, h_p, corresponds to an internal reflective layer (IRL) if the wave frequency is Doppler-shifted to the buoyancy frequency within the water column. If the wave reaches the surface, the propagation depth is the total depth of the domain. A *reflection cycle* is defined as the trajectory of a wave packet from the bathymetry to the surface or an IRL and back to the ocean floor. The time it takes to do so will be referred to as *reflective time*, $t_r = 2t_p$. Finally, the analysis time, t_a, is set to five reflection cycles for the simulations to be dynamically comparable. Table 4.1 presents the simulation parameters. Simulations SIC1.4km to SIC5km are referred to as the *internally reflecting simulations* because of the presence of an IRL, and the last five, SIC7km to SIC72km, are referred to as the *surface reflecting simulations* because the wave propagates freely to the surface. The energy calculations are identical to Chapter 3, except that the equations adjusted for non-hydrostatic physics.

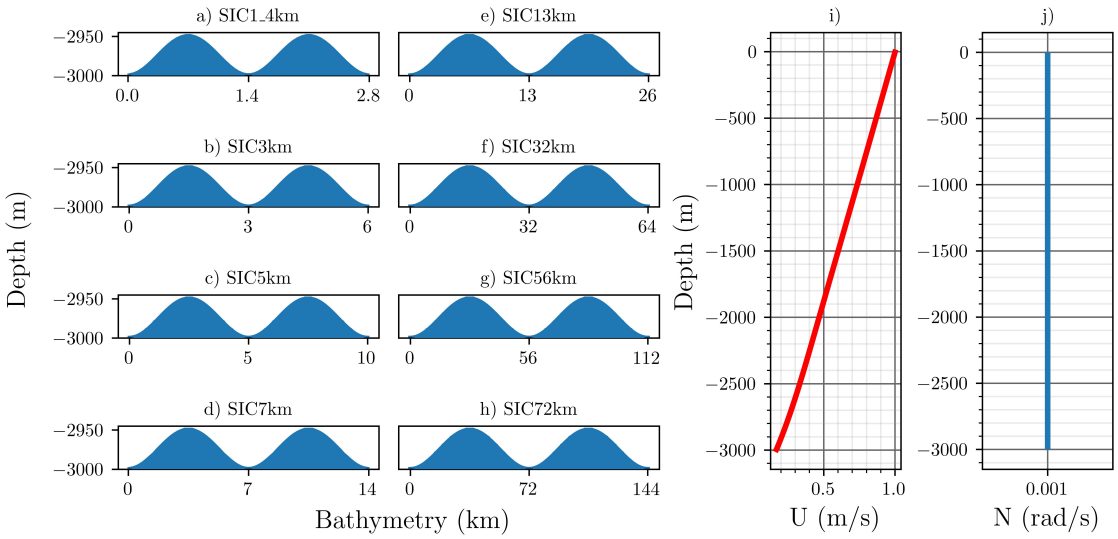

Figure 4.1: a) to h) Bathymetric profiles SIC1.4km to SIC75km, i) Background current profile and j) Stratification profile.

The SIC simulations do not use a ramping-up scheme because the smaller-scale simulation's reflective time is only a few hours, and ramping up the model over such time scales would be similar to a sudden start. A test was done for the larger scale simulations, and the energy dynamics were similar with and without a ramping up, giving us confidence in the model outputs. Finally, model outputs are printed every five minutes for simulations SIC1.4km to SIC13km since the propagation time is shorter for these simulations, and time variability would be missed otherwise. For simulations SIC32km to SIC72km, outputs are printed every hour since the propagation times are longer.

Table 4.1: Parameter of the sinusoidal simulations with a surface-intensified current. The Coriolis parameter is $f = 10^{-5}$ s^{-1} and buoyancy frequency $N = 10^{-3}$ s^{-1}. The analysis time for simulations SIC1.4km to SIC13km is smaller than the inertial period $t_f = 174$ h (10440 min).

	Length scale L km	Horizontal wavenumber k m^{-1}	Generation frequency Ω_b s^{-1}	Propagation depth h_p m	Propagation time t_p min	Analysis time t_a min
SIC1.4km	1.4	44.88×10^{-4}	8.98×10^{-4}	2910	75	745
SIC3km	3	20.94×10^{-4}	4.18×10^{-4}	1950	175	1765
SIC5km	5	12.57×10^{-4}	2.51×10^{-4}	760	250	2505
SIC7km	7	8.98×10^{-4}	1.79×10^{-4}	0	310	3060
SIC13km	13	5.03×10^{-4}	0.97×10^{-4}	0	525	5295
SIC32km	32	1.96×10^{-4}	0.38×10^{-4}	0	1310	13080
SIC56km	56	1.16×10^{-4}	0.23×10^{-4}	0	2510	2580
SIC72km	72	0.87×10^{-4}	0.17×10^{-4}	0	3570	35700

4.2.2 Time Averaging

The analysis time for this set of simulations was arbitrarily set to five reflective cycles. This time is used to qualitatively compare snapshots of the simulations. To make quantitative statements, a time average from the starting point of the simulation until the analysis time is used for simulations SIC1.4km to SIC13km and over the last inertial oscillation for simulations SIC32km to SIC72km.

4.3 Results

4.3.1 Wave Velocity Predictions

Theoretical lee wave bottom-velocity predictions are made using equations 2.18 to 2.20. To validate the model outputs and verify expectation 1, simulated values are time-averaged and normalized by the predicted velocities (figure 4.2). For the first series, results are averaged over the propagation time, t_p. For the second series, the time average is taken until the analysis time, t_a. Numerical velocities are averaged 50 m above bathymetry, to limit boundary effects. Simulated velocities calculated over the propagation time generally follow the predicted velocity patterns (expectation 1) with faster vertical velocities and slower horizontal velocities for waves generated over a larger topographic scale. Numerical velocity magnitudes normalized by the theoretical predictions are one to two and a half times larger than the linear

predictions (figure 4.2). After five reflection cycles, differences between numerical values and predictions are more significant, with one to eighteen times larger values. The discrepancies result from a modification of the wave generation due to reflection in the domain and interaction of upwards and downward propagating waves. They are the largest for SIC3km.

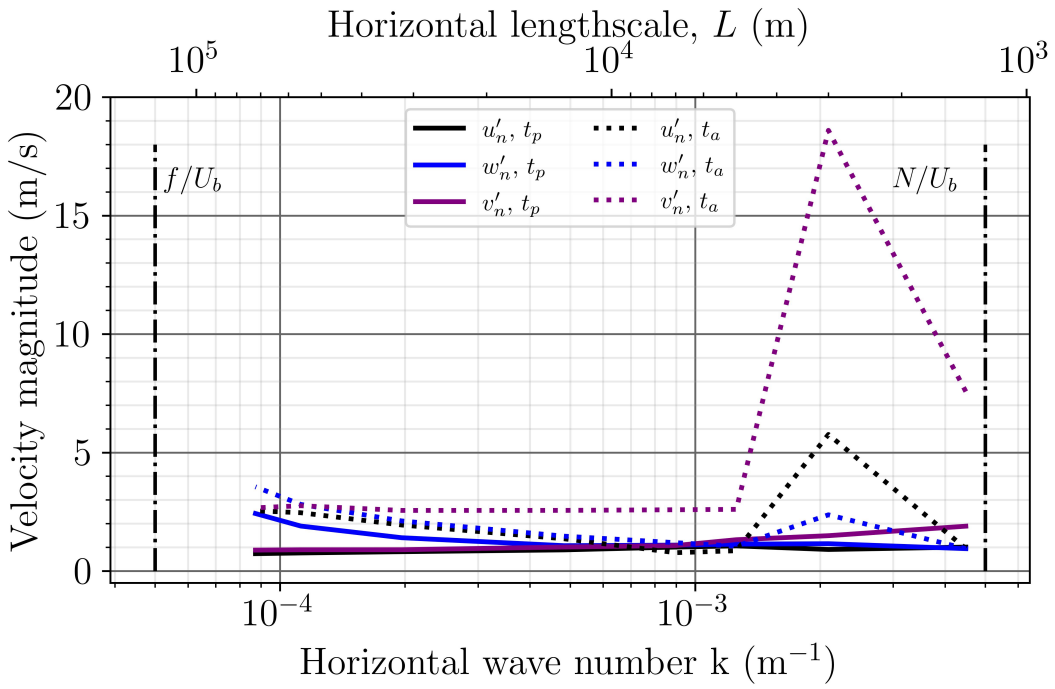

Figure 4.2: Simulated velocity normalized by analytical velocity, (u'_n, v'_n, w'_n), for the different SIC simulations. The left-most point is associated with SIC72km, and the right-most point is with SIC1.4km. The series associated with the solid line is averaged until the propagation time t_p, whereas those associated with the dotted line are averaged until the analysis time t_a. Limits of the radiating wavenumbers are marked with the dotted-dashed lines. The Coriolis parameter and buoyancy frequency are normalized by the bottom current velocity, $U_b = 0.2$ m/s.

4.3.2 Wave Field

Ray tracing predicts a reflection layer for simulations SIC1.4km to SIC5km at a depth of $z = -2910$ m, $z = -1950$ m and $z = -760$ m, respectively (black dotted line, figure 4.3). The internal reflective layer for the internally reflective simulations, SIC1.4km to SIC5km, can be seen as wave velocity magnitudes decrease with height, verifying expectation 2. Signs of resonance can be seen in simulation SIC3km, where isopycnals displacements are very large and wave velocities are enhanced near

bathymetry. The $\rho_0 = 1036.14$ kg/m^3 isopycnal displacement grows and moves upstream over time (see figure 4.4). The displacement is reminiscent of a rotor with the reverse flow (blue area) near the bathymetry on figure 4.4. Numerical studies from *Doyle and Durran* (2002) and *Grubišić and Stiperski* (2009) showed the formation of atmospheric rotors in free-slip numerical simulations, similar to what is seen in simulation SIC3km.

Simulations SIC7km and SIC32km to SIC72km present vertical modes illustrated by the checker-board pattern in figure 4.3, consistent with expectation 3. The distance between the zero crossing of the vertical mode profiles stretches with height, which is an impact of the positively sheared background current. As a lee wave propagates upwards in a SIC, its vertical wave number m reduces with height, meaning that the vertical scale of the wave increases, thus elongating the vertical modes. All surface reflecting simulations except for SIC13km present an anti-node around $z \approx -2600$ m and $z \approx -1200$ m. Simulation SIC13km shows slightly enhanced velocities in the bottom 400 m of the domain. Still, the other node from the vertical mode is absent, which we take as a sign of destructive interference between downward reflected and upward propagating waves. Kinetic energy fields are similar to the velocity fields, with zones of enhanced energy corresponding to zones of enlarged wave velocities (figure 4.5). As predicted, little energy is seen above the IRL for the simulations SIC1.4km to SIC5km. Small-scale density anomalies in the density contours are seen near bathymetry for these simulations, which is most likely a precursor for the grid noise near bathymetry in g) and h). In the ocean, these instabilities' growth lead to wave breaking and turbulence near bathymetry. However, these simulations do not resolve turbulence and tend to form grid scale noise when energy is not dissipated sufficiently fast by the numerical and explicit viscosity.

4.3.3 Energetics

The internally reflective simulations, SIC1.4km to SIC5km, are highly non-hydrostatic, and their residue is larger than our closure criteria of 10%. Therefore, a limited analysis is presented hereafter. Amongst the hypotheses explaining the high residue are that MITgcm is inaccurately resolving the non-hydrostatic pressure term and

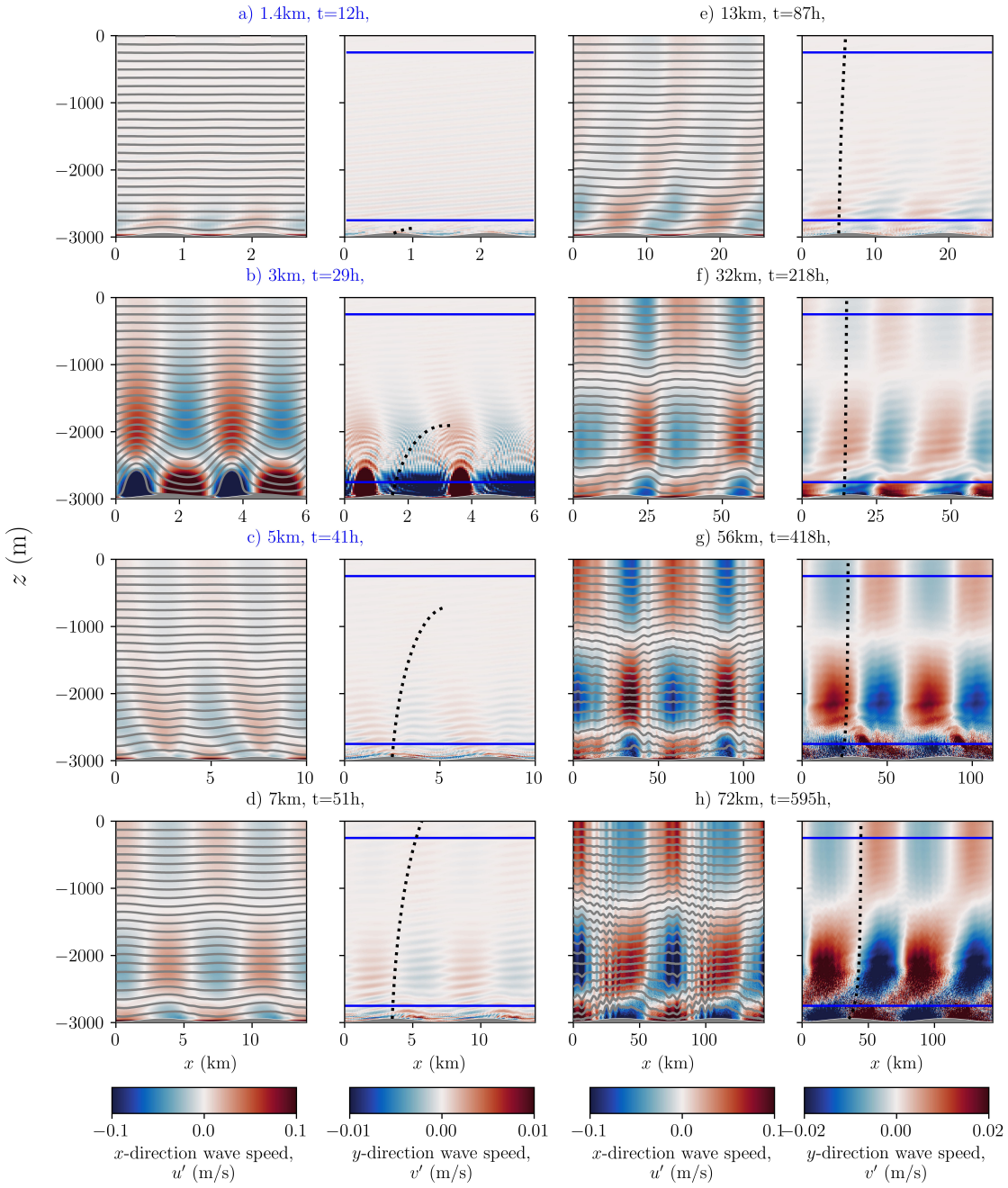

Figure 4.3: Horizontal velocity perturbation, u' (m/s) (left) and v' (m/s) (right) after five reflection cycles. The blue box vertically delimits the integration domain used for the energy budget. Reflective layers are expected for three simulations: SIC1.4km, SIC3km and SIC5km at a depth of -2910 m, -1950 m and -760 m, respectively. The energy path, calculated in an Eulerian frame of reference, is illustrated in the v' panels (black dotted line). Reflective simulations are identifiable by the blue subtitle.

that the analysis code used to calculate the energy terms is using a numerical scheme with a lower precision than those used by MITgcm.

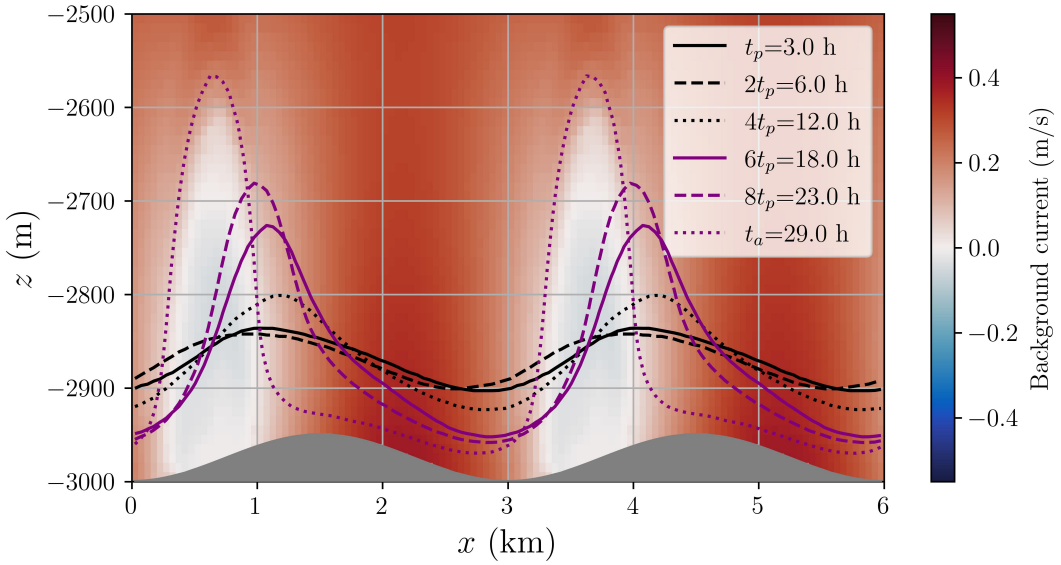

Figure 4.4: Background current at t_a. The $\rho_0 = 1035.14$ kg/m^3 isopycnal is plotted at the propagation time and each reflective cycle until the analysis time (black and purple lines).

There is an overall agreement between reflection period and time oscillations for simulations SIC1.4km, SIC3km and SIC7km (figure 4.6, the vertical grey lines). The dominant energy terms are the potential to kinetic energy transfer (purple), the shear production term (green) and the time derivative of the kinetic energy (blue). In contrast to the BIC simulations, the dissipation of kinetic energy is small compared to the dominant terms, and the advection of kinetic energy is stands out for simulations SIC3km, SIC13km and SIC72km. For clarity, figure 4.6 does not show the non-dominant terms, except for the energy dissipation.

A spectral analysis was undertaken to investigate the simulation time dependency by calculating the spectra of the de-meaned background shear production at each grid point and averaging them together over the domain. The total number of spectra averaged together ranges from 14,000 for simulation SIC1.4km to 180,000 for simulation SIC72km, depending on the simulation resolution. Results for simulation SIC7km are presented in figure 4.7 as an example. Appendix C presents the other spectra. The periods associated with spectral peaks are shown in table 4.2, where peaks are ordered from the highest frequency (peak no1) to the lowest (peak no3). The frequencies were extracted by a visual analysis of the power spectra.

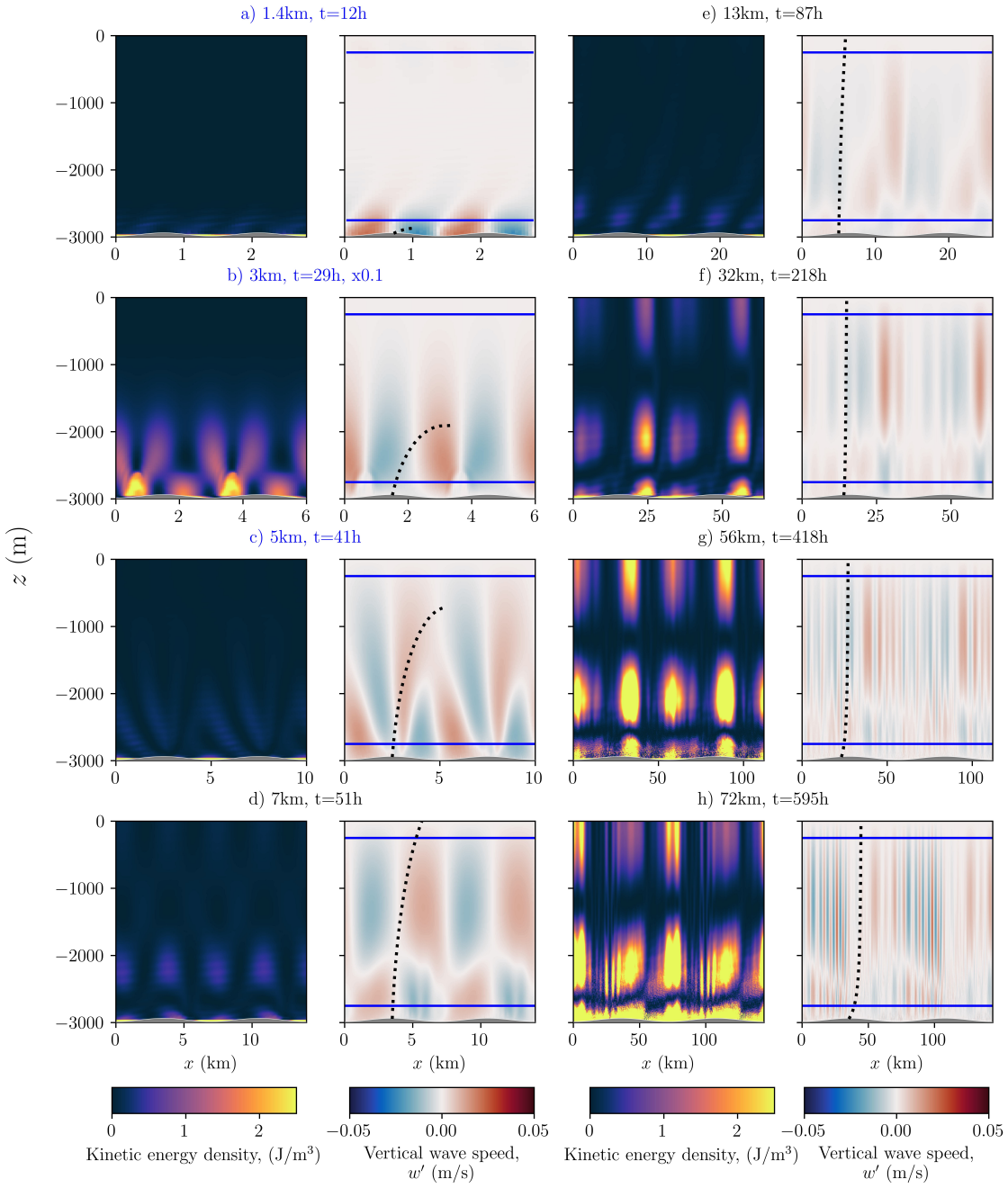

Figure 4.5: As for figure 4.3 but for the wave kinetic energy density (J/m^3) (left) and vertical wave speed w' (m/s) (right). Vertical modes have formed from interference between upward and downward propagating waves.

Simulations SIC3km and SIC7km present a peak associated with the reflection time, t_r. As for simulation SIC1.4km, the period associated with the frequency dominating the power spectra is between the reflection and Lagrangian wave frequency. Surprisingly, simulations SIC5km and SIC13km present a peak close to the wave

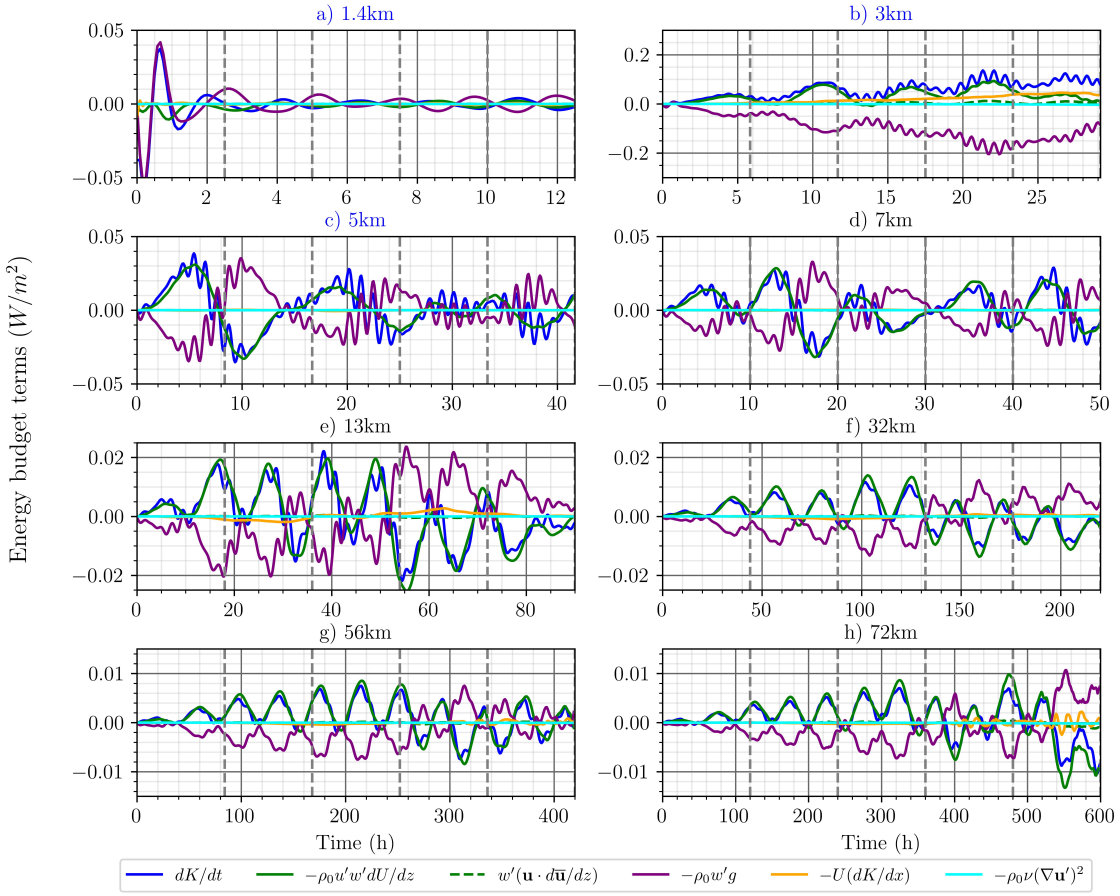

Figure 4.6: Kinetic energy budget normalized by the width of the integration domain. The dominant terms in these budgets are the time derivative of kinetic energy (blue), the available potential energy to kinetic energy transfer (purple), and the shear production (green). The vertical dashed lines represent reflection cycles.

generation period, and SIC32km to SIC72km show a peak close to the first harmonic of the Lagrangian wave frequency. Question remains about the origin of these frequencies as they do not arise directly from the wave motion since Lee waves are stationary in an Eulerian frame of reference, i.e. their frequency $\omega = 0$.

The spectral analysis showed that the time variability is unique to each simulation. The horizontal distance travelled by the wave energy over a reflection cycle was calculated using ray tracing to identify possible interference effects near bathymetry. The wave energy travelled approximately 0.51, 1.07, 1.17, 0.65, 0.15, 0.06, 0.14 and 0.26 times the horizontal length scale for SIC1.4km to SIC72km in one reflection cycle. Simulations SIC7km and SIC32km to SIC72km showed similar wave fields and

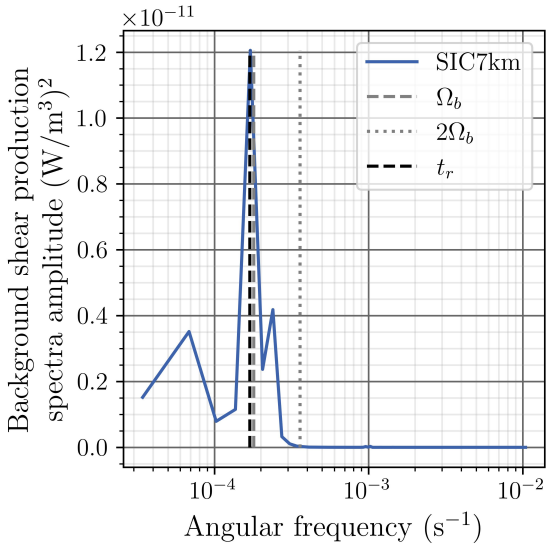

Figure 4.7: Background shear production spectra for SIC7km. The vertical grey dashed line represents the wave generation frequency Ω_b, the grey dotted line marks the first harmonic of the wave 2Ω, and the black, vertical, dashed line is the reflection time.

Table 4.2: Background shear production oscillation periods. All periods are in hours.

	Peak no1	Peak no2	Peak no3	Lagrangian wave generation period $T_{L(z=h)}$	First harmonic period $2T_{L(z=h)}$	Reflective time t_r	Analysis time t_a
SIC1.4km	2.1	-	-	1.9	1.0	2.5	12
SIC3km	5.8	-	-	4.2	2.1	5.8	29
SIC5km	6.9	13.9	-	6.9	3.5	8	41
SIC7km	7.2	10.2	25.5	9.7	4.8	10	50
SIC13km	10.8	29.0	-	18.9	9.4	17	80
SIC32km	21.8	72.7	-	43.2	22.4	43	218
SIC56km	38.0	139.3	-	77.6	38.8	83	418
SIC72km	49.6	198.3	-	99.7	49.7	119	595

vertical modes. However, the distance travelled by the reflected wave differs for each simulation. There is no obvious link between the horizontal distance predicted by ray tracing, reflection patterns and time variability. Finally, in contrast to the BIC simulations, IO remains small even for simulations run long enough to resolve them.

Small-scale simulations are expected to be more energetic than larger-scale simulations, based on energy flux predictions from Chapter 2. Simulation SIC1.4km

presents less energy than most other simulations, contradicting this prediction. However, the reflective layer is below the energy budget's bottom boundary. Therefore, little wave energy enters the integration domain. The magnitude of the energy terms for simulation SIC3km is one order of magnitude larger than for the other simulation, highlighting the importance of constructive interference within the domain. For simulations SIC5km to SIC72km, the magnitude of the energy terms generally decreases as the bathymetric length increases, as expected by theory.

4.3.3.1 Background Shear Production

The integrated background shear production is not strictly positive for simulations SIC1.4km to SIC72km. For waves propagating through an infinitely deep water column with surface-intensified currents, theory predicts an energy gain from the background current. When wave reflection is considered, the shear production term becomes a combination of upward and downward waves and the wave velocity can be expressed as $\mathbf{u}' = \mathbf{u}'_{up} + \mathbf{u}'_{down}$, which introduces cross terms that influence the shear production sign. Thus, energy gain or loss does not only depend on whether the wave is upward or downward propagating. Consistent with figure 4.6, figure 4.8 shows that the background shear production oscillates between energy gain from the background flow, i.e. positive values, and energy loss to the background current, i.e. negative values, for all simulations with values generally decreasing towards the surface. There is an energy gain at the beginning of all simulations (positive shear production), after which the shear production oscillates in time and shows positive interference (dark red zones) and negative interference (blue zones). The spectral analysis revealed a time signature associated with the reflective time for simulation SIC3km and SIC7km consistent with theoretical expectations, whereas the other simulations present different periods.

4.3.3.2 Residual Horizontally-averaged Current

The vertical variability of the residual horizontally-averaged x-direction current, $\overline{u}$, profiles show that jets are being generated, similarly to Chapter 3 (figure 4.9). These jets act to accelerate and decelerate the background current.

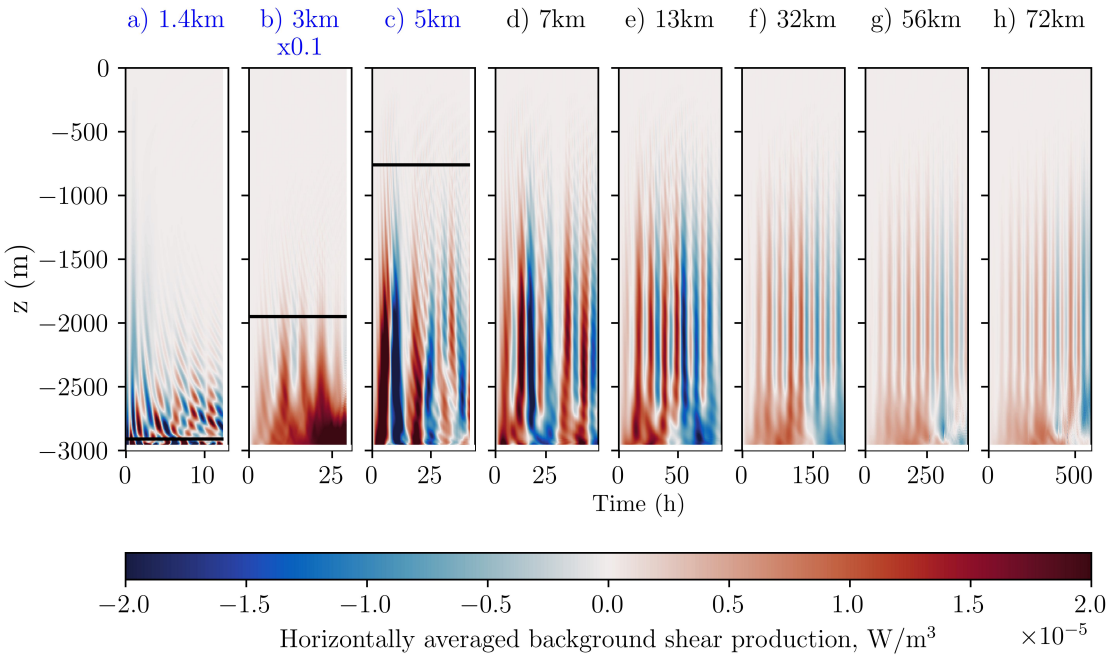

Figure 4.8: Horizontally average shear production profiles. The horizontal average is taken over the width of the budget. Red means energy gain and blue energy loss. There are cycles of energy loss and energy gain. Horizontal black lines indicate IRL.

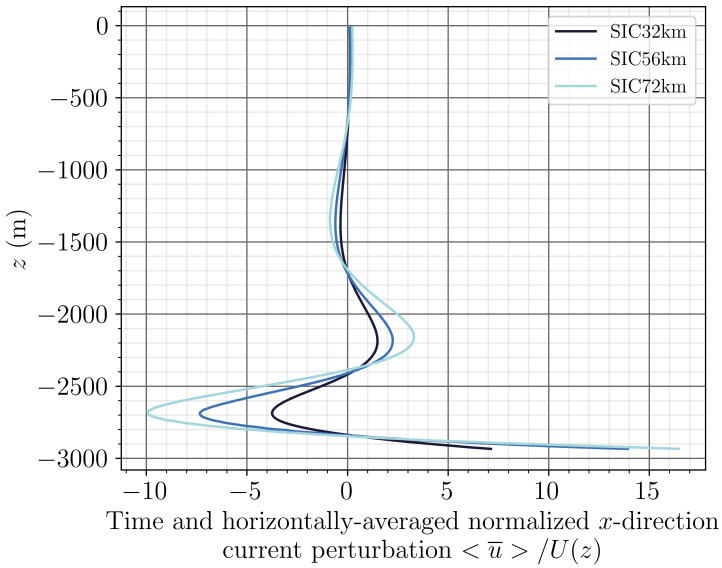

Figure 4.9: Time and horizontally-averaged residual current normalized by the prescribed background current. Profiles are time averaged over the last inertial period.

Inertial oscillations are expected in all simulations based on results from *Nikurashin and Ferrari* (2010a). The spectral analysis did not reveal the presence of inertial oscillations in simulations SIC32km to SIC72km, contrary to what was seen for the

BIC simulations in Chapter 3. Figure 4.10 presents a time series of the residual horizontally-averaged x-direction current, $\overline{u}$ for all simulations. For simulations SIC32km to SIC72km, inertial oscillations are identifiable by the time variability between $z = -2500$ m and $z = -1500$ m, where the magnitude of the inertial current is accelerated and decelerated on the time scale of the inertial oscillations, consistent with expectation 4.

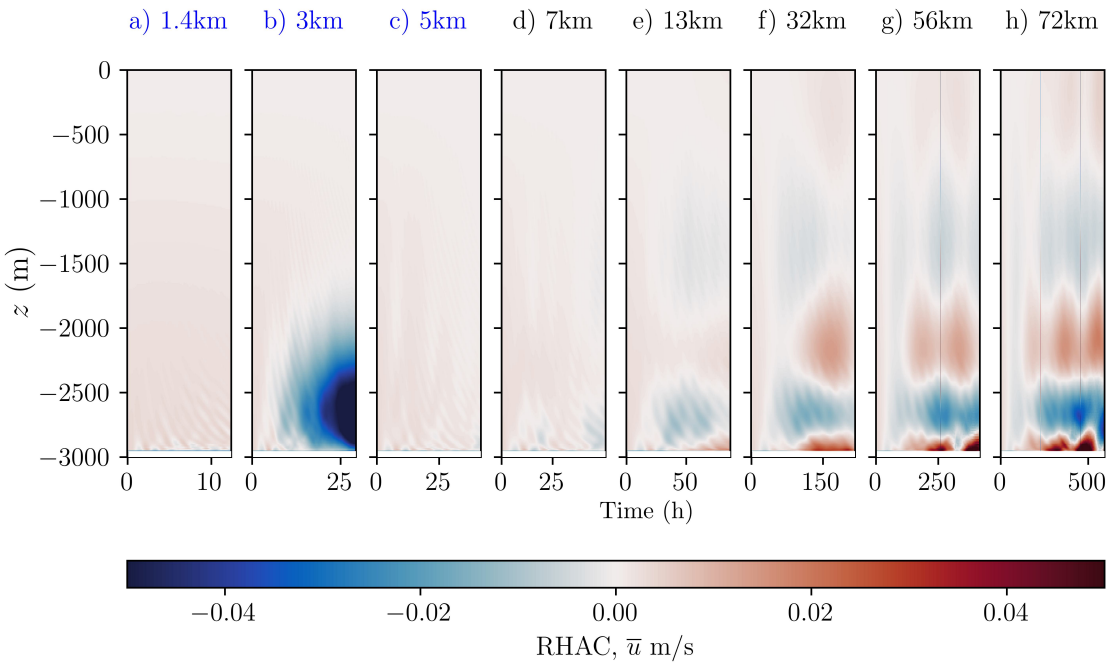

Figure 4.10: Time series of the x-direction RHAC, $\overline{u}$. Red means that the velocity is faster than the background current, and blue that the velocity is slower.

Considering the magnitude of the residual horizontally-averaged current compared to the background current and the absence of a time signature in the energy budget, IO are not a dominant physical phenomenon for surface-intensified simulations, contrary to results from Chapter 3. Wave reflection and the jets generated are the prevalent physical phenomena affecting the background current.

4.3.3.3 Energy Dissipation

Kinetic energy dissipation profiles are presented Figure 4.11. Each profile is horizontally averaged over the width of the domain and time-averaged over the analysis time. Simulation SIC3km shows the most energy dissipation, as expected, considering the

resonance of this simulation. Vertical oscillations of the dissipation profiles do not match the vertical modes observed in the wave field, and energy dissipation decreases with height (figure 4.11 compared to figure 4.3). Enhanced dissipation is seen near bathymetry and in the bottom 1000 m of the domain, which fits with areas of enhanced kinetic energy and expectation 5. Without reflection, i.e. when numerical results are averaged over t_p, a minimum of $\approx 82\%$ of the dissipation happens in the bottom 1000 m of the domain (figure 4.12). After five reflection cycles, dissipation is better distributed across the water column, but it remains largest below $z = -2000$ m, except for simulation SIC1.4km. However, the reflective layer for this simulation is situated near the bathymetry and energy propagation from the model start up could affect the vertical distribution. As for the dissipative fraction, all simulations except for SIC1.4km present higher percentages of energy dissipation at the analysis time, with interactions of upward and downward propagating waves enhancing energy dissipation.

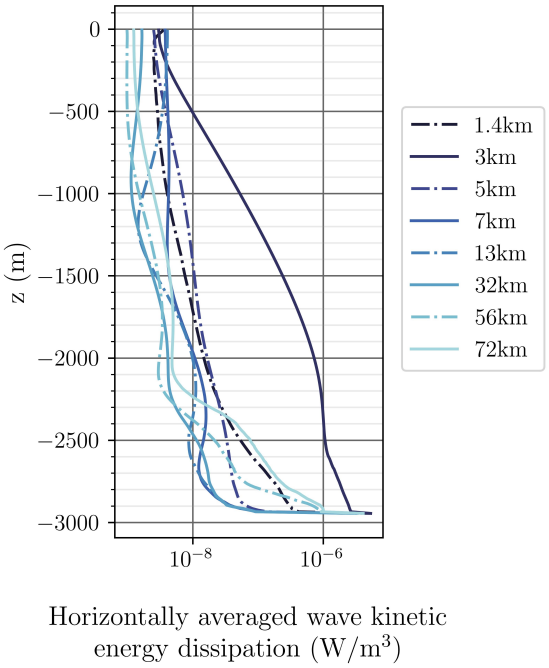

Figure 4.11: Energy dissipation profiles for the SIC simulations run with MITgcm. The horizontal average is taken over the width of the domain and the time average over the analysis time.

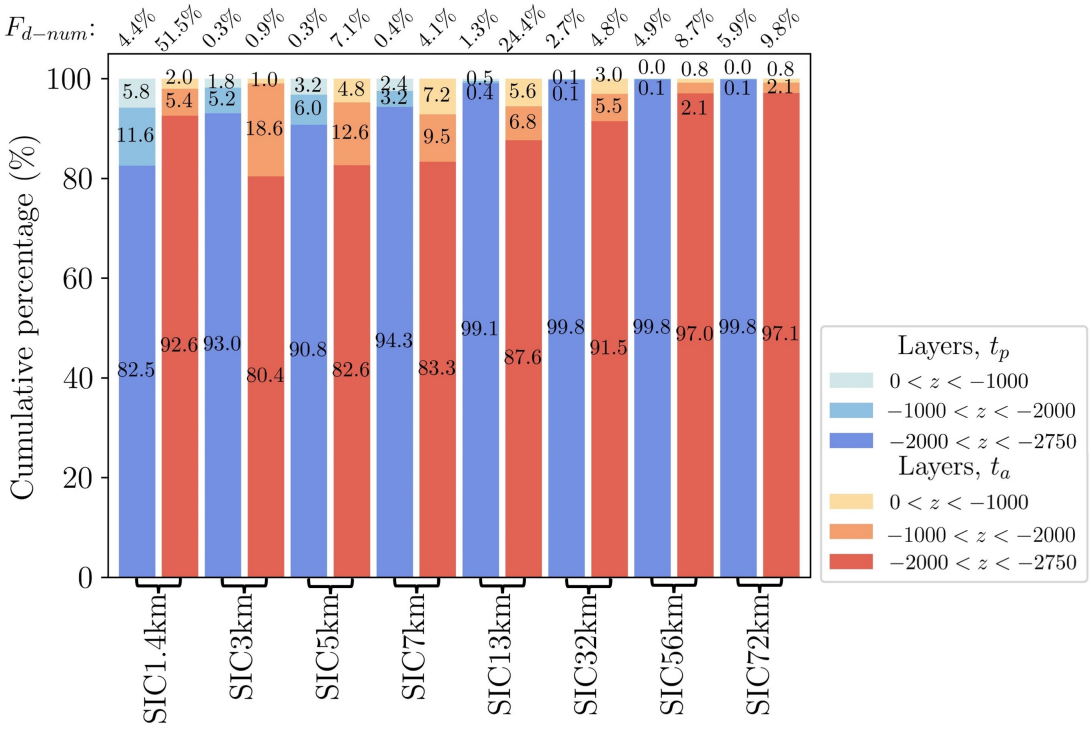

Figure 4.12: Vertical distribution of the energy dissipation. Dissipation is integrated in bins of 1000 m and normalised by the total energy dissipation in the domain. Data is time averaged over the propagation time t_p (blue shades), and the analysis time, t_a (red shades). The dissipative fraction is indicated above each bar.

4.3.4 Comparison with Depth-Uniform Currents

Two additional simulations were run with a depth-uniform current equal to $U_b = 0.2$ m/s to compare the kinetic energy profiles and energy dissipation distribution with SIC simulations. Like Chapter 3, the chosen comparative lengthscales are 5 km and 72 km for the non-sheared simulations, respectively named SNS5km and SNS72km, where the first S stands for "surface", NS for "non-sheared" followed by the lengthscale. Data is averaged over the SIC simulations' analysis time. The 5 km lengthscales are averaged over 42 h and over 595 h for the 72 km lengthscales. In contrast with BICs, the group velocity of waves propagating through the SICs accelerates with height. With a propagation time of 17 h, approximately 1.24 reflection cycles have been completed for the SNS5km simulation compared to 5 for the SIC5km simulation. For the SNS72km, approximately 0.7 of a reflection cycle has been completed ($t_p = 433$ h). The distance between the crests of the vertical mode is constant for the SNS5km, in contrast with the SIC72km simulation, which presents a

profile that stretches with height (figure 4.13a). Vertical modes are not fully formed for the BNS72km since the wave energy has not completed an entire reflection cycle at the analysis time. The reduction in kinetic energy with height and the absence of vertical modes for SIC5km indicate destructive interference between upward and downward propagating waves. Energy dissipation is enhanced near bathymetry for all simulations, but the SIC simulations present significantly higher fractions in the bottom layer (figure 4.13b) compared to the non-sheared simulations. Dissipative fractions are larger for the surface-intensified simulations than the depth-uniform ones.

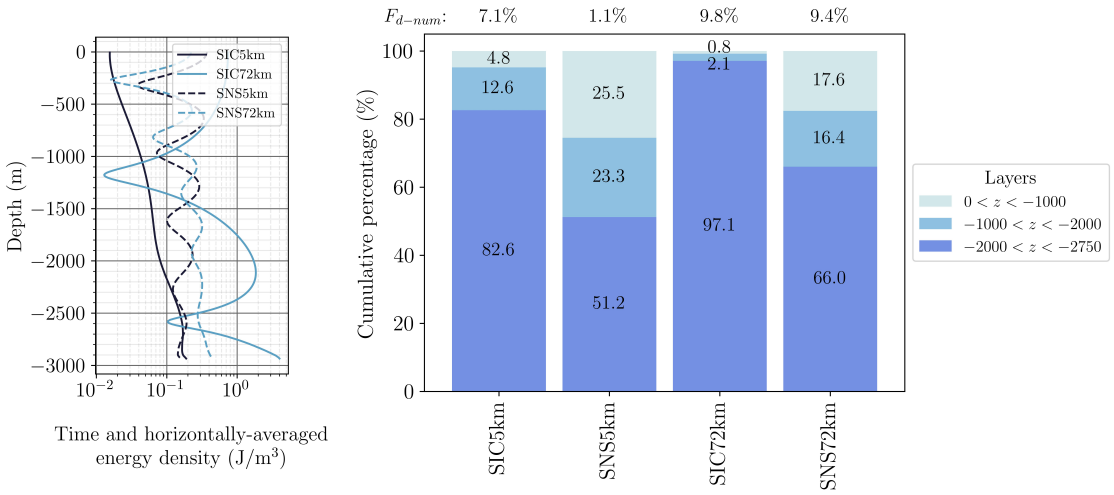

(a) (b)

Figure 4.13: a) Kinetic energy density profiles of the SIC and non-sheared 5km and 72km simulations. The horizontal average is taken over the width of the domain and time-averaged over the analysis time. b) Vertical distribution of the energy dissipation integrated in bins of 1000 m. Data for both panels is averaged over one reflective cycle.

4.3.5 Sea Surface Anomalies

Lee waves propagating to the surface are expected to leave a trace with a horizontal length scale similar to the bathymetric scale. In contrast, internally reflecting waves are expected to be blocked at the IRL and leave no surface signature. Figure 4.14 shows no surface trace for simulation SIC1.4km and a trace for all the other simulations, which partially fits with theoretical predictions.

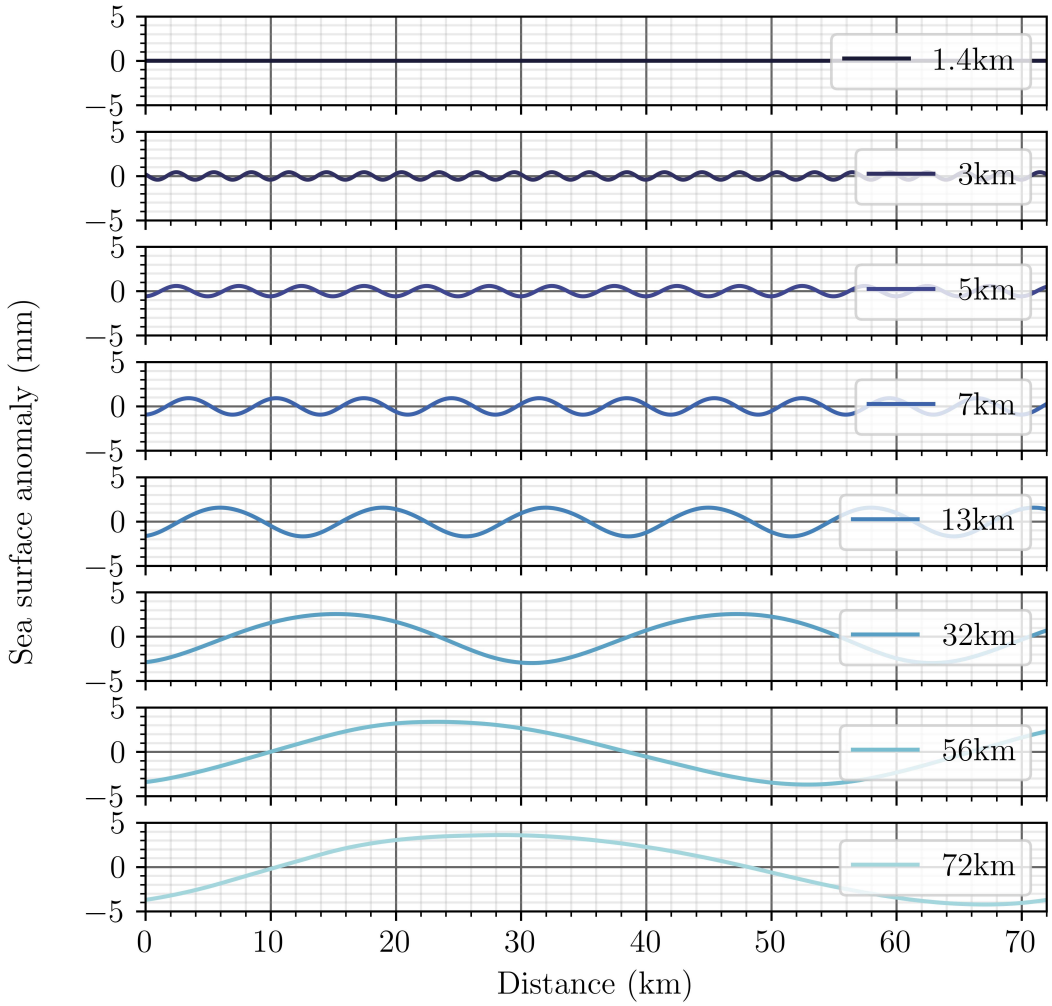

Figure 4.14: Sea surface anomaly for all SIC simulations. Profiles are averaged over time until the analysis time. The surface trace is uniform in depth and similar to the bathymetric length scale for simulations SIC5km to SIC72km.

4.4 Discussion

This section analyzes and compares simulation results from ten idealized lee wave simulations to assess the impacts of surface-intensified current on energetics and energy dissipation.

First, the model outputs are compared to theoretical predictions of bottom velocities. Simulated velocities vary from one to three times the predicted velocity before wave reflection and vary from 1 to 18 times when averaged over five reflection cycles (figure 4.2). Normalized velocity profiles show an acceleration near bathymetry,

mostly due to vertical modes and the generation of jets within the water column, explaining the discrepancies between theoretical and simulated results at the analysis time. The wave field becomes evanescent slightly above the reflective layers for simulations SIC1.4km to SIC5km, which indicates that the wave is partially reflected downwards (figure 4.3). For the surface propagating simulations, all wave fields except for SIC13km show checker-board patterns associated with vertical modes caused by wave reflection. Wave kinetic energy is enhanced at the crest of the vertical modes and generally decreases with height (figure 4.5).

As for the wave energetics, all the simulations are strongly time-varying (figure 4.6). Spectral analysis of the shear production term did not reveal a correlation between predicted time variability and known periods, such as the reflective and wave harmonic periods (table 4.2). The horizontal distance travelled by the energy has been calculated to find an explanation for the large-time oscillation associated with five reflection cycles. However, after five reflection cycles, the wave energy does not align with the crest of the bathymetry, where waves are generated, except for simulation SIC3km, which shows resonance and isopycnal displacement reminescent of a rotor (figure 4.4). Questions remain about the interaction of upward and downward propagating waves and what drives the sign change of the energy terms. Inertial oscillations are weaker in the SIC simulation than in the BIC ones (figure 4.10). Wave reflection and interference dominate the wave field, and jets are generated in the water column (figure 4.9).

The dominant terms in the energy budget are similar to those in Chapter 3 for the BIC simulations. The advection of kinetic energy by the background flow stands out in SIC3km and SIC13km. In contrast to the BIC simulations, the energy dissipation term remains much smaller than the dominant terms. With time, the background shear production and divergence of the energy flux changes sign, meaning that the wave gains and loses energy to the background current and that the total energy in the wave field increases and decreases. This is a result of wave reflection and wave interactions.

Energy dissipation is enhanced near bathymetry for all simulations, with more than 80% of the dissipation happening in the bottom 1000 m of the domain (figure 4.12).

After five reflection cycles, energy dissipation is distributed more evenly compared to fractions calculated over the propagation time. However, dissipation near bathymetry still dominates. Non-sheared simulations show a similar dissipation distribution with enhanced values near bathymetry but with a lower fraction at shallower depths compared to the SIC simulations (figure 4.13). As for the energy profiles, SIC5km presents less energy than SNS5km, likely caused by destructive interference. One reflection cycle has been completed for the SNS5km simulation. SNS5km simulations present a uniform vertical profile, which contrast to the SIC72km simulations, where the vertical mode is stretched with height. This illustrated the changes in the vertical wave number expected for wave propagation trhough SIC. Vertical modes are better defined in top half of the water column for SNS72km, which fits with the distance travelled by the wave energy after 0.7 reflection cycle. Dissipative fractions are largest for the SIC simulations after five reflection cycles compared to fractions averaged over the propagation time, and compared the non-sheared dissipative fractions.

The surface-intensified simulations present similar challenges and caveats as the BIC simulation since they share the same numerical setup. However, the dynamic similarity is easier to obtain across simulations since the reflection time is shorter than the time for the energy to reach dissipative layers. As for the non-hydrostatic mode, we suspect that MITgcm is not precisely solving the pressure components, affecting calculations. To ameliorate the accuracy of the model, it would be possible to increase the spatial resolution or the number of iterations allowed for the model to converge. However, time constraint limited the extent of numerical testing necessary to fix this issue. Finally, some questions about time variability and interference such as "what are the mechanism underlying wave reflection that are generating wave harmonics?" remain unanswered.

Chapter 5

Conclusion

With recent studies highlighting the impacts of lee wave parametrization on global models and theoretical predictions and in situ dissipation measurement not agreeing (*Melet et al.*, 2014; *Cusack et al.*, 2017; *Waterman et al.*, 2013), different hypotheses explaining these discrepancies are under active research. Among these hypotheses is the impact of depth-varying currents. *Kunze and Lien* (2019) theoretically explore the effect of bottom intensified current on lee wave energetics. They showed that the wave loses energy to a bottom-intensified background current, reducing the fraction available for turbulence. *Baker and Mashayek* (2021) studies the effect of surface intensified currents and surface reflection. They show that surface reflection can modified wave generation and interactions of upward and downward propagating wave can generate zones of enhanced dissipation. The thesis aimed to test *Kunze and Lien* (2019)'s theory and extend it to positively sheared currents using numerical modelling to answer the following research question: **What are the impacts of depth varying currents on lee wave energetics and the energy available for turbulence?**

Two groups of simulations were designed to answer the research question and further investigate the impacts of depth-varying currents. Chapter 3 analyzes the effects of bottom-intensified currents using results from eight idealized numerical simulations paired with a linear current and a sinusoidal bathymetry. A comparison between depth-uniform and bottom-intensified simulations is also presented. Similarly, Chapter 4 explored the case of surface-intensified currents using the same numerical setup as Chapter 3 but coupled with a surface-intensified current.

First, shear production ($-\rho_0 u'w' \frac{dU}{dz}$) calculations showed how energy was exchanged as the waves propagated through bottom intensified (surface intensified) currents. Chapter 4 showed that when surface or internal reflection occurs, it generates vertical modes, and energy exchanges no longer depend uniquely on the sign of the background shear because of vertical and lateral wave interactions. Results from BIC simulations showed that the energy lost to the background flow acts to accelerate it. Furthermore, the vertical structure generated by wave reflection causes jets in the background current. Another impact of depth varying currents is the appearance of critical layers: dissipative layers for BIC and internal reflective layers for SIC. Results from Chapter 3 showed dissipative layers where the wave frequency becomes near-inertial as predicted by ray tracing and linear theory. Results from the bottom-intensified simulations show that these dissipative layers have a leading order impact on the vertical distribution of energy dissipation. For the internal reflective layers, results from Chapter 4 show evanescent fields where the wave frequency is larger than the Buoyancy frequency.

In rotating flows, breaking waves deposit their momentum into the background flow, which in turn acts to decelerate it and triggers near-inertial oscillations (*Nikurashin and Ferrari*, 2010a). Near inertial oscillations interact with lee waves in different ways. First, they accelerate and decelerate the background current, which changes the generation frequency of the waves, making the field multi-chromatic. Chapter 3 shows that waves generated with a slightly slower background current will have a smaller generation frequency and propagate further into the water column before encountering a dissipative layer. Conversely, waves generated with a faster current will dissipate lower into the water column. Near inertial oscillations are particularly strong in areas of energy dissipation situated below dissipative layers. Results from the SIC simulations of Chapter 4 show that in contrast with BIC simulations, IO grows less rapidly and are less critical than wave reflection in SIC.

As for the energy available for turbulence, *Kunze and Lien* (2019) calculated dissipative fractions using wave action. They assumed an inviscid and infinitely deep ocean and restricted dissipation to the dissipative layer. In other words, the energy flux is either exchanged with the background flow or dissipated, and waves propagating further into the water column lose more energy, reducing the dissipative

fraction. The work presented in Chapter 3 shows that the dissipative fraction is more significant for simulations where a dissipative layer is reached lower into the domain, in agreement with these predictions. However, the energy exchanged and dissipated does not add to the energy flux and shows that other physical phenomena, such as energy exchange with IO or kinetic to potential energy transfer, are at play. Inertial oscillations can have a larger impact than dissipative layers on the vertical distribution of the energy dissipation (figure 3.12). Therefore, the dissipative fraction does not only include dissipation arising from the DL. Dissipative fractions were also calculated for the SIC simulations and increase after five reflection cycles (figure 4.12), consistent with results from *Baker and Mashayek* (2021).

Comparison between BIC, SIC and depth-uniform currents show that energy dissipation fractions in the bottom 1000 m of the domain are largest for SIC simulations with values higher than 0.8 for all simulations. Depth uniform simulations also show enhanced dissipation near bathymetry. BIC simulations present more evenly distributed dissipative fractions. However, wave reflection is not accounted for since the analysis is done over the propagation time. Dissipative layers and areas with intense IO dictate the dissipation distribution. As a comparison, *Nikurashin and Ferrari* (2010a) found that 50% of the energy dissipation happens in the 1000m above bathymetry. However, this paper did not include depth-varying current or surface reflection.

The simulations presented in Chapter 3 were run using the hydrostatic mode of MITgcm and the non-hydrostatic mode for Chapter 4. The hydrostatic approximation is considered sufficient for Chapter 3 because the vertical scale of the wave decreases with height. However, the hydrostatic approximation starts to break down where the bathymetric scale is similar to the domain depth. Exploring the non-hydrostatic effects would be worthwhile for BIC in future work. As for the non-hydrostatic mode, we suspect that MITgcm is not precisely solving the pressure components, affecting calculations. Increasing the spatial resolution or the number of iterations allowed for the model to converge could ameliorate the model's accuracy, see *Mayer and Fringer* (2021) for an analysis of the impacts of the non-hydrostatic equations on numerical simulation results. Time constraints and computational power limited the extent of solutions explored to set up the model better. However, the non-hydrostatic

simulations present spatial patterns that fit with theoretical expectations. Therefore, we are confident that the physics is realistically represented. The time variability of the dynamics between simulations, especially for Chapter 3, presented a challenge. For Chapter 3, an analysis time of 1.5 times the propagation time was set instead of a shared analysis time for all simulations to ensure dynamic similarity between simulations. Simulated results were time average to reduce the variability associated with each time step and generalize results.

Results from Chapter 3 agree with theoretical expectations for the most part. However, Chapter 4 has revealed numerous unanswered questions. What drives the time dependency of the energy terms and the inversion of their signs? What causes the interference patterns between upwards propagating and downwards reflected waves? How can wave interference be accurately and universally described? To answer these questions, a mathematical analysis of the problem under non-hydrostatic conditions is required. Curious minds will find hints to answer these questions from atmospheric literature, where impacts of background currents have been explored for many years, for example, *Grubišić and Stiperski* (2009) or *Doyle and Durran* (2002).

For future work, it would be interesting to expand *Thorpe* (1992) and *Thorpe* (1996) work on lee wave generated on a corrugated slope and verify its predictions using a numerical model. Then, including sheared currents and assessing the impact of the slope on lee wave propagation. Furthermore, it would be interesting to test more realistic currents and bathymetry. The combination of a positively sheared current underlying a zone of negative shear could be interesting as the wave will gain energy until the shear becomes negative and might encounter a dissipative layer within the negative shear. Zones of enhanced dissipation would likely be found in these currents.

The impact of depth-varying current is significant on wave energy. It allows for exchanges with the background flow and changes the vertical distribution of kinetic energy and dissipation depending on the current type. This thesis shows that the energy propagates away from the generation site, leading to interference between waves. Energy dissipation is strongly affected by the presence of dissipative layers, inertial oscillations, vertical modes, and wave interference, all of which can arise from

sheared currents. Therefore, depth-varying currents should be taken into account when developing a parameterization. However, further research is recommended to generalize results from surface-intensified currents and the impact of wave reflection.

Appendix A

Kinetic Energy Equation Derivation

Here, we will derive the kinetic energy equation (eq. 2.21) presented in Chapter 2. We start with the 3D, non-hydrostatic, Boussinesq equation of motion, and the continuity equation. The flow is separated in a background current oriented in the x-direction $U(z)$, the residual horizontally averaged current (RHAC), $\overline{\mathbf{u}} = (\overline{u}, \overline{v}, \overline{w})$ and the wave perturbations $\mathbf{u}' = (u', v', w')$. The total flow is written as:

$$\mathbf{u}_t = (u, v, w) = (U(z) + \overline{u} + u', v + \overline{v}, w + \overline{w}). \tag{A.1}$$

The momentum equations are :

$$\begin{aligned} \frac{\partial}{\partial t}(U(z) + \overline{u} + u') + \mathbf{u}_t \cdot \nabla(U(z) + \overline{u} + u') - (\overline{v} + v')f \\ = \frac{-1}{\rho_0}\frac{\partial p}{\partial x} + \nu\nabla^2(U(z) + u' + \overline{u}) \end{aligned} \tag{A.2}$$

$$\begin{aligned} \frac{\partial}{\partial t}(v' + \overline{v}) + \mathbf{u}_t \cdot \nabla(v' + \overline{v}) + (U(z) + \overline{u} + u')f \\ = \frac{-1}{\rho_0}\frac{\partial p}{\partial y} + \nu\nabla^2(v' + \overline{v}) \end{aligned} \tag{A.3}$$

$$\frac{\partial}{\partial t}(w' + \overline{w}) + \mathbf{u}_t \cdot \nabla(w' + \overline{w}) = \frac{-1}{\rho_0}\frac{\partial p}{\partial z} - \frac{\rho g}{\rho_0} + \nu\nabla^2(w' + \overline{w}) \tag{A.4}$$

where f is the Coriolis parameter, p the pressure, and ν the molecular kinetic viscosity. The above system of equation is multiplied by the background density, ρ_0, and the dot product is taken with the wave perturbation velocity to obtain the kinetic energy equation:

$$\rho_0 u' \left[\frac{\partial}{\partial t}(U(z) + \overline{u} + u') + \mathbf{u}_t \cdot \nabla(U(z) + \overline{u} + u') - (\overline{v} + v')f \right.$$
$$\left. = \frac{-1}{\rho_0}\frac{\partial p}{\partial x} + \nu\nabla^2(U(z) + u' + \overline{u}) \right] \tag{A.5}$$
$$\rho_0 v' \left[\frac{\partial}{\partial t}(v' + \overline{v}) + \mathbf{u}_t \cdot \nabla(v' + \overline{v}) + (U(z) + \overline{u} + u')f \right.$$
$$\left. = \frac{-1}{\rho_0}\frac{\partial p}{\partial y} + \nu\nabla^2(v' + \overline{v}) \right] \tag{A.6}$$
$$\rho_0 w' \left[\frac{\partial}{\partial t}(w') + \mathbf{u}_t \cdot \nabla(w') = \frac{-1}{\rho_0}\frac{\partial p}{\partial z} - \frac{\rho g}{\rho_0} + \nu\nabla^2(w') \right] \tag{A.7}$$

To get the 2-D kinetic energy equation, the y-derivatives are neglected. The equations are further simplified by assuming that $\overline{w} \approx 0$. Each term is expanded and presented below.

A.1 Time Derivative

The time derivative term,

$$\rho_0 \mathbf{u}' \cdot \frac{\partial \mathbf{u}_t}{\partial t}, \tag{A.8}$$

is expanded, and simplified by assuming that the background current is steady in time:

$$\rho_0 \mathbf{u}' \cdot \frac{\partial \mathbf{u}_t}{\partial t} = \rho_0 \left(\cancel{u' \frac{\partial U(z)}{\partial t}} + u'\frac{\partial u'}{\partial t} + u'\frac{\partial \overline{u}}{\partial t} + v'\frac{\partial v'}{\partial t} + w'\frac{\partial \overline{v}}{\partial t} + w'\frac{\partial w'}{\partial z} \right).$$

By applying the chain rule to the time derivative of the wave perturbation, the wave velocity can be brought inside the derivative. This yields the time derivative of the wave kinetic energy (A.9a), where $K = 1/2\rho_0(u'^2 + v'^2 + w'^2)$. The RHAC terms are joined together to form the time variability of the RHAC term (A.9b):

$$\rho_0 \mathbf{u}' \cdot \frac{\partial \mathbf{u}_t}{\partial t} = \frac{\partial}{\partial t}\frac{1}{2}\rho_0(u'^2 + v'^2 + w'^2) + \rho_0 \mathbf{u}' \cdot \left(\frac{\partial \overline{u}}{\partial t} + \frac{\partial \overline{v}}{\partial t} \right)$$
$$= \underbrace{\frac{\partial}{\partial t}K}_{A.9a} + \underbrace{\rho_0 \mathbf{u}' \cdot \left(\frac{\partial \overline{\mathbf{u}}}{\partial t} \right)}_{A.9b}. \tag{A.9}$$

A.2 Advection Term

The advection term from the momentum equations is

$$\rho_0 \mathbf{u}' \cdot (\mathbf{u}_t \cdot \nabla \mathbf{u}_t). \tag{A.10}$$

First, we will expand $\rho_0 \mathbf{u}' \cdot (\mathbf{u}_t \cdot \nabla \mathbf{u}_t)$ and the equation is simplified considering that the background current is a fuction of z, $U(z) = f(z)$, and that the RHAC present no variability in the x-direction ($\partial \overline{\mathbf{u}}/\partial x = 0$)

$$\begin{aligned}
\mathbf{u}_t \cdot \nabla \mathbf{u}_t = & \\
& u'\rho_0 \left((U(z) + \overline{u} + u') \frac{\partial (\cancel{U(z)} + \cancel{\overline{u}} + u')}{\partial x} + (w') \frac{\partial (U(z) + \overline{u} + u')}{\partial z} \right) \\
& + v'\rho_0 \left((U(z) + \overline{u} + u') \frac{\partial (\cancel{\overline{v}} + v')}{\partial x} + (w') \frac{\partial (\overline{v} + v')}{\partial z} \right) \\
& + w'\rho_0 \left((U(z) + \overline{u} + u') \frac{\partial (w')}{\partial x} + (w') \frac{\partial (w')}{\partial z} \right).
\end{aligned} \tag{A.11}$$

To ease physical interpretation, equation A.11 will be separated into three groups. The first group contains terms that include the background current. The second group contains expressions that include the RHAC. Lastly, the third group contains terms comprised of the wave perturbations. The following sections present the expansion of each group.

A.2.1 Background Current Terms

All the terms from equation A.11 that include the background current are collected:

$$\begin{aligned}
& \rho_0 u' \left(U(z) \frac{\partial u'}{\partial x} + w' \frac{dU(z)}{dz} \right) \\
& + \rho_0 v' \left(U(z) \frac{\partial v'}{\partial x} \right) \\
& + \rho_0 w' \left(U(z) \frac{\partial w'}{\partial x} \right).
\end{aligned}$$

By applying the chain rule to the derivative of the wave velocity, we get the

advection of kinetic energy from the background current,

$$\rho_0 \left(u'U(z)\frac{\partial u'}{\partial x} + v'U(z)\frac{\partial v'}{\partial x} + w'U(z)\frac{\partial w'}{\partial x} \right) = U(z)\frac{\partial}{\partial x}K. \tag{A.12}$$

The remaining term is the shear production term,

$$\rho_0 u'w'\frac{dU(z)}{dz}. \tag{A.13}$$

A.2.2 Residual Horizontally-Averaged Current terms

The RHAC term is:

$$\begin{aligned}\rho_0 \Bigg[& u'(\overline{u})\frac{\partial u'}{\partial x} + u'(w')\frac{\partial(\overline{u}+u')}{\partial z} \\ & + v'(\overline{u})\frac{\partial v'}{\partial x} + v'(w')\frac{\partial(\overline{v}+v')}{\partial z} \\ & + w'(\overline{u})\frac{\partial w'}{\partial x} + w'(w')\frac{\partial(w')}{\partial z} \Bigg].\end{aligned}$$

Similar to the advection of kinetic energy from the background current (eq. A.12), the advection of the kinetic energy from the RHAC is obtained by applying the chain rule to terms including the derivative of the wave perturbation:

$$\rho_0 \left(u'\overline{u}\frac{\partial u'}{\partial x} + v'\overline{u}\frac{\partial v'}{\partial x} + w'\overline{u}\frac{\partial w'}{\partial x} \right) = \overline{u}\frac{\partial K}{\partial x}. \tag{A.14}$$

The shear production from the RHAC is comprised of the terms that include the vertical derivative of the RHAC terms,

$$\rho_0 \left(u'w'\frac{\partial \overline{u}}{\partial z} + v'w'\frac{\partial \overline{v}}{\partial z} \right) = \rho_0 w'(\mathbf{u}' \cdot \frac{\partial}{\partial z}\overline{\mathbf{u}}). \tag{A.15}$$

A.2.3 Turbulent Transport of Kinetic energy

Lastly, advections terms comprised of the wave velocity are group together to form the turbulent transport of kinetic energy by applying the chain rule,

$$\begin{aligned}\rho_0(u'u'\frac{\partial u'}{\partial x} + u'w'\frac{\partial u'}{\partial z} + v'u'\frac{\partial v'}{\partial x} + v'w'\frac{\partial v'}{\partial z} + w'u'\frac{\partial w'}{\partial x} + w'w'\frac{\partial w'}{\partial z}) = \\ \rho_0(u'\frac{1}{2}\frac{\partial u'^2}{\partial x} + w'\frac{1}{2}\frac{\partial u'^2}{\partial z} + u'\frac{1}{2}\frac{\partial v'^2}{\partial x} + w'\frac{1}{2}\frac{\partial v'^2}{\partial z} + u'\frac{1}{2}\frac{\partial w'^2}{\partial x} + w'\frac{1}{2}\frac{\partial w'^2}{\partial z}) = \\ u'\frac{\partial K}{\partial x} + w'\frac{\partial K}{\partial z} = \\ \mathbf{u}' \cdot \nabla K. \end{aligned} \quad \text{(A.16)}$$

A.3 Coriolis Terms

Terms that include the Coriolis parameter are collected from equations A.5 to A.7:

$$-\rho_0(u'(\overline{v} + v')f + v'(U(z) + \overline{u} + u')f).$$

In the numerical model, the background current is imposed as a body force equal to $U(z)f$ in the y-direction momentum equation. This body force allows for a geostrophic balance in a two-dimensional system. As for the terms including the RHAC, it is assumed they are negligeable.

A.4 Transfer of Kinetic Energy to Potential Energy

In the kinetic energy equation (eq. A.5 to A.7), the buoyancy term from the z-direction momentum equation, $(\rho' g)/\rho_0$, in eq. A.4, becomes the transfer of kinetic energy to potential energy term, also referred to as the buoyancy production,

$$w'\rho_0 \left(\frac{-\rho' g}{\rho_0}\right) = -\rho' g w'. \quad \text{(A.17)}$$

A.5 Energy Flux Divergence

The energy flux divergence arise from the pressure term in the momentum equations. The continuity equation (eq. 2.2) can be used to bring the velocity perturbation inside the derivative:

$$\begin{aligned} &- \mathbf{u}' \cdot \nabla p \\ &= - \nabla \cdot (\mathbf{u}' p). \end{aligned} \tag{A.18}$$

A.6 Dissipation term

To facilitate physical interpretation, the dissipative term from the energy equation, i.e. $\nu \mathbf{u}' \cdot \nabla^2 \mathbf{u}_t$, is expanded and simplified assuming that the second derivative of the background current and RHAC is small, i.e. $\nabla^2 U(z) \approx 0$ and $\nabla^2 \overline{\mathbf{u}} \approx 0$:

$$\rho_0 \nu \mathbf{u}' \cdot \nabla^2 \mathbf{u}' =$$
$$\rho_0 \nu \left[u' \frac{\partial}{\partial x} \frac{\partial}{\partial x} u' + u' \frac{\partial}{\partial z} \frac{\partial}{\partial z} u' + v' \frac{\partial}{\partial x} \frac{\partial}{\partial x} v' + v' \frac{\partial}{\partial z} \frac{\partial}{\partial z} v' + w' \frac{\partial}{\partial x} \frac{\partial}{\partial x} w' + w' \frac{\partial}{\partial z} \frac{\partial}{\partial z} w' \right].$$

Then the chain rule is applied to each term to form the viscous diffusion of the

kinetic energy (A.19a) and the dissipation of the kinetic energy (A.19b):

$$
\begin{aligned}
&\rho_0\nu\mathbf{u}'\cdot\nabla^2\mathbf{u}' = \\
=&\rho_0\nu\left[\frac{\partial}{\partial x}\left(u'\frac{\partial u'}{\partial x}\right)-\left(\frac{\partial u'}{\partial x}\right)^2+\frac{\partial}{\partial z}\left(u'\frac{\partial u'}{\partial z}\right)-\left(\frac{\partial u'}{\partial z}\right)^2\right. \\
&+\frac{\partial}{\partial x}\left(v'\frac{\partial v'}{\partial x}\right)-\left(\frac{\partial v'}{\partial x}\right)^2+\frac{\partial}{\partial z}\left(v'\frac{\partial v'}{\partial z}\right)-\left(\frac{\partial v'}{\partial z}\right)^2 \\
&\left.+\frac{\partial}{\partial x}\left(w'\frac{\partial w'}{\partial x}\right)-\left(\frac{\partial w'}{\partial x}\right)^2+\frac{\partial}{\partial z}\left(w'\frac{\partial w'}{\partial z}\right)-\left(\frac{\partial w'}{\partial z}\right)^2\right] \\
=&\rho_0\nu\left[\frac{\partial}{\partial x}\left(\frac{\partial}{\partial x}\frac{1}{2}u'^2\right)+\frac{\partial}{\partial z}\left(\frac{\partial}{\partial z}\frac{1}{2}u'^2\right)-\left(\frac{\partial u'}{\partial x}\right)^2-\left(\frac{\partial u'}{\partial z}\right)^2\right. \\
&+\frac{\partial}{\partial x}\left(\frac{\partial}{\partial x}\frac{1}{2}v'^2\right)+\frac{\partial}{\partial z}\left(\frac{\partial}{\partial z}\frac{1}{2}v'^2\right)-\left(\frac{\partial v'}{\partial x}\right)^2-\left(\frac{\partial v'}{\partial z}\right)^2 \\
&\left.+\frac{\partial}{\partial x}\left(\frac{\partial}{\partial x}\frac{1}{2}w'^2\right)+\frac{\partial}{\partial z}\left(\frac{\partial}{\partial z}\frac{1}{2}w'^2\right)-\left(\frac{\partial w'}{\partial x}\right)^2-\left(\frac{\partial w'}{\partial z}\right)^2\right] \\
=&\rho_0\nu\left[\frac{\partial^2}{\partial x^2}\left(\frac{1}{2}(u'^2+v'^2+w'^2)\right)+\frac{\partial^2}{\partial z^2}\left(\frac{1}{2}(u'^2+v'^2+w'^2)\right)\right. \\
&\left.-(\nabla u')^2-(\nabla v')^2-(\nabla w')^2\right] \\
=&\nu\left[\frac{\partial^2}{\partial x^2}(K)+\frac{\partial^2}{\partial z^2}(K)-\rho_0(\nabla\mathbf{u}')^2\right] \\
=&\underbrace{\nu\nabla^2(K)}_{A.19a}-\underbrace{\nu\rho_0(\nabla\mathbf{u}')^2}_{A.19b}.
\end{aligned}
\tag{A.19}
$$

Note that the energy disispation (A.19b) is a positive definite quantity multiplied by -1, thus an energy sink.

A.7 The Kinetic Energy Equation

The full 3-D kinetic equation can be rewrite using the different expression presented above as

$$\underbrace{\frac{\partial}{\partial t}K}_{1} + \underbrace{\rho_0 \mathbf{u}' \cdot \left(\frac{\partial}{\partial t}\overline{\mathbf{u}}\right)}_{2} = -\underbrace{U(z)\frac{\partial K}{\partial x}}_{3} - \underbrace{\overline{u} \cdot \nabla K}_{4} - \underbrace{\mathbf{u}'\nabla K}_{5} - \underbrace{\rho_0 u'w'\frac{dU(z)}{dz}}_{6} \tag{A.20}$$

$$-\rho_0 \underbrace{w'\left(\mathbf{u}' \cdot \frac{\partial \overline{\mathbf{u}}}{\partial z}\right)}_{7} - \underbrace{w'\rho g}_{8} - \underbrace{\nabla(\mathbf{u}'p)}_{9} + \underbrace{\nu\nabla^2(K)}_{10} - \underbrace{\nu\rho_0(\nabla\mathbf{u}')^2}_{11}, \tag{A.21}$$

where the different terms are:

1. Time derivative of K;
2. Time dependency of RHAC;
3. Advection of K from background current;
4. Advection of K from RHAC;
5. Advection of K from wave velocities;
6. Shear production from the background current;
7. Shear production from the RHAC;
8. Energy transfer from K to available potential energy (buoyancy production);
9. Pressure work;
10. Viscous diffusion of K;
11. Viscous dissipation of K.

Appendix B

Detailed Simulation Set Up and Parameters

The numerical model set up is presented below for each simulation group, the BIC, SIC and Line W simulations.

B.1 Bottom-Intensified Simulations

The simulation set up for the BIC simulations (Chapter 3) is:

1. Bathymetry: Idealized sinusoidal
2. Stratification: Constant;
3. Shear: Linear;
4. Current profile: $U(z) = -5 \times 10^{-5} z + 0.05$ (m/s);
5. Bottom current velocity: $U_b = 0.2$ m/s;
6. Topographic height: $h_0 = 50$ m;
7. Boundary condition: free-slip condition;
8. Equation type: hydrostatic equations;
9. Boundary conditions: Free surface, horizontally periodic.

The following table present in details the parameters used for each simulation.

Table B.1: Bottom intensified simulation resolution and parameters

	Horizontal resolution	Vertical resolution	Time step	CFL condition	Horizontal eddy kinetic viscosity	Vertical eddy kinetic viscosity	Horizontal eddy diffusivity	Vertical eddy diffusivity
	Δx	Δz	Δt	-	ν_h	ν_v	κ_h	κ_h
	m	m	s	-	m^2/s	m^2/s	m^2/s	m^2/s
BIC1.4km	50	10	2	0.008	5×10^{-2}	5×10^{-4}	5×10^{-2}	5×10^{-4}
BIC3km	50	10	2	0.008	5×10^{-2}	5×10^{-4}	5×10^{-2}	5×10^{-4}
BIC5km	50	10	2	0.008	5×10^{-2}	5×10^{-4}	5×10^{-2}	5×10^{-4}
BNS5km	50	10	2	0.008	5×10^{-2}	5×10^{-4}	5×10^{-2}	5×10^{-4}
BIC7km	50	10	2	0.008	5×10^{-2}	5×10^{-4}	5×10^{-2}	5×10^{-4}
BIC13km	200	10	10	0.01	5×10^{-2}	5×10^{-4}	5×10^{-2}	5×10^{-4}
BIC32km	200	10	10	0.01	5×10^{-2}	5×10^{-4}	5×10^{-2}	5×10^{-4}
BIC56km	200	10	10	0.01	5×10^{-2}	5×10^{-4}	5×10^{-2}	5×10^{-4}
BIC72km	200	10	10	0.01	5×10^{-2}	5×10^{-4}	5×10^{-2}	5×10^{-4}
BNS72km	200	10	10	0.01	5×10^{-2}	5×10^{-4}	5×10^{-2}	5×10^{-4}

B.2 Surface-Intensified Simulations

The simulation set up for the SIC simulations (Chapter 4) is:

1. Bathymetry: Idealized sinusoidal
2. Stratification: Constant;
3. Shear: Linear;
4. Current profile: $U(z) = 2.6 \times 10^{-5} z + 1$ (m/s);
5. Bottom current velocity: $U_b = 0.2$ m/s;
6. Topographic height: $h_0 = 50$ m;
7. Boundary condition: free-slip condition;
8. Equation type: non-hydrostatic equations;
9. Boundary conditions: Free surface, horizontally periodic.

Table B.2: Surface intensified simulation resolution and parameters

	Horizontal resolution	Vertical resolution	Time step	CFL condition	Horizontal eddy viscosity	Vertical eddy kinetic viscosity	Horizontal eddy diffusivity	Vertical eddy diffusivity
	Δx	Δz	Δt	-	ν_h	ν_v	κ_h	κ_h
	m	m	s	-	m^2/s	m^2/s	m^2/s	m^2/s
SIC1.4km	50	10	2	0.008	5×10^{-2}	5×10^{-4}	5×10^{-2}	5×10^{-4}
SIC3km	50	10	2	0.008	5×10^{-2}	5×10^{-4}	5×10^{-2}	5×10^{-4}
SIC5km	50	10	2	0.008	5×10^{-2}	5×10^{-4}	5×10^{-2}	5×10^{-4}
SNS5km	50	10	2	0.008	5×10^{-2}	5×10^{-4}	5×10^{-2}	5×10^{-4}
SIC7km	50	10	2	0.008	5×10^{-2}	5×10^{-4}	5×10^{-2}	5×10^{-4}
SIC13km	200	10	10	0.01	5×10^{-2}	5×10^{-4}	5×10^{-2}	5×10^{-4}
SIC32km	200	10	10	0.01	5×10^{-2}	5×10^{-4}	5×10^{-2}	5×10^{-4}
SIC56km	200	10	10	0.01	5×10^{-2}	5×10^{-4}	5×10^{-2}	5×10^{-4}
SIC72km	200	10	10	0.01	5×10^{-2}	5×10^{-4}	5×10^{-2}	5×10^{-4}
SNS72km	200	10	10	0.01	5×10^{-2}	5×10^{-4}	5×10^{-2}	5×10^{-4}

Appendix C

SIC: Shear production spectra

Below are the spectra for simulations SIC1.4km to SIC72km. The spectra are calculated at each point of the integration domain and averaged together. The number of spectra ranges from 14000 to 180000. The mean has been remove before performing the spectral analysis. The spectra are calculated over the analysis time.

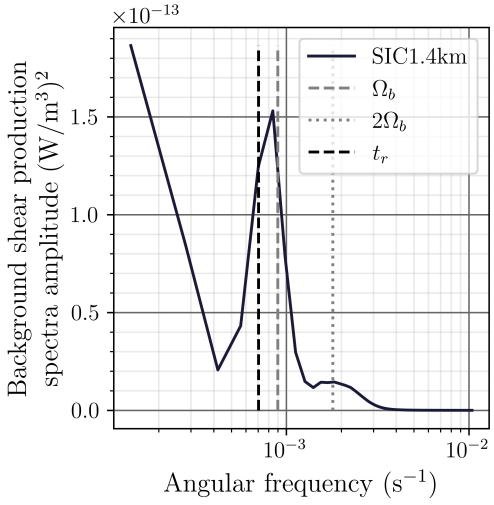
×10^−13
SIC1.4km
Ωb
2Ωb
tr
Background shear production spectra amplitude (W/m^3)^2
Angular frequency (s^−1)

(a)

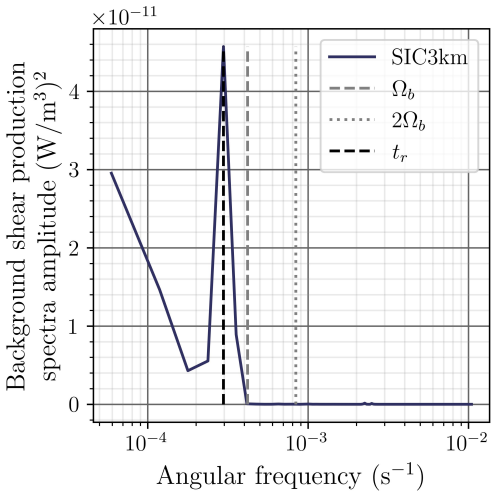
×10^−11
SIC3km
Ωb
2Ωb
tr
Background shear production spectra amplitude (W/m^3)^2
Angular frequency (s^−1)

(b)

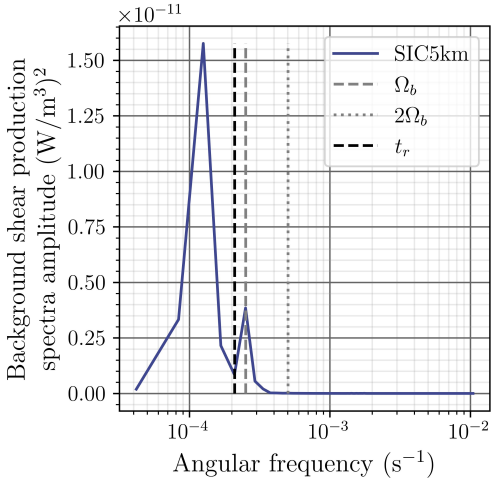
×10^−11
SIC5km
Ωb
2Ωb
tr
Background shear production spectra amplitude (W/m^3)^2
Angular frequency (s^−1)

(c)

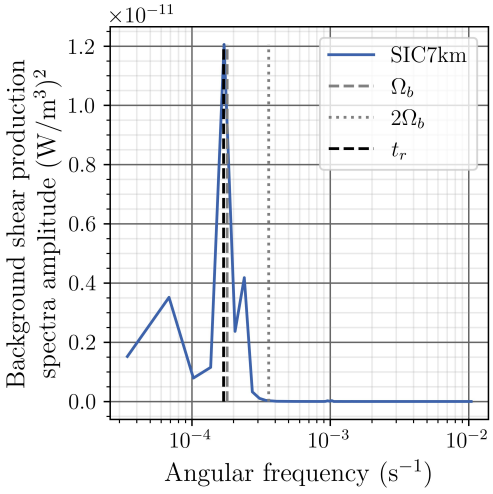
×10^−11
SIC7km
Ωb
2Ωb
tr
Background shear production spectra amplitude (W/m^3)^2
Angular frequency (s^−1)

(d)

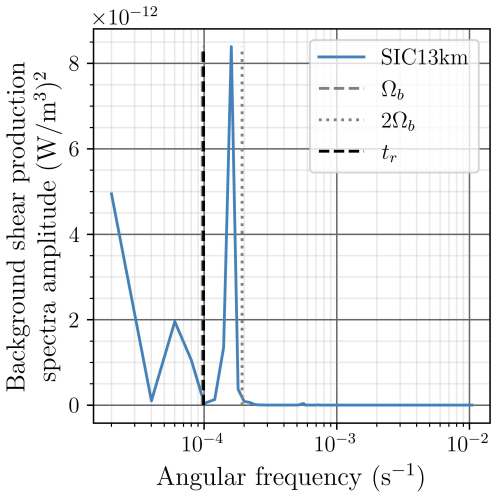
×10^−12
SIC13km
Ωb
2Ωb
tr
Background shear production spectra amplitude (W/m^3)^2
Angular frequency (s^−1)

(e)

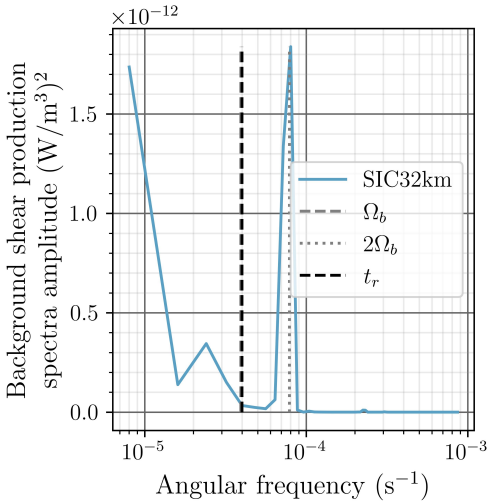
×10^−12
SIC32km
Ωb
2Ωb
tr
Background shear production spectra amplitude (W/m^3)^2
Angular frequency (s^−1)

(f)

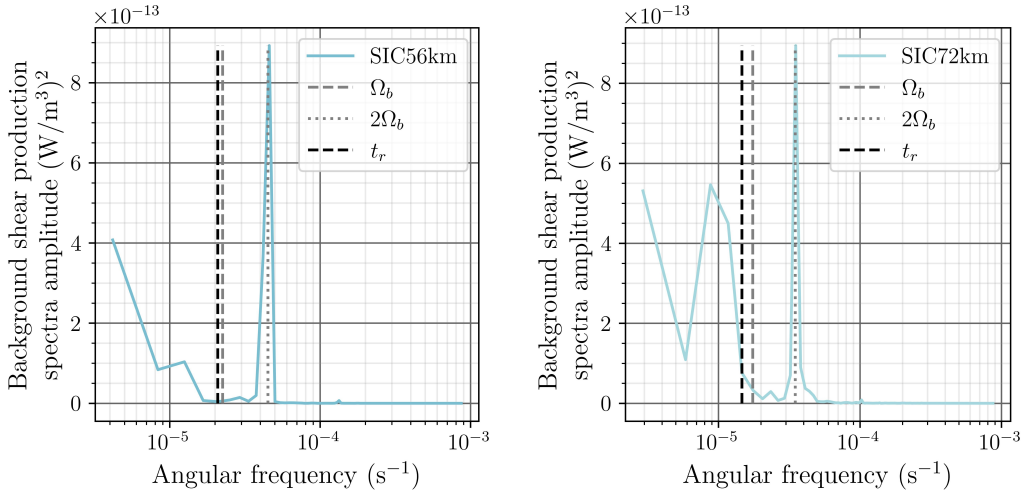

Figure C.0: Background shear production spectra. All simulations show similar patterns with three dominant frequencies. The vertical grey dashed line represent the wave generation first harmonic, $2\Omega_b$. The reflective period is marked by the dashed, black line and the wave generation frequency is marked by the dotted grey line.

Bibliography

Baker, L., and A. Mashayek, Surface reflection of bottom generated oceanic lee waves, *Journal of Fluid Mechanics*, *924*, A17, 2021, arXiv: 2103.03779.

Bell, T. H., Topographically generated internal waves in the open ocean, *Journal of Geophysical Research (1896-1977)*, *80*, 320–327, 1975.

Bretherton, F. P., C. J. R. Garrett, and M. J. Lighthill, Wavetrains in inhomogeneous moving media, *Proceedings of the Royal Society of London. Series A. Mathematical and Physical Sciences*, *302*, 529–554, 1968, publisher: Royal Society.

Colson, D., Results of Double-Theodolite Observations at Bishop, Cal., in Connection with the "Bishop-Wave" Phenomena *, *Bulletin of the American Meteorological Society*, *33*, 107–116, 1952.

Cusack, J. M., A. C. Naveira Garabato, D. A. Smeed, and J. B. Girton, Observation of a Large Lee Wave in the Drake Passage, *Journal of Physical Oceanography*, *47*, 793–810, 2017, publisher: American Meteorological Society.

de Marez, C., N. J. Lahaye, and J. Gula, Interaction of the Gulf Stream with small scale topography: a focus on lee waves, *Scientific Reports*, *10*, 2332, 2020.

Doyle, J. D., and D. R. Durran, The Dynamics of Mountain-Wave-Induced Rotors, *Journal of the Atmospheric Sciences*, *59*, 186–201, 2002, publisher: American Meteorological Society Section: Journal of the Atmospheric Sciences.

Garrett, C., What is the "Near-Inertial" Band and Why Is It Different from the Rest of the Internal Wave Spectrum?, *Journal of Physical Oceanography*, *31*, 962–971, 2001.

Garrett, C., and E. Kunze, Internal Tide Generation in the Deep Ocean, *Annual Review of Fluid Mechanics*, *39*, 57–87, 2007.

Gill, A. E., *Atmosphere-ocean dynamics*, no. 30 in International geophysics series, nachdr. ed., Acad. Press, San Diego, 2003, oCLC: 249294465.

Grimshaw, R., Wave Action and Wave-Mean Flow Interaction, with Application to Stratified Shear Flows, *Annual Review of Fluid Mechanics*, *16*, 11–44, 1984.

Grubišić, V., and I. Stiperski, Lee-Wave Resonances over Double Bell-Shaped Obstacles, *Journal of the Atmospheric Sciences*, *66*, 1205–1228, 2009.

Jones, W. L., Propagation of internal gravity waves in fluids with shear flow and rotation, *Journal of Fluid Mechanics*, *30*, 439–448, 1967, publisher: Cambridge University Press.

Klymak, J. M., Nonpropagating Form Drag and Turbulence due to Stratified Flow over Large-Scale Abyssal Hill Topography, *Journal of Physical Oceanography*, *48*, 2383–2395, 2018.

Kunze, E., and R.-C. Lien, Energy Sinks for Lee Waves in Shear Flow, *Journal of Physical Oceanography*, *49*, 2851–2865, 2019.

Legg, S., Mixing by oceanic lee waves, *Annual Review of Fluid Mechanics*, *53*, 173–201, 2021.

Long, R. R., Some Aspects of the Flow of Stratified Fluids: I. A Theoretical Investigation, *Tellus*, *5*, 42–58, 1953.

Long, R. R., Some Aspects of the Flow of Stratified Fluids: II. Experiments with a Two-Fluid System, *Tellus*, *6*, 97–115, 1954.

Long, R. R., Some Aspects of the Flow of Stratified Fluids, *Tellus*, *7*, 341–357, 1955.

Marshall, J., A. Adcroft, C. Hill, L. Perelman, and C. Heisey, A finite-volume, incompressible Navier Stokes model for studies of the ocean on parallel computers, *Journal of Geophysical Research: Oceans*, *102*, 5753–5766, 1997, _eprint: https://agupubs.onlinelibrary.wiley.com/doi/pdf/10.1029/96JC02775.

Mayer, F., and O. Fringer, Resolving nonhydrostatic effects in oceanic lee waves, *Ocean Modelling*, *159*, 101763, 2021.

Melet, A., R. Hallberg, S. Legg, and M. Nikurashin, Sensitivity of the Ocean State to Lee Wave–Driven Mixing, *Journal of Physical Oceanography*, *44*, 900–921, 2014, publisher: American Meteorological Society Section: Journal of Physical Oceanography.

Melet, A., R. Hallberg, A. Adcroft, M. Nikurashin, and S. Legg, Energy Flux into Internal Lee Waves: Sensitivity to Future Climate Changes Using Linear Theory and a Climate Model, *Journal of Climate*, *28*, 2365–2384, 2015, publisher: American Meteorological Society.

Nault, J. T., and B. R. Sutherland, Internal wave transmission in nonuniform flows, *Physics of Fluids*, *19*, 016601, 2007.

Naveira Garabato, A. C., A. J. G. Nurser, R. B. Scott, and J. A. Goff, The Impact of Small-Scale Topography on the Dynamical Balance of the Ocean, *Journal of Physical Oceanography*, *43*, 647–668, 2013.

Nikurashin, M., and R. Ferrari, Radiation and Dissipation of Internal Waves Generated by Geostrophic Motions Impinging on Small-Scale Topography: Theory, *Journal of Physical Oceanography*, *40*, 1055–1074, 2010a.

Nikurashin, M., and R. Ferrari, Radiation and Dissipation of Internal Waves Generated by Geostrophic Motions Impinging on Small-Scale Topography: Application to the Southern Ocean, *Journal of Physical Oceanography*, *40*, 2025–2042, 2010b.

Nikurashin, M., and R. Ferrari, Global energy conversion rate from geostrophic flows into internal lee waves in the deep ocean: INTERNAL LEE WAVES IN THE OCEAN, *Geophysical Research Letters*, *38*, n/a–n/a, 2011.

Nikurashin, M., R. Ferrari, N. Grisouard, and K. Polzin, The Impact of Finite-Amplitude Bottom Topography on Internal Wave Generation in the Southern Ocean, *Journal of Physical Oceanography*, *44*, 2938–2950, 2014.

Osborn, T. R., Estimates of the Local Rate of Vertical Diffusion from Dissipation Measurements, *Journal of Physical Oceanography*, *10*, 83–89, 1980.

Scorer, R. S., Theory of waves in the lee of mountains, *Quarterly Journal of the Royal Meteorological Society*, *75*, 41–56, 1949.

Scott, R. B., J. A. Goff, A. C. Naveira Garabato, and A. J. G. Nurser, Global rate and spectral characteristics of internal gravity wave generation by geostrophic flow over topography, *Journal of Geophysical Research*, *116*, C09029, 2011.

Shakespeare, C. J., Interdependence of Internal Tide and Lee Wave Generation at Abyssal Hills: Global Calculations, *Journal of Physical Oceanography*, *50*, 655–677, 2020.

Shakespeare, C. J., and A. M. Hogg, The viscous lee wave problem and its implications for ocean modelling, *Ocean Modelling*, *113*, 22–29, 2017.

Shakespeare, C. J., B. K. Arbic, and A. M. Hogg, Dissipating and Reflecting Internal Waves, *Journal of Physical Oceanography*, *51*, 2517–2531, 2021.

Sheen, K. L., J. A. Brearley, A. C. N. Garabato, D. A. Smeed, S. Waterman, J. R. Ledwell, M. P. Meredith, L. S. Laurent, A. M. Thurnherr, J. M. Toole, and A. J. Watson, Rates and mechanisms of turbulent dissipation and mixing in the Southern Ocean: Results from the Diapycnal and Isopycnal Mixing Experiment in the Southern Ocean (DIMES), *Journal of Geophysical Research: Oceans*, *118*, 2774–2792, 2013.

St. Laurent, L., A. C. Naveira Garabato, J. R. Ledwell, A. M. Thurnherr, J. M. Toole, and A. J. Watson, Turbulence and Diapycnal Mixing in Drake Passage, *Journal of Physical Oceanography*, *42*, 2143–2152, 2012.

Sun, H., Q. Yang, K. Zheng, W. Zhao, X. Huang, and J. Tian, Internal Lee Waves Generated by Shear Flow Over Small-Scale Topography, *Journal of Geophysical Research: Oceans*, *127*, 2022.

Sutherland, B. R., *Internal Gravity Waves*, Cambridge University Press, Cambridge, 2010.

Teixeira, M., J. Argaín, and P. Miranda, Drag produced by trapped lee waves and propagating mountain waves in a two-layer atmosphere: Drag Produced by Trapped Lee Waves, *Quarterly Journal of the Royal Meteorological Society*, *139*, 964–981, 2013.

Thorpe, S. A., The generation of internal waves by flow over the rough topography of a continental slope, *Proceedings of the Royal Society of London. Series A: Mathematical and Physical Sciences*, *439*, 115–130, 1992, publisher: Royal Society.

Thorpe, S. A., The Cross-Slope Transport of Momentum by Internal Waves Generated by Alongslope Currents over Topography, *Journal of Physical Oceanography*, *26*, 191–204, 1996, publisher: American Meteorological Society Section: Journal of Physical Oceanography.

Trossman, D. S., B. K. Arbic, J. G. Richman, S. T. Garner, S. R. Jayne, and A. J. Wallcraft, Impact of topographic internal lee wave drag on an eddying global ocean model, *Ocean Modelling*, *97*, 109–128, 2016.

Waterman, S., A. C. N. Garabato, and K. L. Polzin, Internal Waves and Turbulence in the Antarctic Circumpolar Current, *Journal of Physical Oceanography*, *43*, 259–282, 2013, publisher: American Meteorological Society Section: Journal of Physical Oceanography.

Waterman, S., K. L. Polzin, A. C. Naveira Garabato, K. L. Sheen, and A. Forryan, Suppression of Internal Wave Breaking in the Antarctic Circumpolar Current near Topography, *Journal of Physical Oceanography*, *44*, 1466–1492, 2014.

Winters, K. B., and L. Armi, Hydraulic control of continuously stratified flow over an obstacle, *Journal of Fluid Mechanics*, *700*, 502–513, 2012.

Wright, C. J., R. B. Scott, P. Ailliot, and D. Furnival, Lee wave generation rates in the deep ocean, *Geophysical Research Letters*, *41*, 2434–2440, 2014.

Wu, Y., E. Kunze, A. Tandon, and A. Mahadevan, Reabsorption of Lee-Wave Energy in Bottom-Intensified Currents, *Journal of Physical Oceanography*, *53*, 477–491, 2023.

Wunsch, C., The Work Done by the Wind on the Oceanic General Circulation, *Journal of Physical Oceanography*, *28*, 2332–2340, 1998, publisher: American Meteorological Society.

Wunsch, C., and R. Ferrari, 100 Years of the Ocean General Circulation, *Meteorological Monographs*, *59*, 7.1–7.32, 2018.

Yang, L., M. Nikurashin, A. M. Hogg, and B. M. Sloyan, Energy Loss from Transient Eddies due to Lee Wave Generation in the Southern Ocean, *Journal of Physical Oceanography*, *48*, 2867–2885, 2018.

Zheng, K., and M. Nikurashin, Downstream Propagation and Remote Dissipation of Internal Waves in the Southern Ocean, *Journal of Physical Oceanography*, *49*, 1873–1887, 2019, publisher: American Meteorological Society.